The Optomechanical Design, Alignment, and Performance of TolTEC: A Millimeter-wave Polarimeter

by

Emily Lunde

A Dissertation Presented in Partial Fulfillment
of the Requirements for the Degree
Doctor of Philosophy

Approved October 2023 by the
Graduate Supervisory Committee:

Philip Mauskopf, Chair
Christopher Groppi
Evan Scannapieco
Allison Noble
Sean Bryan

ARIZONA STATE UNIVERSITY

December 2023

ABSTRACT

TolTEC is a three-band millimeter-wave, imaging polarimeter installed on the 50 m diameter Large Millimeter Telescope (LMT) in Mexico. This camera simultaneously images the focal plane at three wavebands centered at 1.1 mm (270 GHz), 1.4 mm (214 GHz), and 2.0 mm (150 GHz). TolTEC combines polarization-sensitive kinetic inductance detectors (KIDs) with the LMT to produce high resolution images of the sky in both total intensity and polarization.

I present an overview of the TolTEC camera's optical system and my contributions to the optomechanical design and characterization of the instrument. As part of my work with TolTEC, I designed the mounting structures for the cold optics within the cryostat accounting for thermal contraction to ensure the silicon lenses do not fracture when cooled. I also designed the large warm optics that re-image the light from the telescope, requiring me to perform static and vibration analyses to ensure the mounts correctly supported the mirrors. I discuss the various methods used to align the optics and the cryostat in the telescope. I discuss the Zemax optical model of TolTEC and compare it with measurements of the instrument to help with characterization. Finally, I present the results of stacking galaxies on data from the Atacama Cosmology Telescope (ACT) to measure the Sunyaev-Zel'dovich (SZ) effect and estimate the thermal energy in the gas around high red-shift, quiescent galaxies as an example of science that could be done with TolTEC data. Since the camera combines high angular resolution with images at three wavelengths near distinct SZ features, TolTEC will provide precise measurements to learn more about these types of galaxies.

ACKNOWLEDGMENTS

Thank you to my committee: Phil Mauskopf, Chris Groppi, Evan Scannapieco, Allison Noble, and Sean Bryan. Phil, I have learned so much from you during my time in the lab. Thank you for pushing me to try out new instrumentation and science related things like cryogenics. I quite literally couldn't have done it without you. Sean, I appreciate you being my extra set of hands during my second trip to Mexico and for being around to answer a lot of TolTEC related questions I had during my first year.

Thank you to all my friends that I have made since starting grad school Jenna Moore, Mrudula Gopalkrishna, Mohini Jodhpurkar, Cassie Whitton, Jamie Perkins, Paul Horton, Cecilia La Place, Kyle Massingill, Justin Mathewson. Through movie nights, board games, zoom lunches, musicals, Dungeons and Dragons, and bookstore trips, we have had lots of fun. You all are a large part of how I made it through school. Huge thanks to Jenna and Justin for always helping out with the cryogenics chaos in the lab and problem solving the various headaches that come with Baby Beluga.

Thanks also to my family for supporting me though my time in grad school. Mom and Brian, thanks for giving me a place to retreat to during the summers to recharge. Also, Mom, thanks for coming to pick me up during the Covid summer when I wasn't able to fly home so I wouldn't miss a summer of lake time with all of you. Kiers and Eli, you are the best siblings I could have asked for. I appreciate the random video chats and messages that always brighten my day. Ryan, I'm thankful everyday that I found you. You have been so supportive during this whole dissertation process. Every one of you has always believed in me and I love you all.

Big thanks to all of the people who I have worked with on the TolTEC instrument team. This dissertation makes use of data products from the TolTEC imaging camera operated at the Large Millimeter Telescope Alfonso Serrano (LMT), which is a joint

project of the Mexican Consejo Nacional de Ciencia y Tecnología (CONACyT) and the University of Massachusetts, also supported by the US National Science Foundation via the University Radio Observatory programme, and the Instituto Nacional de Astrofísica, Óptica y Electrónica (INAOE). The TolTEC Project is funded under NSF MSIP Grant #1636621.

TABLE OF CONTENTS

CHAPTER Page

LIST OF TABLES

LIST OF FIGURES

Figure Page

Figure Page

Figure Page

Figure Page

Chapter 1

INTRODUCTION AND SCIENCE MOTIVATION

1.1 TolTEC

TolTEC is a three-band millimeter-wave, imaging polarimeter installed on the 50 m diameter Large Millimeter Telescope (LMT) in Mexico. This camera simultaneously images the focal plane at three wavebands centered at 1.1 mm (270 GHz), 1.4 mm (214 GHz), and 2.0 mm (150 GHz). TolTEC combines polarization-sensitive Kinetic Inductance Detectors (KIDs) with the LMT to produce 5-10 arcmin resolution maps of the sky in both total intensity and polarization. TolTEC is able to simultaneously create 6 images, one for each polarization direction for each of the three wavebands (Wilson et al. 2020).

Figures 1 and 2 show the Large Millimeter Telescope. Figure 1 shows the surface of the 50 m primary mirror and the location of the secondary mirror. The central hole in the primary is where the light enters the receiver cabin where TolTEC is installed. Figure 2 shows the LMT in its zenith position with the primary mirror pointed directly up. The doors and crane near the top of the structure were used lift the TolTEC cryostat into the receiver cabin.

The LMT has three optical surfaces. The 50 m diameter primary mirror surface is made of 180 surface segment that form 5 concentric rings. Each segment is connected to the back-structure of the LMT with multiple actuators. This creates an active surface that can correct for deformation under gravity and optical aberrations due to thermal gradients on the primary. The 2.6 m diameter secondary mirror is mounted

Figure 1. The Large Millimeter Telescope where the TolTEC camera is installed.

Figure 2. The Large Millimeter Telescope in its zenith position.

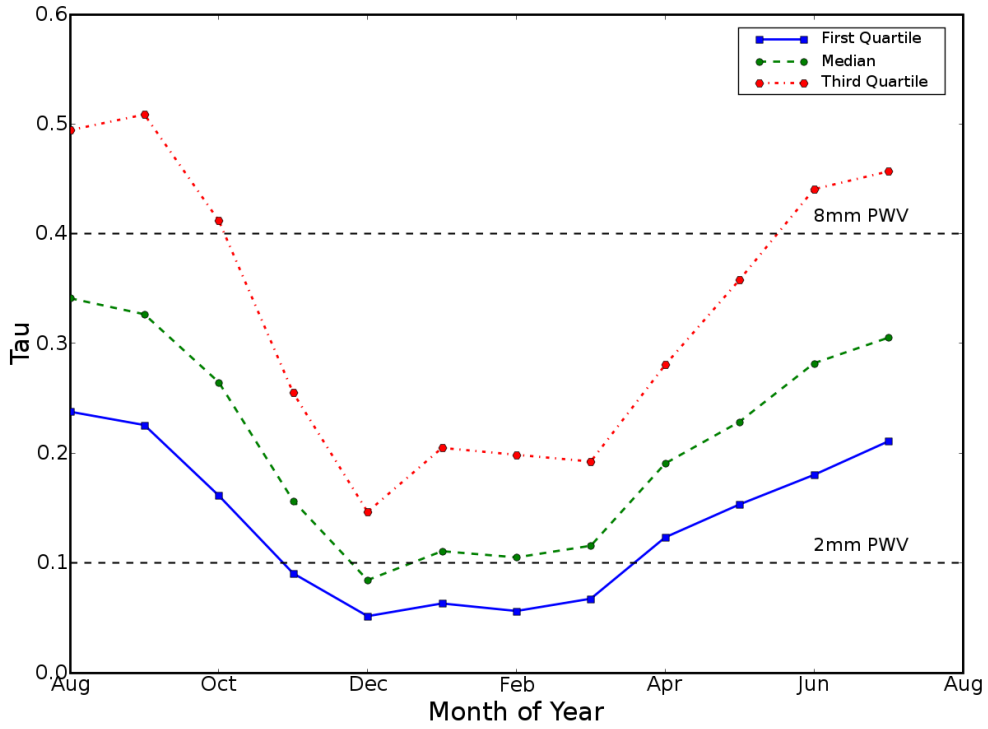

Figure 3. LMT site atmospheric opacity at 225 GHz throughout the year. Dashed horizontal lines show the opacity for two levels of precipitable water vapor in the atmosphere. Image from http://lmtserver.astro.umass.edu/site.html

on an active hexapod mount that allows adjustments of focus, lateral offsets, and tilts. The tertiary mirror is a flat elliptical shape with a 1.7 m major axis and a 1.1 m minor axis. This mirror tracks the telescope elevation axis and can be rotated to choose which instrument in the receiver cabin gets light (Hughes et al. 2010).

TolTEC is observing at millimeter wavelengths of light. These wavelengths are highly absorbed by water in the atmosphere so many millimeter-wave telescopes are built on mountains in dry regions to be above much of the Earth's atmosphere. Telescopes on mountains also have an unobstructed view of the horizon to allow more of the night sky to be observed. The Large Millimeter Telescope is located on Sierra

Negra in Puebla, Mexico at an altitude of 4580 m (15030 ft). This site has a dry season between October and May. Figure 3 shows the atmospheric opacity for 1.3 mm light over a whole year. During the dry season the opacity is < 0.06 for 25% of time, $<$ 0.1 for 50% of the time, and < 0.28 for 80% of the time (Zeballos et al. 2016; Ferrusca and Contreras R. 2014).

1.2 Millimeter-wave Instrumentation

Millimeter-wave instrumentation refers to instruments designed to detect light with wavelengths between 1-10 mm (30-300 GHz). Submillimeter-wave instrumentation looks at light with wavelengths between 0.1-1 mm (0.3-3 THz). The development of multiplexed arrays of superconducting millimeter-wave and submillimeter-wave detectors has led to a great increase in our ability to obtain astronomical images at these wavelengths. Current millimeter-wave and sub-millimeter-wave receivers such as the SPT-3G instrument on the 10 meter diameter South Pole Telescope (Sobrin et al. 2018), the Advanced-ACT receiver on the 6 meter diameter Atacama Cosmology Telescope (Koopman 2018), the NIKA2 instrument on the IRAM 30 meter Telescope (Adam, R. et al. 2018) and the SCUBA2 instrument on the 15 meter diameter James Clerk Maxwell Telescope (JCMT) (Holland et al. 2013) all have focal planes with multiple wavelength bands and thousands of pixels. Table 1 compares the parameters of these instruments. One of the challenges in telescope and instrument design is obtaining high quality imaging over the large throughput that corresponds to these array sizes while minimizing sources of stray light and heat at the detectors. TolTEC reduces the amount of stray light and heating through the use of cooled Lyot stop and baffles. Another challenge with large detector arrays is reading out the data while

Table 1. Instrument Parameters for TolTEC and Other Millimeter-wave and Submillimeter-wave Instruments

Project	TolTEC[a]	NIKA2[b]	AdvACT[c]	SPT-3G[d]	SCUBA2[e]	MUSCAT[f]
Wavelength (mm)	1.1, 1.4, 2.0	1.2, 2.0	1.3, 2.0, 3.3, 7.3, 10.7	1.4, 2.0, 3.2	0.45, 0.86	1.1
Frequencies (GHz)	270, 214, 150	260, 150	230, 150, 90 41, 28	220, 150, 95	660, 350	270
# Bands	3	2	5	3	2	1
Resolution	5” (at 270 GHz)	11” (at 260 GHz)	0.9’ (at 230 GHz)	1’ (at 150 GHz)	7.9” (at 660 GHz)	5” (at 270 GHz)
Field of View	4’	6.5’	1.1°	1.9°	3.2’	4’
Polarization	Yes	Yes	Yes	Yes	No	No
Detectors	$\sim$ 7700	$\sim$ 3000	$\sim$ 6000	$\sim$ 15000	$\sim$ 10000	$\sim$ 1600
Telescope	LMT: 50 m	IRAM: 30 m	ACT: 6 m	SPT: 10 m	JCMT: 15 m	LMT: 50 m

a: Bryan et al. 2018

b: Adam, R. et al. 2018

c: Henderson et al. 2016

d: Sobrin et al. 2018 and Benson et al. 2014

e: Dempsey et al. 2013

f: Castillo-Dominguez et al. 2018 and Brien et al. 2018

minimizing cryogenic cabling, space, and complexity. TolTEC uses microwave kinetic inductance detectors to reduce readout electronic space.

1.3 Microwave Kinetic Inductance Detectors

TolTEC utilizes three large arrays of polarization sensitive microwave kinetic inductance detectors (MKIDs) designed by NIST-Boulder to image the sky in three wavelengths(Austermann et al. 2018). TolTEC's 7700 detectors are split between three 150 mm diameter detector arrays: 4000 detectors in the 1.1 mm array, 2500 detectors in the 1.4 mm array, and 1200 detectors in the 2.0 mm array. MKIDs are superconducting resonators described by Day et al. 2003. Their resonant frequency changes in response to the absorption of incident light. This change is proportional to the amount of optical power absorbed by the detector. Data from the MKIDs can be read out using frequency domain multiplexing. Since each detector has a unique resonant frequency, large numbers of detectors can be coupled to the same feedline and read at the same time reducing the size and complexity needed for readout electronics. Table 2 references a few current and future instruments that make use of MKIDs. These detectors can be used for many different types of instrumentation including broadband imagers, polarimeters, and spectrometers.

1.4 TolTEC Science Goals

With the capability of simultaneously imaging at three wavelength and two polarization directions, TolTEC could be used in a wide variety of studies. Once

Table 2. Instruments Using MKIDs

Project	Telescope	Frequency	Type	# of Detectors
TolTEC[a]	LMT: 50 m	150,214,270 GHz	Imaging Polarimeter	7700
MUSCAT[b]	LMT: 50 m	270 GHz	Imaging Camera	1600
SuperSpec[c]	LMT: 50 m	255-278 GHz	Spectrometer	300
NIKA2[d]	IRAM: 30 m	150,260 GHz	Imaging Camera	3000
Blast-TNG[e]	Balloon: 2.5 m	600,857,1200 GHz	Polarimeter	3000
TIM[f]	Balloon: 2 m	714-1200 GHz	Intensity Mapping/Spectrometer	7200
Exclaim[g]	Balloon: 90 cm	420-550 GHz	Intensity Mapping/Spectrometer	2100
CONCERTO[h]	APEX: 12 m	130-310 GHz	Spectrometer	4300

a: Austermann et al. 2018

b: Brien et al. 2018

c: Karkare et al. 2020

d: Adam, R. et al. 2018

e: Coppi et al. 2020

f: Vieira et al. 2020

g: Essinger-Hileman et al. 2020

h: Fasano et al. 2022

commissioning is complete, TolTEC will begin collecting data for its four public legacy surveys listed here[1]:

- The Clouds-to-Cores Legacy Survey will look at giant molecular clouds to learn about their collapse into star-forming cores.
- The Field in Filaments Legacy Survey will use dust polarization to measure the distribution of magnetic fields
- The Ultra-Deep Survey of Star-forming Galaxies will look at luminous infrared galaxies at redshifts 2-10 and compare them to their optical counterparts.
- The Large Scale Structure Survey will use the Sunyaev-Zel'dovich effect to image the substructures of galaxy clusters and explore the relationship between star forming galaxy distribution and large scale structure.

1.5 Sunyaev-Zel'dovich Effect

The thermal Sunyaev-Zel'dovich (tSZ) effect occurs when CMB photons pass through hot, ionized gas (Sunyaev and Zel'dovich 1970, 1972). Since these photons have less energy than the electrons in the gas, inverse Compton scattering occurs and the photons gain energy from the electrons. Photons below a null frequency, $\nu_{null} = 217.6$ GHz, are excited to frequencies above 217.6 GHz. This shows up as a of deficit photons below and an excess of photons above the null frequency. Figure 4 shows the spectral deformation in the CMB caused by the SZ effect. The change in CMB temperature ΔT due to the tSZ effect is given by

$$\frac{\Delta T}{T_{\rm CMB}} = y\left(x\frac{e^x+1}{e^x-1} - 4\right), \tag{1.1}$$

[1]http://toltec.astro.umass.edu/science_legacy_surveys.php

where y is the Compton-y parameter and is defined as

$$y \equiv \int \sigma_T \frac{n_e k \left(T_e - T_{CMB}\right)}{m_e c^2} dl, \tag{1.2}$$

where σ_T is the Thomson cross section, k is the Boltzmann constant, m_e is the electron mass, c is the speed of light, n_e is the electron number density, T_e is the electron temperature, $T_{\rm CMB}$ is the CMB temperature ($T_{\rm CMB} = 2.725$ K), the integral is performed over the line-of-sight distance l, and the dimensionless frequency x is given by

$$x \equiv \frac{h\nu}{kT_{\rm CMB}} = \frac{\nu}{56.81\,{\rm GHz}} \tag{1.3}$$

where h is the Planck constant. The TolTEC camera will be especially suited for SZ measurements. TolTEC's three frequency bands are highlighted in figure 4. The 1.4 mm band is located at the null frequency while the 2.0 mm band should see a decrease in flux and the 1.1 mm band should see an increase in flux.

1.6 Dissertation Outline

This dissertation is organized as follows:

- Chapter 2 describes the optomechanical design of the TolTEC camera. This includes an overview of the design requirements for the optics, the design of the cold optics mounts, and design of the warm optics mounts.
- Chapter 3 describes the different techniques used to align the warm optics with the TolTEC cryostat and the LMT mirrors. And describes the methods used to characterize the TolTEC optics.
- Chapter 4 describes steps taken to upgrade one of the lab cryostats and the method used to test prototype TolTEC kinetic inductance detectors.

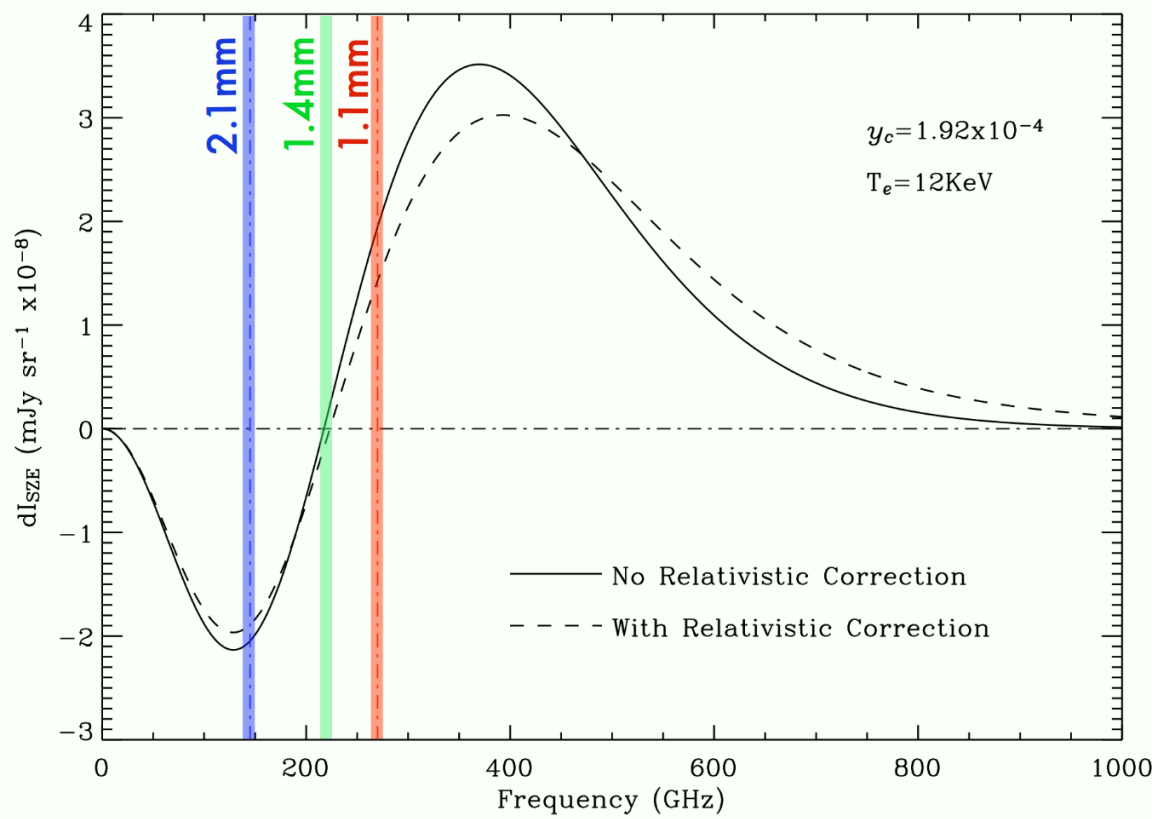

Figure 4. Spectral deformation in the flux density of the CMB caused by the Sunyaev-Zel'dovich effect. TolTEC bands are marked in colors. Image from http://toltec.astro.umass.edu/science_clusters.php

- Chapter 5 describes the method of measuring the Sunyaev-Zel-dovich effect using data from the Atacama Cosmology Telescope. And discusses what these measurements say about galactic feedback occurring in high redshift galaxies.
- Chapter 6 describes future steps to continue to optimize the TolTEC optical system.

Chapter 2

OPTOMECHANICAL DESIGN OF TOLTEC

2.1 Optics Overview

The TolTEC optics are split into two parts. The cold optics are the components within the cryostat that are cooled to 4 Kelvin or lower temperatures. The warm optics are the room temperature components that direct the light from the tertiary mirror of the LMT into the cryostat located within the receiver cabin near the Nasmyth focus. Starting from the sky, the 50 m primary mirror (M1) gathers light from an object in the sky. The secondary mirror (M2) reflects the light into the receiver cabin through a hole in M1. The tertiary mirror (M3) directs the light to the first of TolTEC's mirrors. Two curved mirrors (M4 and M6) and one flat mirror (M5) send the light into the cryostat. Figure 5 shows a computer-aided design (CAD) model of the warm optics components that come after M3. Figure 6 shows the model of the cold optics components within the cryostat. Light passes through the window of the cryostat and the Lyot stop at the 4 Kelvin stage. The first cold mirror (M7) reflects the light to the first dichroic filter (DF1). DF1 is a high-pass filter that allows TolTEC's highest frequency band (270 GHz) to pass through two lenses (L1 and L2). These lenses focus the light to the 1.1 mm detector array. DF1 reflects all other light to the third lens (L3). The light is split again by the second high-pass filter (DF2). The second band of light (150 GHz) is reflected to another cold lens (L4) which focuses the light to the 2.0 mm detector array. The final band of light (214 GHz) passes through DF2 to the

second cold mirror (M8). M8 then reflects the light through lens (L5) which focuses the light to the 1.4 mm detector array (Lunde et al. 2020).

2.2 Optics Design Requirements

The optical design of the TolTEC camera came from a process of optimizing the mirror and lens parameters to meet all of the optical requirements while also fitting into the receiver cabin and not obstructing the space of other instruments at the LMT. Additionally, the TolTEC cryostat needed to be located where it can be opened and easily accessed for maintenance purposes. The following constraints were placed on the optics design (Lunde et al. 2020):

- Window diameter is less than 30 cm due to the limit on anti-reflection coating capability for ultra-high molecular weight polyethylene (UHMWPE).
- Lyot stop diameter is 26 cm, largest possible size given the window requirement, and located at the image of the primary mirror.
- Primary mirror illumination overlap is greater than 90% across each array.
- Dichroic filter clear aperture is less than 25 cm and angles < 25 degrees.
- Silicon lens clear aperture diameters are less than 30 cm and thickness less than 2 cm.
- Strehl ratio from aberrations is greater than 0.9 over the full field at all wavelengths.
- Minimize beam ellipticity and cross polarization.
- Minimize diffraction.
- Focal ratio at the detectors is f/# $= 2.4$ so that a 4 arcmin field of view covers 130 cm diameter.

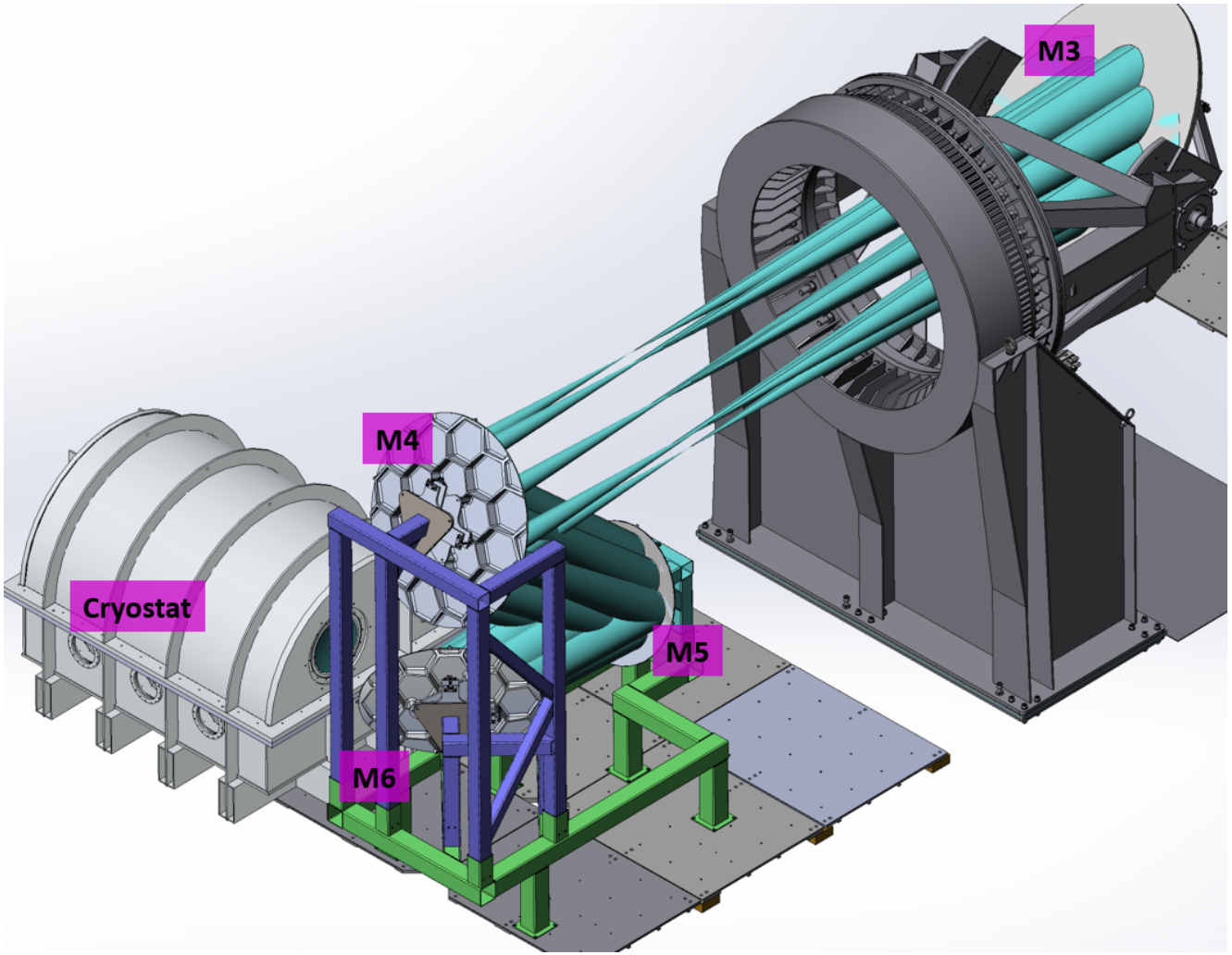

Figure 5. This CAD model shows the warm optics components of TolTEC starting with the tertiary mirror of the the LMT. Teal cones represent the optics path that light follows into the cryostat.

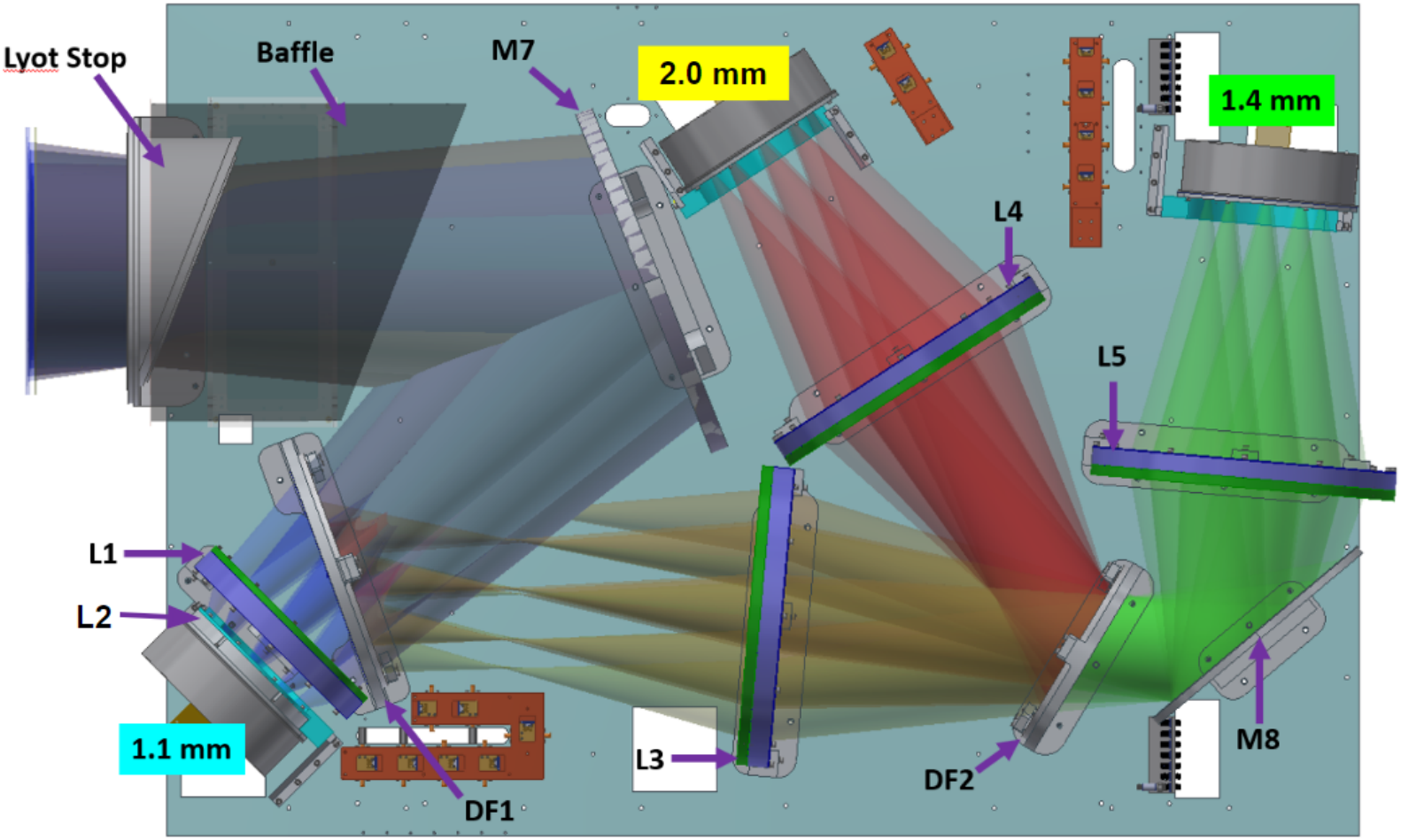

Figure 6. This CAD model shows the cold optics components of TolTEC inside the cryostat. Blue, green, and red cones represent the optics paths for the 1.1 mm, 1.4 mm, and 2.0 mm beams respectively. (Lunde et al. 2020)

Since each optical component adds noise, it was important to minimize the number of mirrors used in the reimaging optics. The optimal case for noise was placing the cryostat on the platform near the Cassegrain focus of the LMT. However, the cryostat was too large to fit on the platform, therefore, the light needed to be directed into the receiver cabin. The light needed to be directed perpendicularly to the original beam so the TolTEC cryostat would not overlap with other instruments in the LMT cabin. Adding one mirror to bend the light by 90 degrees, placed the cryostat at a height where it could not open because of the ceiling. The first reimaging mirror (M4) must be angled to reduce the height of the beam. Adding a second mirror at the desired beam height to bend the light placed TolTEC too close to another instrument in the receiver cabin, therefore, the second mirror (M5) was angled to send the beam parallel to its original path. A third mirror (M6) was used to direct the beam into the cabin at an angle of 90 degrees. The distance between the Cassegrain focus and M4 was maximized but limited by the length of the platform. This distance controlled the size of the primary mirror image. By maximizing the size of the image, the cryostat was less sensitive to its positioning. The window of the cryostat was placed near the image of the primary. All of the mirrors were designed to be simple conic sections with parameters given in Table 3.

Inside the cryostat, the Lyot stop was placed at the image of the primary mirror. By maximizing the stop diameter, the diffraction was minimized and the image quality and primary mirror overlap was maximized. The Lyot stop diameter was limited by the sizes of the window and primary mirror image.One curved mirror was added to focus the beam. The dichroic filters separated the beam into three wavelength bands (1.1 mm, 1.4 mm, and 2.0 mm). The lenses were added for beam corrections and to ensure the beams focused inside the cryostat footprint. The Silicon lenses in the cold

Table 3. Parameters for Curved, Reimaging Mirrors.

Mirror	Radius (m)	Conic	DX (m)	DY (m)	DiaX (m)	DiaY (m)
M4	5.950	-1.0	0.0	2.166	0.9	0.9
M6	2.678	-0.607	0.0	3.500	0.46	0.26
M7	1.393	-1.0	0.0	0.570	0.33	0.33

Source: Parameters from Lunde et al. 2020.

Note: The radius is the radius of curvature at the vertex of the conic section. DX and DY are decenters from the vertex to the chief ray and DiaX and DiaY are the mirror diameters in the X and Y directions, perpendicular to the propagation direction, Z.

Table 4. Parameters for Cryogenic Silicon Lenses

Lens	Radius (m)	Conic	Diameter (cm)	Thickness (cm)	Frequency (GHz)
L1	0.5468	-1.0	20.36	2.0	240-300
L2	-0.5023	-1.0	14.45	1.0	240-300
L3	0.9125	-1.0	29.66	2.0	130-240
L4	0.6766	-2.556	29.34	2.0	130-175
L5	0.6766	-2.556	29.34	2.0	185-240

Source: Parameters from Lunde et al. 2020.

Note: The radius is the radius of curvature at the vertex of the conic section. The thickness is at the center of the lens not including the anti-reflection coating. The Frequency range is the range covered by the anti-reflection coating design.

optics are flat on one side and simple conics on the other side with parameters given in Table 4. The flat mirror was added to bend the 2.0 mm band before it hit the back wall of the cryostat.

Every optical system has tolerances on the alignment of the components to achieve the desired illumination of the detectors. The angular tolerance of the TolTEC optics is more constrained than the translational tolerance. Figure 7 depicts the two types of offsets that can occur in the optics and shows how each offset affects the location of the beam on the secondary mirror through ray tracing. The red line shows an on axis beam that hits the center of all three mirrors. The blue line shows a beam that

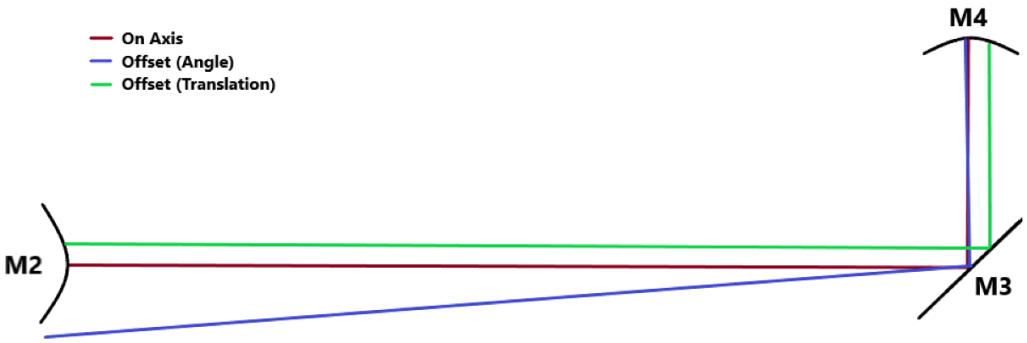

Figure 7. Optical alignment tolerance ray tracing diagram

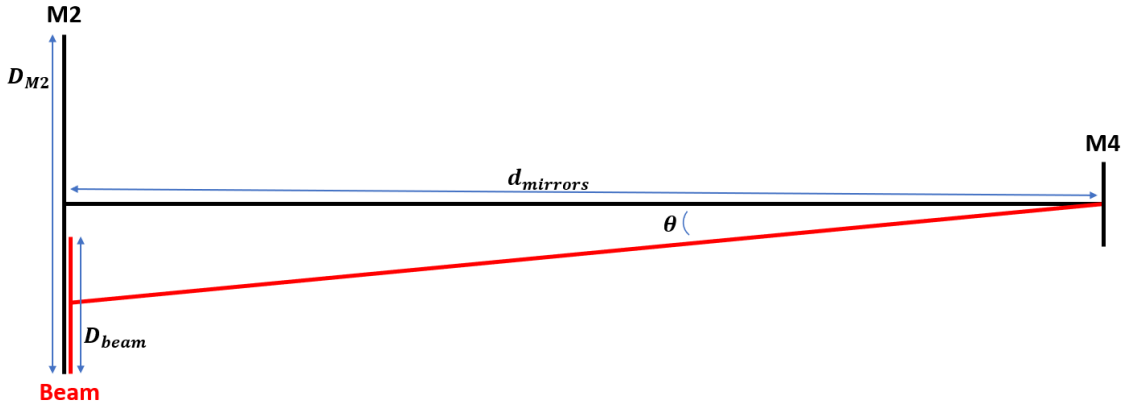

Figure 8. Diagram showing the distances and angles used to calculate the angular tolerance of the TolTEC optics.

has a small angular offset. A small angle can cause the beam to miss the secondary mirror as the light travels over the long distance between M2 and M4. The green line shows a beam that has a translational offset. This beam shows that with small offsets perpendicular to the optical axis, the beam will still hit the secondary mirror.

The angular tolerance of TolTEC can be determined by calculating the maximum beam angle that makes the beam clip the edge of the secondary mirror. For this analysis I ignore M3 since it is a flat mirror that is already aligned with M2 therefore it would not change the angular offset between the secondary mirror and TolTEC. I chose

to do this analysis between M2 and M4, since this is the largest distance that the light travels between optical components and angular offsets are especially important for long distances. Figure 8 shows the important distances used to calculate the angular tolerance of the TolTEC optics. The diameter of M2 (D_{M2}) is 2.6 m. The diameter of the beam (D_{beam}) at the surface of M2 is approximately 2.4 m. The distance between M2 and M4 ($d_{mirrors}$) is approximately 27.1 m. Using these distances, the angle can be calculated using the following equation:

$$\theta = tan^{-1}\left(\frac{(D_{M2} - D_{beam})/2}{d_{mirrors}}\right) \tag{2.1}$$

This gives an angle offset of 0.2 degrees for a beam that just starts to clip the edge of the secondary mirror. Realistically, the beam should not be at the very edge of a mirror since this adds distortion into the optics. To keep the beam off the edge of the mirror and provide a margin for errors, the angular tolerance for the TolTEC beam between M3 and M4 was set as 0.1 degrees.

2.3 Solidworks Finite Element Analysis

TolTEC's optomechanical design relies heavily on the use of the Solidworks simulation tools. Solidworks uses finite element analysis (FEA), a numerical technique that uses partial differential equations to solve structural and vibration problems. There are three steps to each analysis: defining the mathematical model, building the finite element model (meshing), and solving the model (Kurowski 2022a, 2022b).

The mathematical model starts with a simplified CAD model to create a smaller mesh and shorten the analysis times. Simplifications are made by removing bolt holes and external fillets on objects. Further simplifications are made by removing components from an assembly that have complex shapes and replacing them with a

well defined remote mass. External loads such as gravity and remote mass can be added to the model. The model restraints show the locations where reaction forces occur. The most commonly used restraint defines a surface as fixed geometry where the object is firmly fixed to the ground. After setting the model's material properties, the type of analysis (for example static or vibration) is selected.

Meshing splits the mathematical model into a finite number of tetrahedral solid elements (Kurowski 2022a). Figure 9 shows an example of a completed mesh for one of the TolTEC mirror mounts. The loads and restraints are discretized and applied to the nodes of the mesh. With the mathematical model and mesh defined, the Solidworks solver runs for the selected type of analysis. A static analysis calculates the displacements, strains, and stresses within the model. A vibration analysis calculates the resonant frequency modes of the structure. These results are compared to the established design requirements.

2.4 Cold Optics Components

As stated previously the cold optics system includes all of the mirrors, lenses, and filters that are cooled within the cryostat to 4 K. To create designs, each component from the Zemax model must be scaled to room temperature dimensions using their respective linear thermal expansion coefficient (LTE). This scaling is important since all the components will be machined and assembled at room temperature before being cooled to their 4 K operating temperature. Flanges were added to the lenses so they can be mounted without blocking the beam. The mounts dimensions were constrained by the size of the 4 K cryostat shell and the optical path.

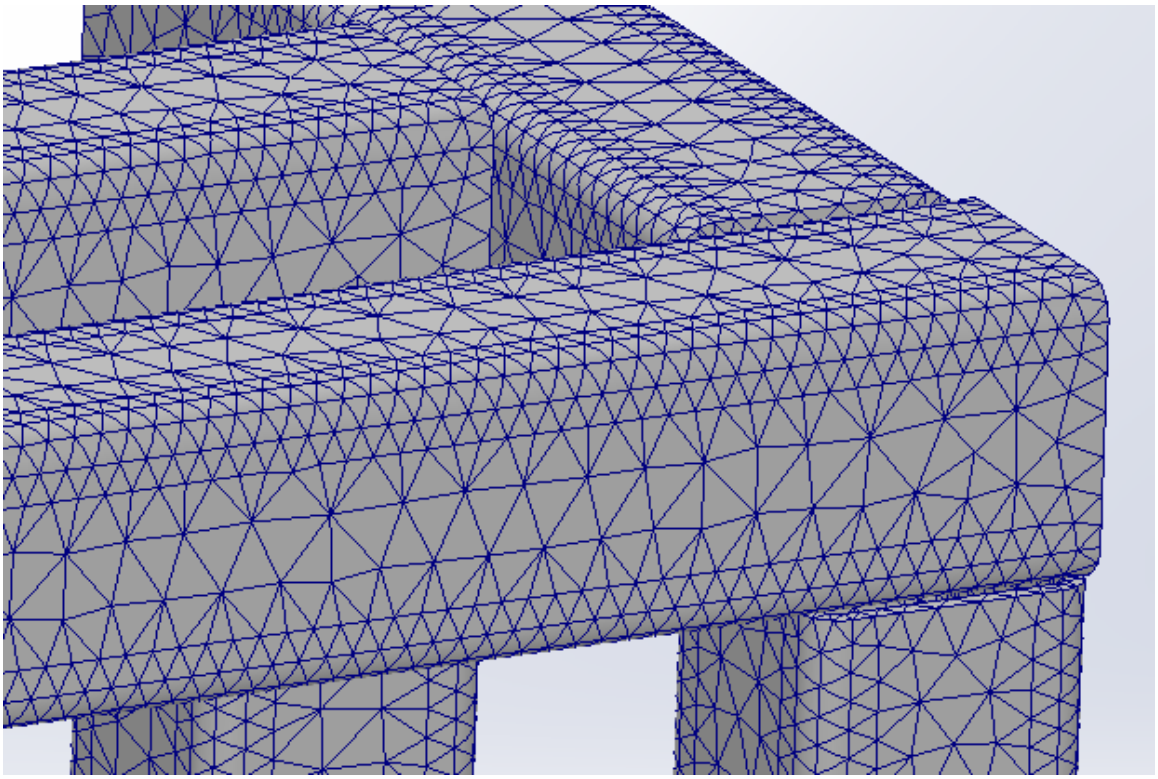

Figure 9. Example of the Solidworks mesh for the FEA simulations

2.4.1 Thermal contraction

The thermal contraction of the lenses and mounts is different as the optics components are cooled to 4 K. The LTE coefficient of the aluminum mounts is -0.004127 (Institute for Basic Standards 1977). While the LTE coefficient of the silicon lenses is -0.0002155 (Lyon et al. 1977). These values were chosen for a temperature change from 300 K to 4 K. For the lenses to be machined, the conic constants must be defined for the shape of the lens at room temperature. However, those constants were originally defined at 4 K. Equation 2.2 shows how length changes with the LTE coefficient, α (Shackelford 2015).

$$L_{300} = \frac{1}{(1+\alpha)} L = \beta L \tag{2.2}$$

Equation 2.3 shows the conic equation where R is the radius of curvature, k is the conic constant, and $c = \frac{1}{R}$.

$$z_{300} = \beta z = \beta \frac{cr^2}{1 + \sqrt{1 - (1+k)c^2 r^2}} \tag{2.3}$$

Given how lengths change with the LTE coefficient, substitute equation 2.4 in equation 2.3 for the radius. This will result in equation 2.5.

$$r = \frac{r_{300}}{\beta} \tag{2.4}$$

$$z_{300} = \frac{cr_{300}^2/\beta}{1 + \sqrt{1 - (1+k)c^2 r_{300}^2/\beta^2}} \tag{2.5}$$

Equation 2.5 implies that the radius of curvature changes with the thermal contraction while the conic constant remains the same. The new radius of curvature can be found using equation 2.6.

$$R_{300} = \beta R = \frac{1}{(1+\alpha)} R \tag{2.6}$$

With a much smaller LTE coefficient, silicon shrinks significantly less than aluminum. This introduces a risk of the lens fracturing as the mount shrinks. The mount designed to hold the lenses is shown in Figure 10. Metal Spira SS-11 gaskets were used to hold the lens radially and along the optical axis. These gaskets act like springs, to absorb the thermal contraction changes while holding the lenses in place. Along the optical axis, a complete ring of the gasket rests in a grove between the lens and the mount. As the mount is cooled, the aluminum shrinks and compresses the spring into the groove. In the radial direction, a section of this gasket presses the lens into two tabs at the bottom of the mount. This combination centers the lens in the aperture as the mount contracts without fracturing the lens.

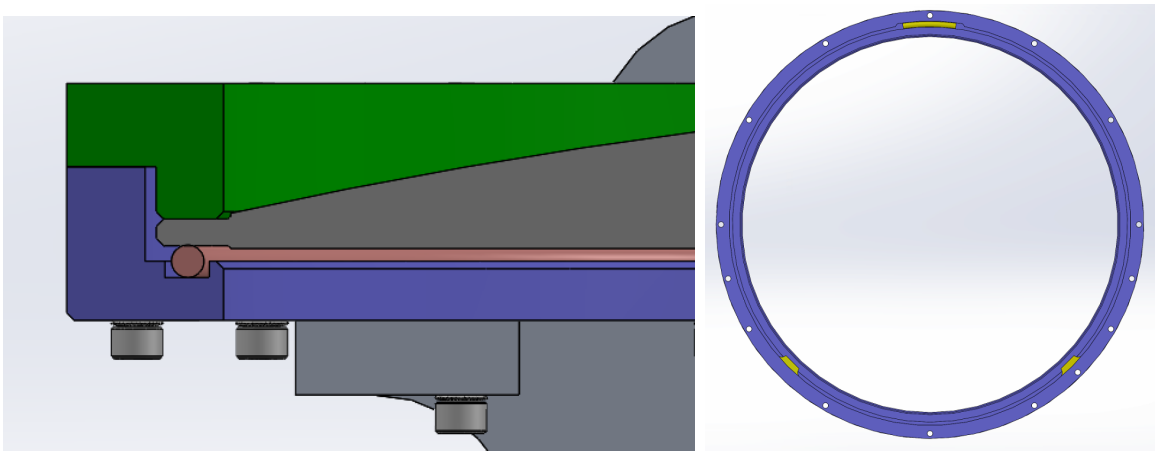

Figure 10. CAD model of a lens mount: The left image is a sectional view of lens mount. The pink colored ring is the Spira spring that absorbs the thermal contraction occurring along the optical axis. The right image is the back part of a cold lens mount. The yellow portions mark the spring segment and tabs that absorb the radial thermal contraction. Note: the size of the tabs have been exaggerated so they can be seen easily in this image. (Lunde et al. 2020)

2.4.2 Anti-reflection coating

TolTEC's large detector arrays require the use of the large aperture, cryogenic lenses with a high index of refraction that function at multiple frequencies. To reduce signal loss and increase the optical performance of the lenses, multichroic, anti-reflection (AR) coatings were needed. The metamaterial AR coatings used are cut into the surface of the lens so they have an LTE coefficient that is inherently matched to the silicon lenses. Each lens has a different metamaterial anti-reflection (AR) coating machined into its surface (Datta et al. 2013; Coughlin et al. 2018).

The Zemax lens models did not include the thickness of the AR coating. The thicknesses shown in Table 5 were added to each lens by adding a surface translation feature in the CAD model. The AR coatings are cut into the surface of the lenses using a 78 mm diameter blade. To successfully machine the coatings, the lenses are

Table 5. Anti-reflection Coatings Used on Each of the Cold Lenses.

Band (GHz)	Thickness (μm)	Number of Layers	Lens
150	320	1	L4
220	220	1	L5
270	180	1	L1/L2
150/220	642	3	L3

held underneath the dicing saw by the mounting flanges and must have a minimum clearance of 100 microns between the blade and the flange. Without this clearance the blade will cut into the mount. This clearance was used to determine the thickness of the mounting flange. Both sides of the lenses will have the AR coating. Figure 11 shows a CAD model simulating the cuts. The 78 mm diameter blade is represented by the two circles tangent to the surface of the lens. These are the original lens surfaces without the AR coating thickness added. The distance between the blade and the flat surface of the flange is measured at the point of the blades closest approach. All of the lenses achieve the 100 micron clearance (Lunde et al. 2020).

2.4.3 Lyot stop and baffling

The Lyot stop is the first optics component on the optics bench located at the entrance of the 4 K shell, placing it at the image of primary mirror. This aperture controls the amount of light that enters the cryostat and reaches the detectors. The Lyot stop contains a 4 filter cartridge and an aluminum mount that is cooled to 1.2 K and offset from the 4 K optics bench with carbon fiber standoffs. Its four filters include 2 infrared (IR) blocking filters held at an angle of 20 degrees and a pair of low-pass filters with cutoffs at 16 cm^{-1} and 12 cm^{-1} (Wilson et al. 2020). The diameter of the Lyot stop is slightly smaller than the diameter of the beam at the window of the

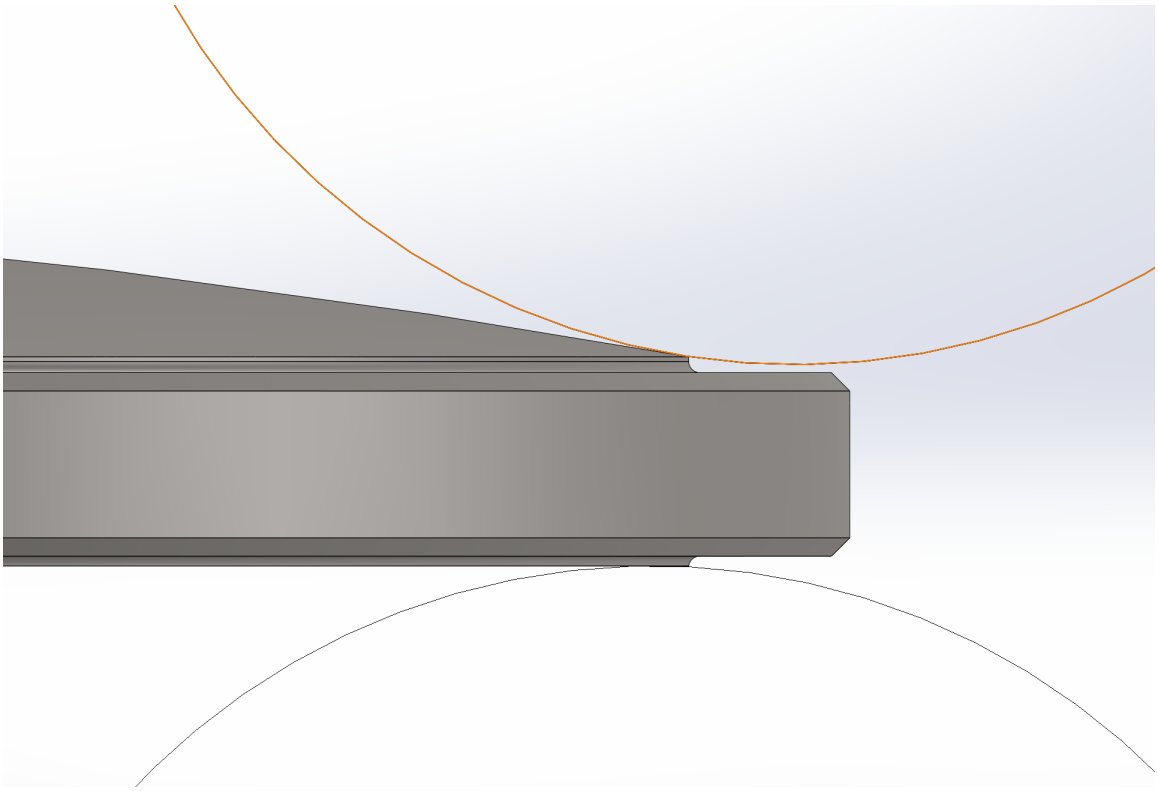

Figure 11. CAD model to show the clearance between the flange of the lens and the blade used to cut the AR coatings.The blades are shown in the positions where they are closest to the flange (Lunde et al. 2020).

cryostat. Figure 12 shows the footprint diagram of the designed Lyot stop with the aperture diameters shown. The beams in the footprint lie on the aperture edge as the Lyot stop was designed. The large Lyot aperture stop reduces diffraction and allows TolTEC to use more of the primary mirror and get better resolution on the sky.

During the initial lab testing of the optics, excess radiation noise was picked up by the detectors. A 28.5 cm baffle was designed to surround the Lyot stop and absorb additional radiation. The baffle was made from a rolled sheet of copper and blackened using carbon-infused cloth. It is also cooled to 1.2 K and offset from the 4 K optics bench with carbon fiber standoffs. The baffle provides a large surface area

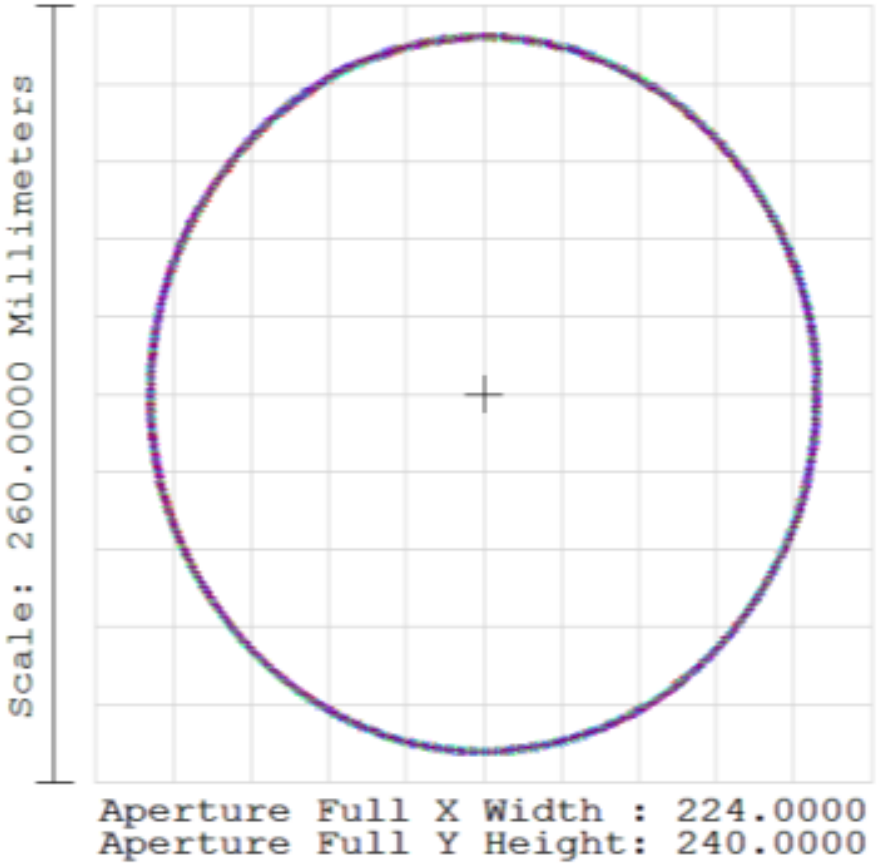

Figure 12. Footprint diagram of the Lyot stop.

on which stray, scattered light is absorbed long before it reaches the detectors (Lunde et al. 2020).

2.4.4 Cold optics bench

The cold optics are mounted to a 1/4 inch, aluminum plate that is cooled to 4 Kelvin. The plate is bolted to the lip of the 4 K shell and offset from the 40 K plate with a large G-10 ring. G-10 material provides high strength and low thermal conductivity, making it a good material for cryogenic offsets between different temperature stages.

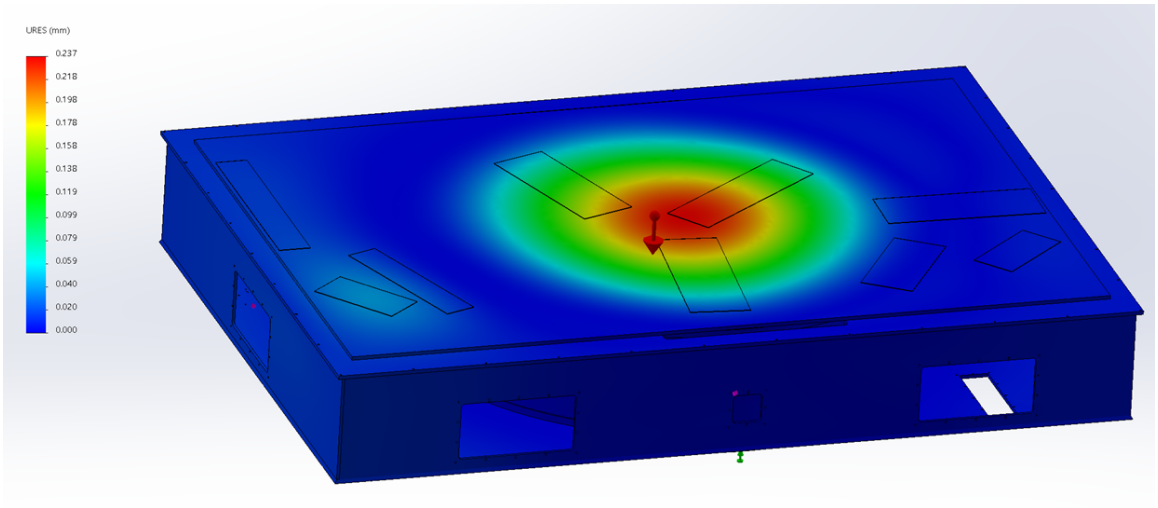

Figure 13. CAD static deflection analysis for the cold optics plate.

Figure 13 shows the CAD static deflection analysis for the 4 K plate supported by both the G-10 ring and 4 K shell. To simplify the mesh used in the analysis, I represented each of the cold optics components as remote masses applied at a the rectangular footprint of each mount. The largest deflection of 0.237 mm occurs in the center of the plate. Using the following equation, the angular deflection of the optics can be calculated:

$$\theta = \arcsin \frac{\Delta}{H} \tag{2.7}$$

In this equation Δ is the deflection and H is the height. Using the height of the optics affected by this deflection, 344 mm, the calculated angular deflection is 0.04 degrees which is less than the 0.1 degree requirement for the optics.

The positions of the optics are controlled using dowel pins to align the mounts on the optics plate. The positions of the dowel pin holes were specified with a high precision to the manufacturers. Cut outs on the plate were added for the coaxial cables and the wiring of the detector arrays. Figure 14 shows the CAD model and the final image of the optics components installed in the TolTEC cryostat.

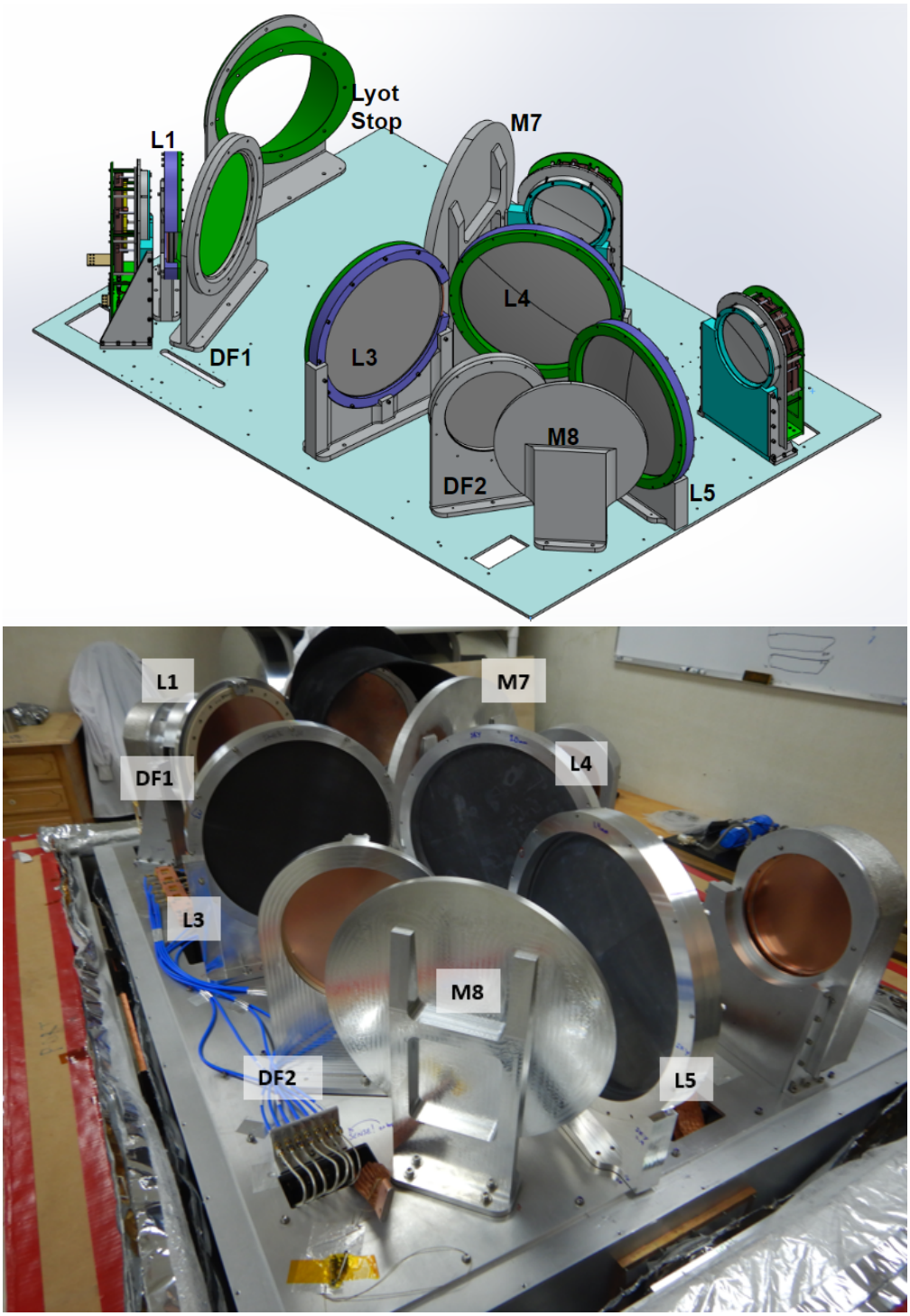

Figure 14. Top image shows the final CAD model of the cold optics mounts. Bottom image shows the cold optics installed at the site.

Table 6. Masses of the Warm Optics Before and After Light-weighting.

Mirror	Initial Mass (kg)	Final Mass (kg)	Reduction
M4	103.31	21.75	79%
M5	38.55	9.12	76%
M6	47.98	11.17	77%

2.5 Warm Optics Components

TolTEC's warm optics consist of the three mirrors that direct the light from the telescope into the cryostat. The first step in designing these mirrors is to import the Zemax optics model into Solidworks to create a CAD model. This model shows the correct sizes, curvatures, and placements of the mirror surfaces to build designs around. The largest of these mirrors has a diameter of approximately 1 m. Since these aluminum mirrors are large, they would end up being heavy and hard to mount in the telescope. To reduce the weight a hexagonal pattern was cut into the back of the mirror to significantly reduce the mass while maintaining the rigidity. Figure 15 shows the transition from a solid mirror to a light-weighted mirror. With this method, M4 went from an initial mass of 103.31 kg to a final mass of 21.75 kg. This is a mass reduction of 79%. The other warm mirrors experienced similar mass reductions using this light-weighting method. Table 6 shows the mass reductions for each of the mirrors. All mirror designs include 10 mm x 10 mm tabs on the top, bottom and both sides of the mirrors shown in Figure 16. These tabs create a flat plane at the front of the mirror that can be used as a reference for measurements. Each mirror is mounted with three bolts in a triangle formation on the back of the mirror. The three points of contact constrain the mirror to prevent translational and rotational movement of the mirror (Lunde et al. 2020).

After finalizing the mirror designs, the CAD model of the optics was added to a

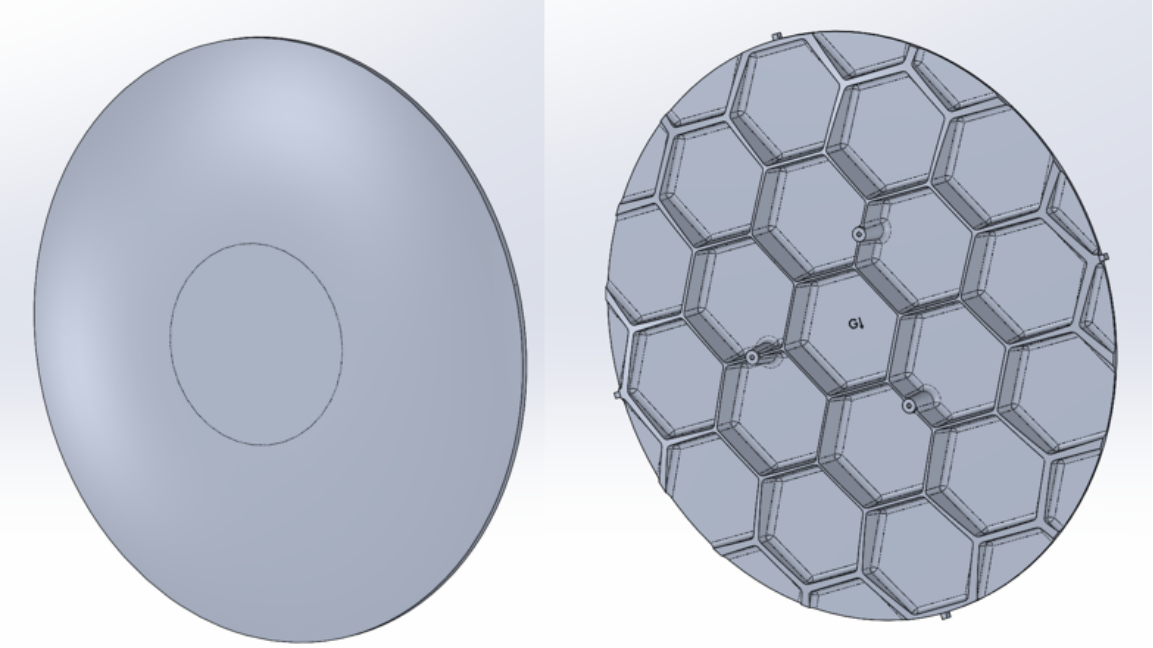

Figure 15. CAD drawings of M4. Shows the transition from solid to light-weighted mirror.(Lunde et al. 2020)

CAD model of the LMT receiver cabin by lining up the center of M3 from the optics file with the center of tertiary mirror in the LMT model. A welded structure was then designed to hold the mirrors at the correct positions inside the receiver cabin. The length and height of the welded structure are determined by the locations of the mirrors. The locations of possible structural beams are constrained by the optics beams and the walls in the LMT cabin. The beams can be seen in Figure 5. The following sections describe the static and vibration analyses performed to determine the optimal support structure for the warm optics and their adjustment mechanism (Lunde et al. 2020).

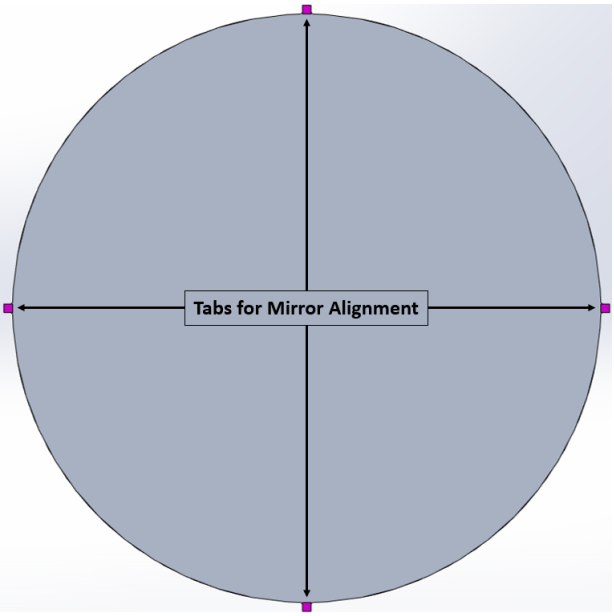

Figure 16. CAD drawing of M5. Shows the four tabs for mirror alignment in pink.

2.5.1 Tip-tilt mechanism

Since the warm mirrors are larger and outside of the cryostat, an adjuster could be designed to correct the angular positions of the mirrors around two axes. This mechanism should change the mirror angle by ±3 degrees with an accuracy of 0.1 degrees to achieve the desired angular tolerance. Figure 17 shows the first iteration of the tip-tilt mechanism that was installed on the mirrors. The tip-tilt consists of three plates, two perpendicular axes of rotation, and two adjusters. The L-shaped, center plate sets the distance the adjuster is from the rotational axis to provide the desired adjustment accuracy. With this mechanism, the x and y rotations are independent of each other. The ball-joint end rods used in the adjuster have a pitch of 0.8 mm which provides a 0.1 degree change per quarter turn. A tip-tilt was mounted to the back of each warm mirror using the three bolt holes on the back of the mirror shown in Figure 15. The triangular plates provide easy axis to the mounting points.

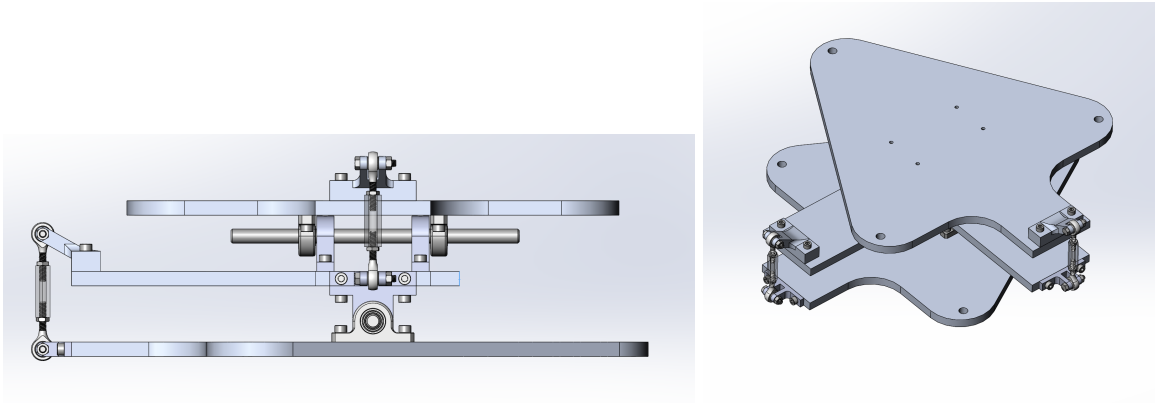

Figure 17. The left image is a side view of the original tip-tilt mechanism (Lunde et al. 2020). The right image is an isotropic view that shows the shape of the plates.

Unfortunately during the assembly of the warm optics at the LMT, there were significant vibrations in the mirrors. This was most noticeable in the largest mirror, M4. These vibrations were due to small gaps that are designed into the bearings to allow them to rotate. To reduce the vibrations, a second adjuster mechanism was added to act as a clamp for each pair of plates. Figure 18 shows the final tip-tilt design currently being used at the LMT. To change the angle of the plates, the two adjusters must be turned in opposite directions by the same amount. This must be done in small steps to avoid binding the threads and flexing the plates. Foam was also added between the plates after the mirrors were aligned to dampen any residual vibration modes.

2.5.2 Static deflection analysis

The angular misalignment of the optics was determined by performing a static analysis to determine how much a component bends under gravity. The static analysis was done using the Solidworks simulation tool. Figure 19 shows the simulation results

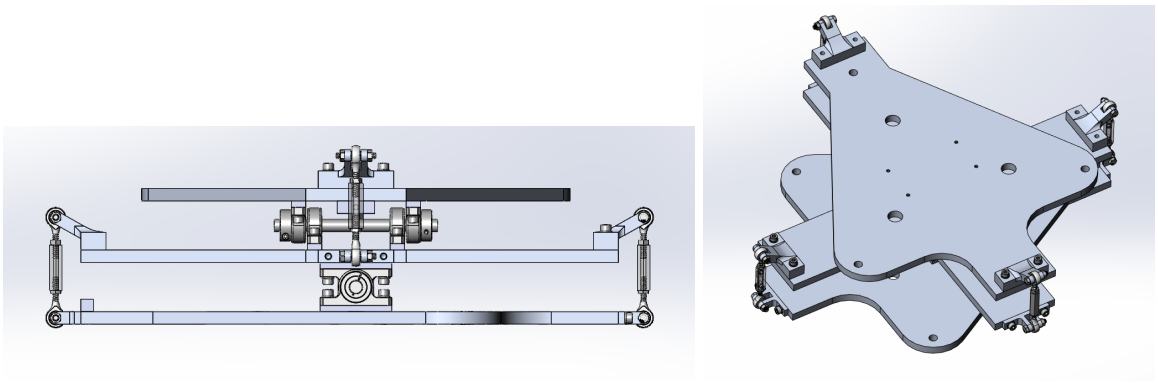

Figure 18. The left image is a side view of the final tip-tilt mechanism (Lunde et al. 2022). The right image is an isotropic view that shows the shape of the plates.

for the M4/M6 mount and the M5 mount. The simulation shows the magnitude, in millimeters, and direction of the mount deflection. The maximum angular deflection can be determined by fixing the base of the mount and calculating the angle using equation 2.7 as previously done. For the M4/M6 mount, the max deflection of 0.079 mm occurs at the height of the M4 mirror. Using the mirror height of 1620 mm, the angular deflection is only 0.003 degrees. For the M5 mount, the max deflection is 0.0094 mm. With a height of 530 mm, the angular deflection is 0.001 degrees. These deflections are within the 0.1 degree requirement for the warm optics mounts.

2.5.3 Resonance frequency analysis

Every structure vibrates in the presence of external forces or vibrations. The frequency a structure vibrates at is referred to as its natural frequency. The primary mirror of the LMT moves and causes vibrations in the receiver cabin. If these vibrations match the optics mount's natural frequency, the structure will resonate causing large deflections. The dominant resonant frequency of the LMT is between 3-5 Hz. All

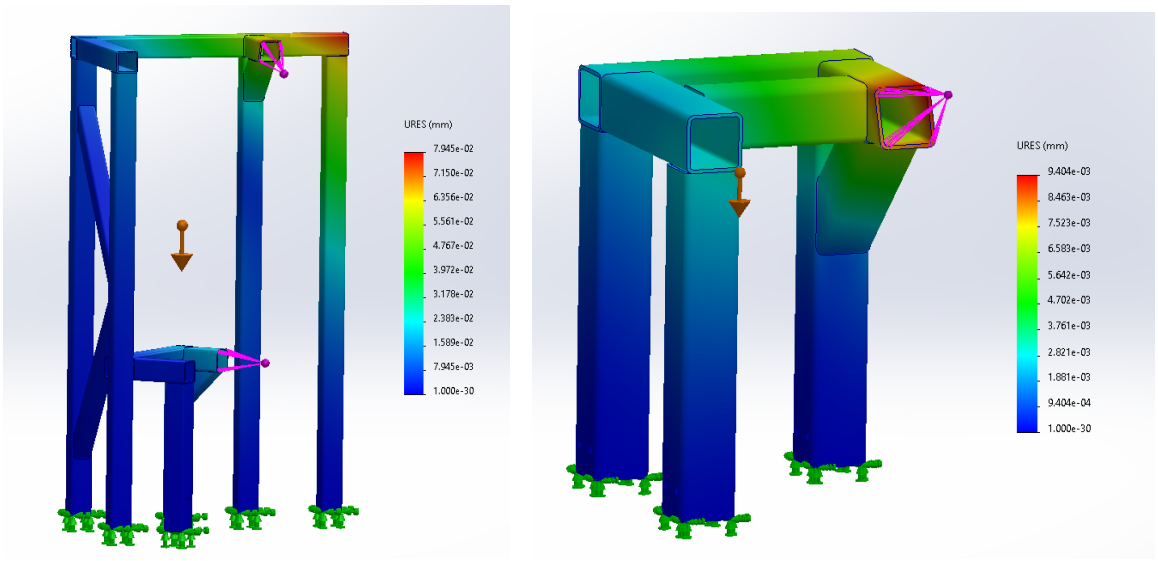

Figure 19. The left image shows the static analysis results for the M4/M6 mount. The right image shows the result for the M5 mount.

the mounts must have their first mode natural frequency greater than 20 Hz, to have more than an order of magnitude reduction to any mechanically coupled vibrations in the optics. This analysis was also completed for the cold optics mounts. Since each of the cold optics mounts are small, all of the primary frequency modes were above 100 Hz. This meant no additional changes needed to be made to the cold optics mount designs.

The Solidworks vibrational analysis tool calculates the natural frequency modes of a model. Figure 20 shows the applied loads and fixed points for the analysis of the two mounting structures. The red arrow represents the direction of gravity. The green and orange arrows at the bottom of the mount show the reaction forces on the surfaces of the mount that are fixed to the table. Since the tip-tilt mechanism and light-weighted mirror are complex structures attached to the mount, the mesh used in the calculations is too complicated to run. I simplified the analysis by calculating the moment of inertia and center of mass of the mirror relative to a common axis

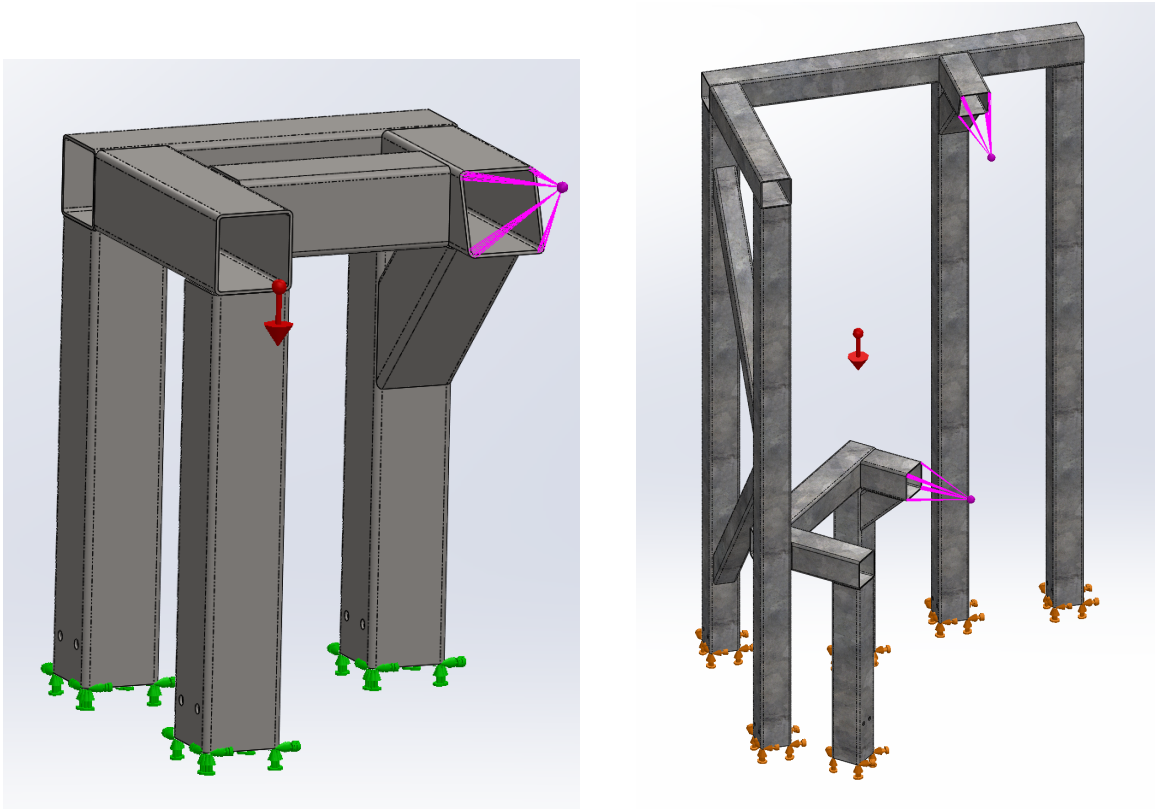

Figure 20. These CAD models show the loads and fixtures for the vibration analysis of the M5 mount (left) and the M4/M6 mount (right).

located at the top corner of the mounts. This can be applied as an external load in the vibration analysis. The pink dot represents the center of mass of the mirror that is coupled to the mount.

Since the warm optics mounts are designed to hold large mirrors high above the ground, these mounts were more complicated to design. The resonant frequencies of structures are affected by mass, height, and moment of inertia. Figure 21 shows a cantilever beam with a mass concentrated at one end to represent a simplified model of a mirror mount used to convey general ideas about how different parameters affect the resonant frequencies of structures. The resonant frequency of this system can be

Table 7. First Five Resonant Frequency Modes for the Final TolTEC Warm Optics Designs.

Object	Mode 1 (Hz)	Mode 2 (Hz)	Mode 3 (Hz)	Mode 4 (Hz)	Mode 5 (Hz)
M4	101.8	102.2	176.1	182.1	226.1
M5	222.2	222.7	326.1	331.8	524.2
M6	160.6	237.0	305.2	319.2	403.9
M5 Mount	69.92	85.59	112.6	182.6	208.4
M4/M6 Mount	17.37	21.52	27.89	30.48	32.62

estimated using the following equation from ToolBox 2017:

$$f = \frac{1}{2\pi}\sqrt{\frac{3EI}{ML^3}} \tag{2.8}$$

where M is the weight of the mirror, L is the height of the mount, E is the elastic modulus of the mount material, and I is the area moment of inertia. The natural frequency is increased by decreasing the height, decreasing the weights, and increasing the moment of inertia. The mass of the warm mirrors has already been reduced. The height of the mirrors is defined by the optical path. This leaves increasing the moment of inertia as the only option. The moment of inertia increase can be achieved by changing the cross-sectional shape of the steel tubing or by adding a structural beams that work designed to cancel out certain resonance modes. For example, the original frequency mode of M5 was approximately 20 Hz. By adding a beam across the top of the mount, I was able to increase the frequency to 27 Hz. Then by increasing the size of the steel tubing to 3.5x3.5 inch squares, I increased the frequency to 70 Hz. The M5 mount was completed after three design iterations. Figure 22 shows the vibration analysis results for the final M5 mount design. Exaggerated deflections show the shape of the first 5 resonance modes. The displacement results are normalized to show the resultant amplitude (AMPRES) (Kurowski 2022b).

However, the combined M4/M6 mount was more challenging. The bottom CAD

Figure 21. The mirror mount can be simplified as a cantilever beam with a mass concentrated at the end.

models in figure 23 show the simulation result for the final M4/M6 mount. Again, exaggerated deflections show the shape of the first 5 resonance modes in units of AMPRES. The lowest mode resonance is a rocking motion of the position of M4. After many different design attempts, the maximum resonant frequency reached for this mount is 17 Hz. This was determined to be good enough because it gives a factor of safety of 3.5 above the vibrations in the telescope.

The vibration analysis was also completed for each of the warm mirrors separately to ensure the rigidity of the mirrors. Since the large mirrors are held near their centers, there is the possibility of vibration modes around the mounting point. Figure 24 shows the vibration analysis for the warm mirrors. The green arrows show the fixed mounting points of the mirrors. These are the three points near the center where the mirrors are bolted to the three mirrors. The orange arrows show the direction of gravity, which changes depending on the angle at which each mirror is held. Table 7 lists the resonance frequencies of the first 5 modes for the warm optics mounts and mirrors. All but the first mode resonance of the M4/M6 mount meet the design requirement of 20 Hz.

After the optics were installed at the LMT, the vibrations of M4, M5 and M6 were

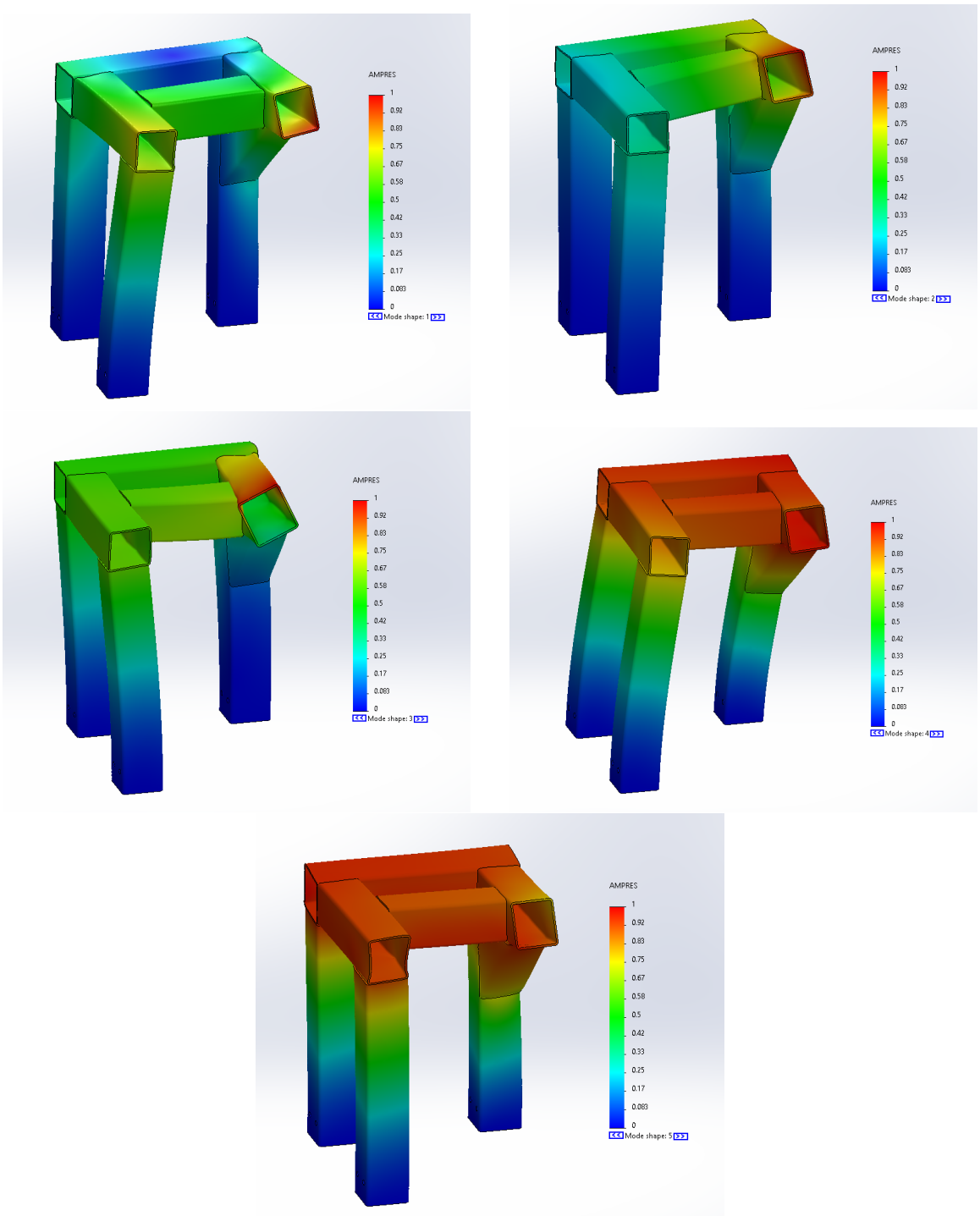

Figure 22. Vibration analysis for the mount that holds M5. Shows the shape of the first 5 resonance modes.

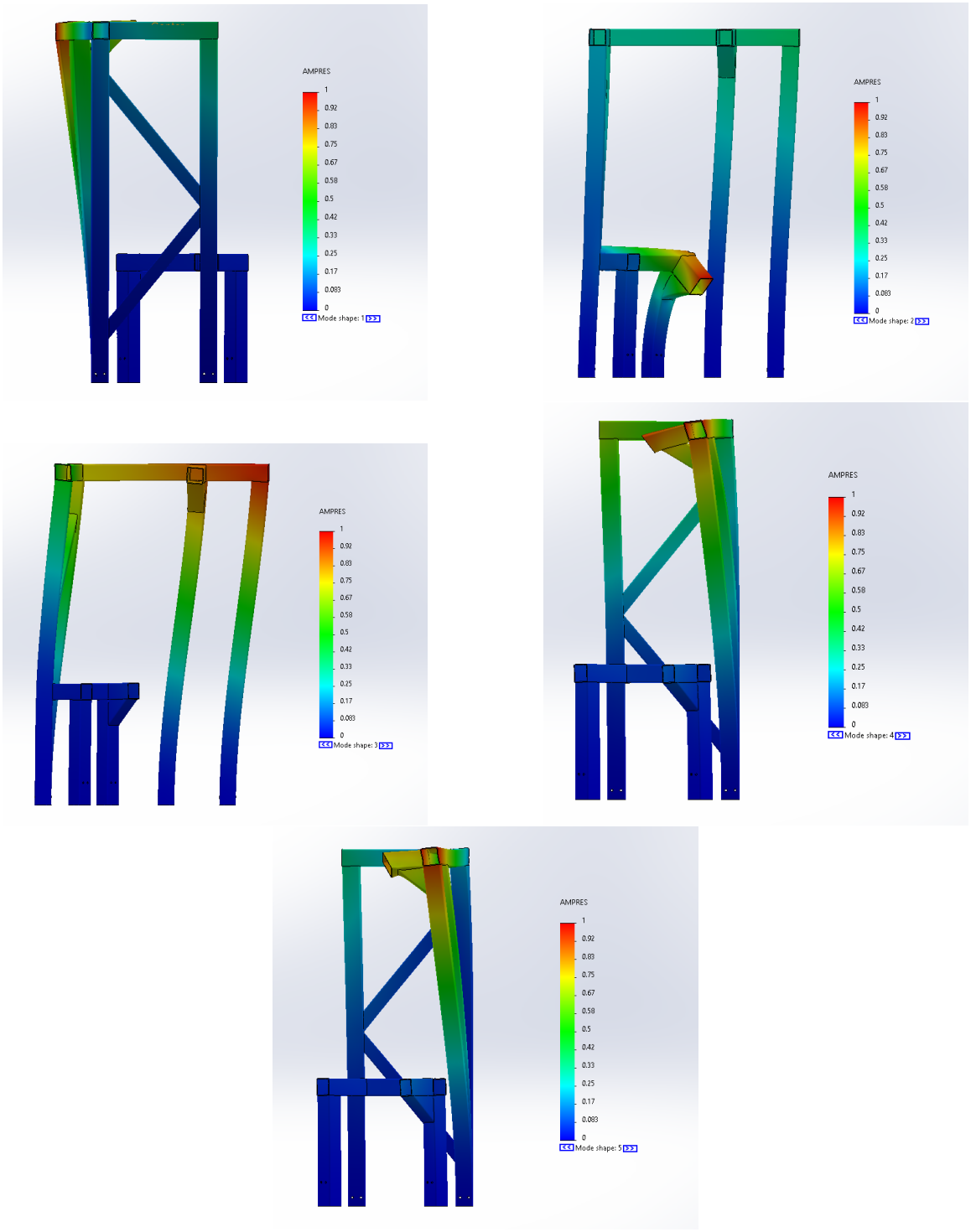

Figure 23. Vibration analysis for the mount that holds M4 and M6. Shows the shape of the first 5 resonance modes. The deflection is exaggerated to show the shape of the primary resonant mode.

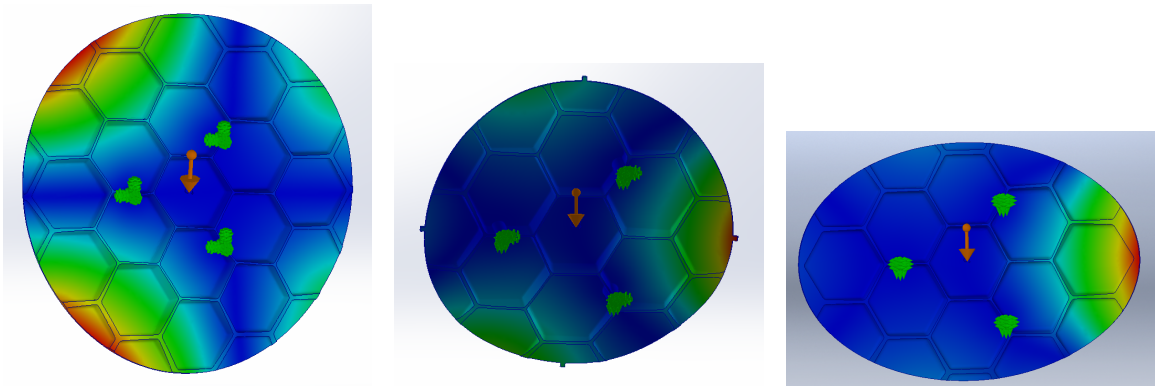

Figure 24. Vibration analysis for all three warm mirrors. Shows the first resonant modes for each of the mirrors. From left to right: M4, M5, M6.

measured using an MPU6500 accelerometer. This 14 bit ADC has a range of ±2g. Where g is the acceleration due to Earth's gravity, $9.81 m/s^2$. With an accelerometer attached to each mirror, a 200 second timestream of data was taken. I divided the timestream into 5 second samples and performed a Fast Fourier Transform (FFT) to get the power spectra of the data. These samples were then averaged to reduce the noise. Figure 25 shows the results of this analysis. M4 has peaks around 56 Hz. M5 has peaks at 24 Hz and 120 Hz. While M6 appears to have no major peaks. All of these frequencies are higher than the design goal of 20 Hz.

With the warm optics mounts and tip-tilt were finalized, the warm optics were connected to a table structure. This allows the warm optics to be aligned before being mounted in the telescope. Figure 26 shows the completed CAD design and an image of the optics installed in the receiver cabin at the telescope.

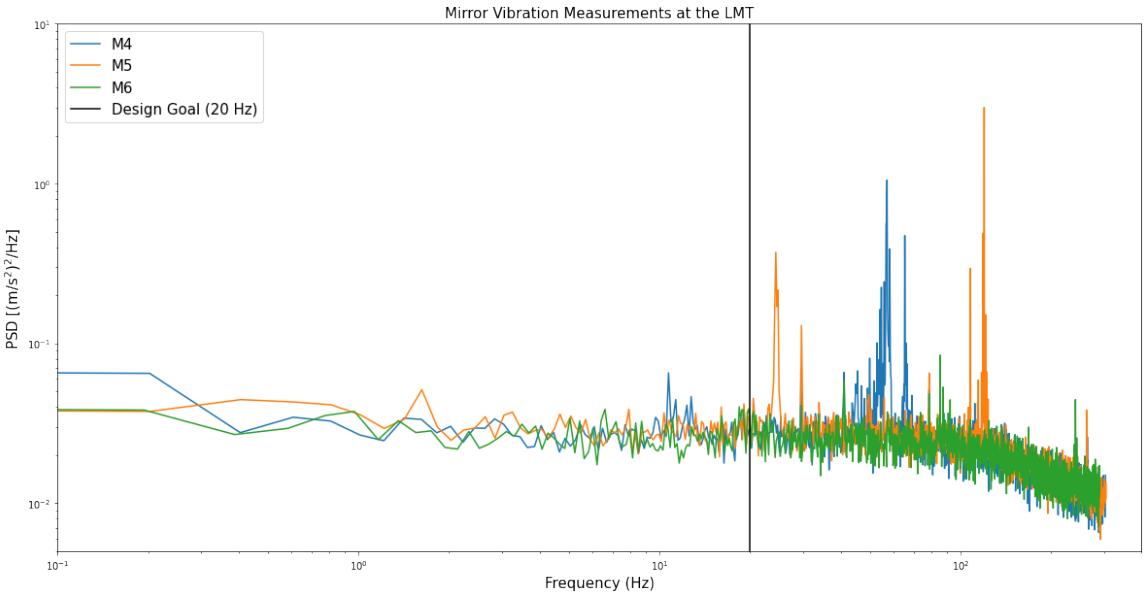

Figure 25. This plot shows the vibration measurements of the mirrors at the LMT.

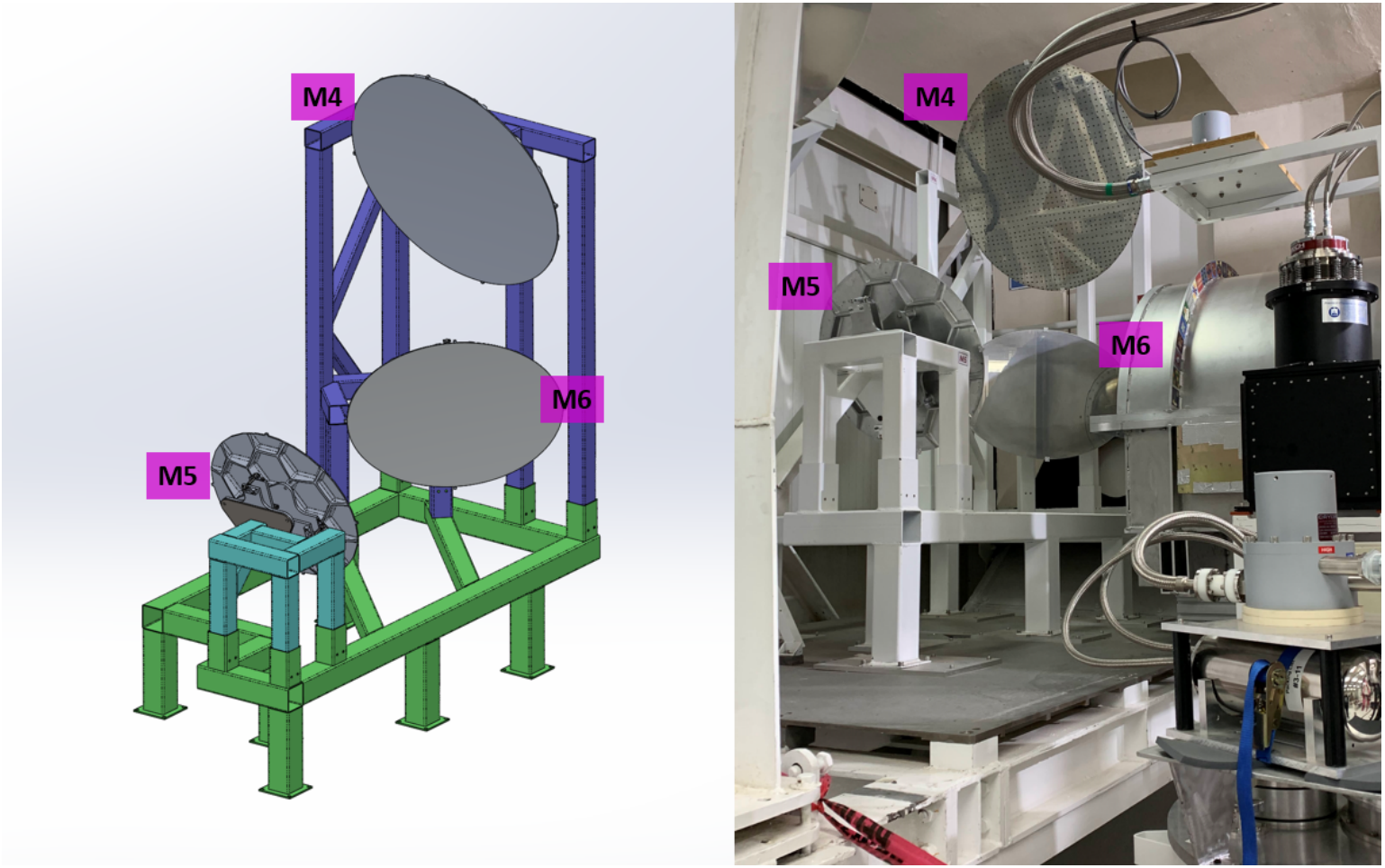

Figure 26. Left image shows the final CAD model of the warm optics. Right image shows the warm optics at the LMT.

Chapter 3

OPTICAL ALIGNMENT AND CHARACTERIZATION OF TOLTEC

3.1 Trips to the LMT

My first trip to the LMT was for the initial installation of TolTEC in November of 2021. This included assembling the TolTEC cryostat, mounting the cold optics and detectors on the 4 K plate, and mounting the warm optics in the LMT receiver cabin. The cold optics were successfully installed. The alignment of the cold optics system once bolted to the cold optics plate was verified in the lab at the University of Massachusetts before shipping TolTEC to Mexico. During the assembly of the warm optics, there were significant vibrations in the mirrors caused by the tip-tilt mechanism. Therefore, before significant work could be done on alignment, the tip-tilt had to be modified.

May of 2022 marked my second trip to the LMT to install the new tip-tilt mechanism and begin the optical alignment of the warm optics. The first step was to measure the mirror positions with the laser theodolite and adjust the angles to match the solidworks model. Then a laser was traced through the warm optics from the cryostat window. Minor adjustments were made to the mirrors to center the laser on each of the mirrors.

During some on sky measurements in the summer, one of the tip-tilt adjusters was broken. It was a simple fix, since replacement parts could be salvaged from the original tip-tilt. This began the planning of my final trip to the LMT in November of 2022 to ensure that the optics were still aligned and take measurements of the optics

beam for characterization. Timestreams of a liquid nitrogen source were used to align the optics and a modulated infrared (IR) source attached to a robot arm (Wyatt) was used to map the beam.

3.2 Optics Zemax Analysis

Zemax was used in both the design and characterization of the TolTEC optics. One of the requirements for the TolTEC camera was to have a Strehl ratio greater than 0.9 over the full field at all wavelengths. The Strehl ratio measures the effect wavefront aberrations from atmosphere or optics aberrations have on image quality. It is calculated in Zemax by dividing the peak intensity of the diffraction point spread function (PSF) by the peak intensity of the diffraction PSF if there were no aberrations (Zemax 2011). This gives a measure of optical image quality if the TolTEC camera was diffraction limited. Figure 27 shows the Strehl ratio over the full field for the 1.1 mm band. Figure 28 shows the Strehl ratio for the 1.4 mm and 2.0 mm bands. The contours on the plots are drawn with one percent intervals and the axis units are in degrees. The purple circles show the 4 arcminute field of view of the arrays. The minimum Strehl ratio value within the circle is 0.95 for all three frequency bands. This is greater than the design requirement of 0.9.

Footprint diagrams show the footprint of the beam on any surface defined in the Zemax model. I used footprint diagrams to check the surface apertures of the optical components and illumination overlap on the primary mirror. The illumination overlap requirement is 90%. I interpreted this as the percentage of the area each beam should overlap the other beams. Footprint diagrams are created through the Zemax ray tracing procedure which calculates how bundles of rays move through

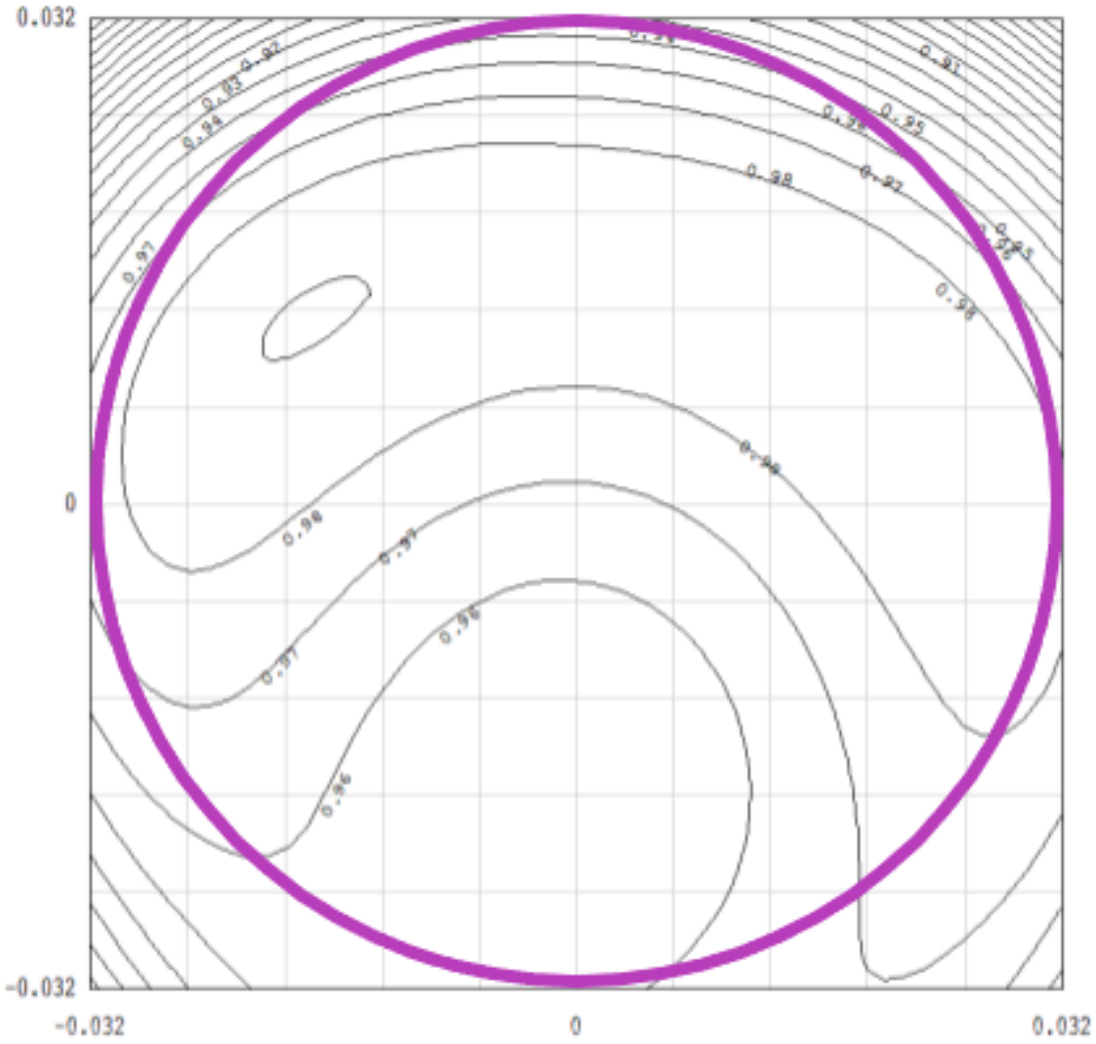

Figure 27. Strehl ratio plot over the full field for the 1.1 mm band. The circle shows the approximate diameter of the array that covers about 4 arcminutes.

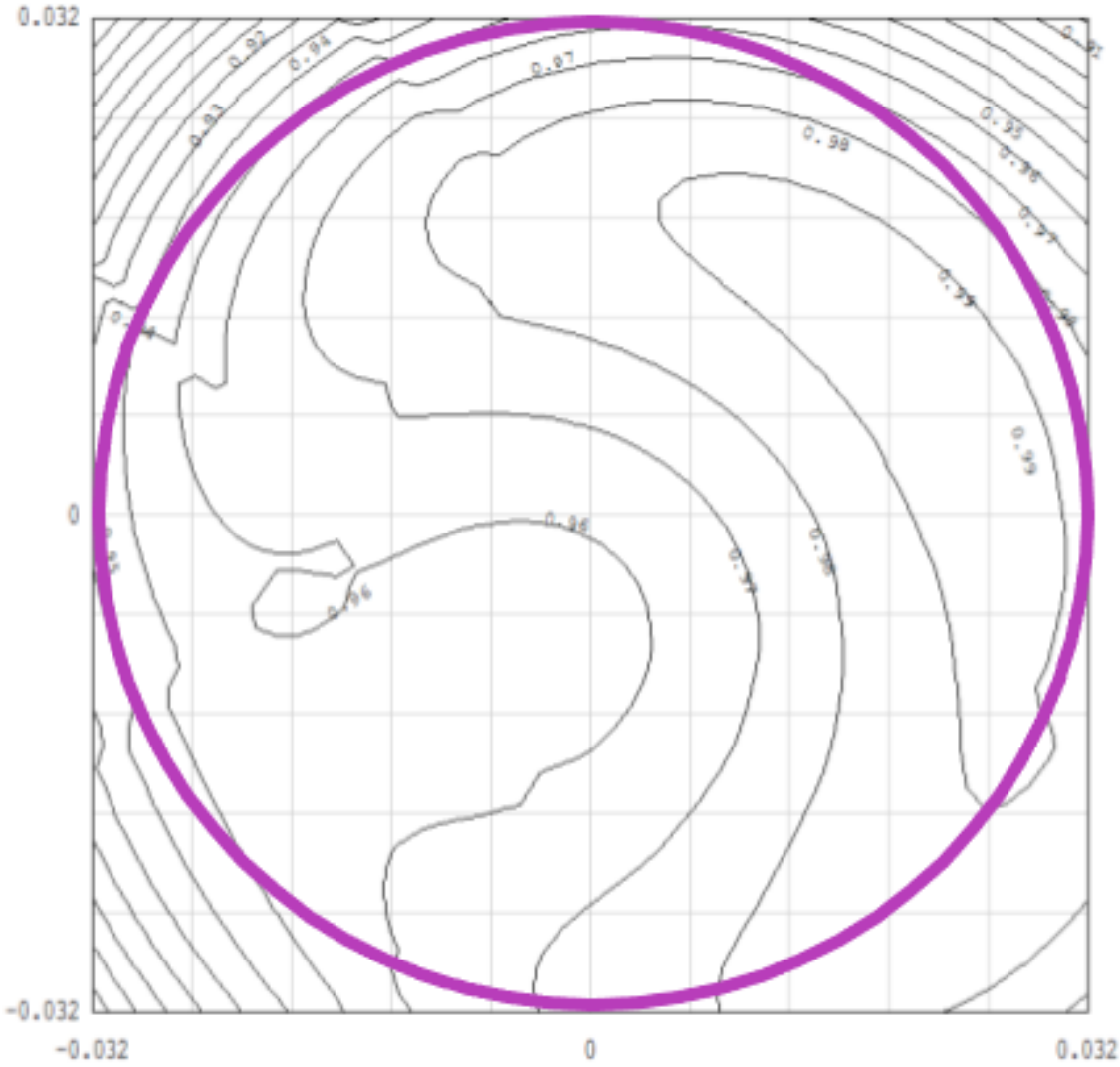

Figure 28. Strehl ratio plot over the full field for the 1.4 mm and 2.0 mm bands. The circle shows the approximate diameter of the array that covers about 4 arcminutes.

the optical system and are affected by each optical component. Figure 29 shows the beam footprint on the primary mirror of the LMT. The aperture (black circle) has a 50000 mm diameter. This is the diameter of the primary mirror. The colorful circles show the footprints of each set of rays. The outer diameter of this bundle of circles is 47460 mm and the inner diameter is 43680 mm. I then calculated the ratio of the area (A) of circles with these diameters to determine the what percent of the overlap occurs using the following equation:

$$AreaRatio = \frac{A_{inside}}{A_{outside}} = \frac{(D_{inside})^2}{(D_{outside})^2} \tag{3.1}$$

To have 90% beam overlap, the outside and inside areas should be within 90% of the average area. The following statements must be true:

$$A_{avg} > 0.9A_{outside} \tag{3.2}$$

$$A_{inside} > 0.9A_{avg} \tag{3.3}$$

Combining equations 3.2 and 3.3 by substituting for the average area gives the following requirement:

$$A_{inside} > 0.81A_{outside} \rightarrow \frac{(D_{inside})^2}{(D_{outside})^2} > 0.81 \tag{3.4}$$

The ratio of the inner and outer diameter areas for the bundle of rays should be greater than 81% to meet the illumination overlap requirement. This ratio for TolTEC is 85% which meets this requirement.

I also used footprint diagrams to ensure the clear aperture diameters of the silicon lenses were less than 30 cm. As a default in Zemax, if no aperture is defined at a surface, the footprint diagram will draw a circular aperture with a diameter equal to its radial clear aperture value (Zemax 2011). Figure 30 shows the footprint diagrams of the five cold lenses. L4 and L5 are identical lenses with identical footprints, therefore,

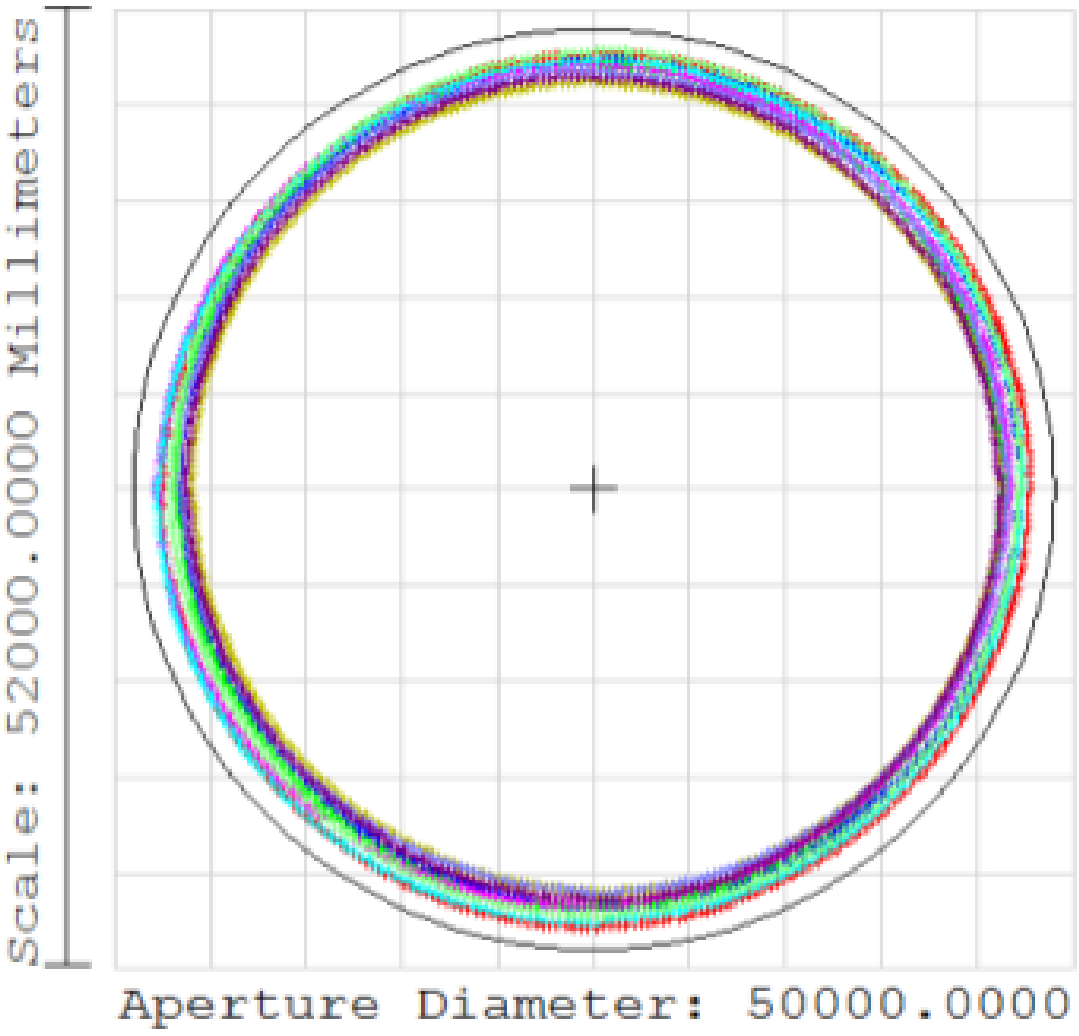

Figure 29. Zemax beam footprint with overlapping beams on the primary mirror of the LMT.

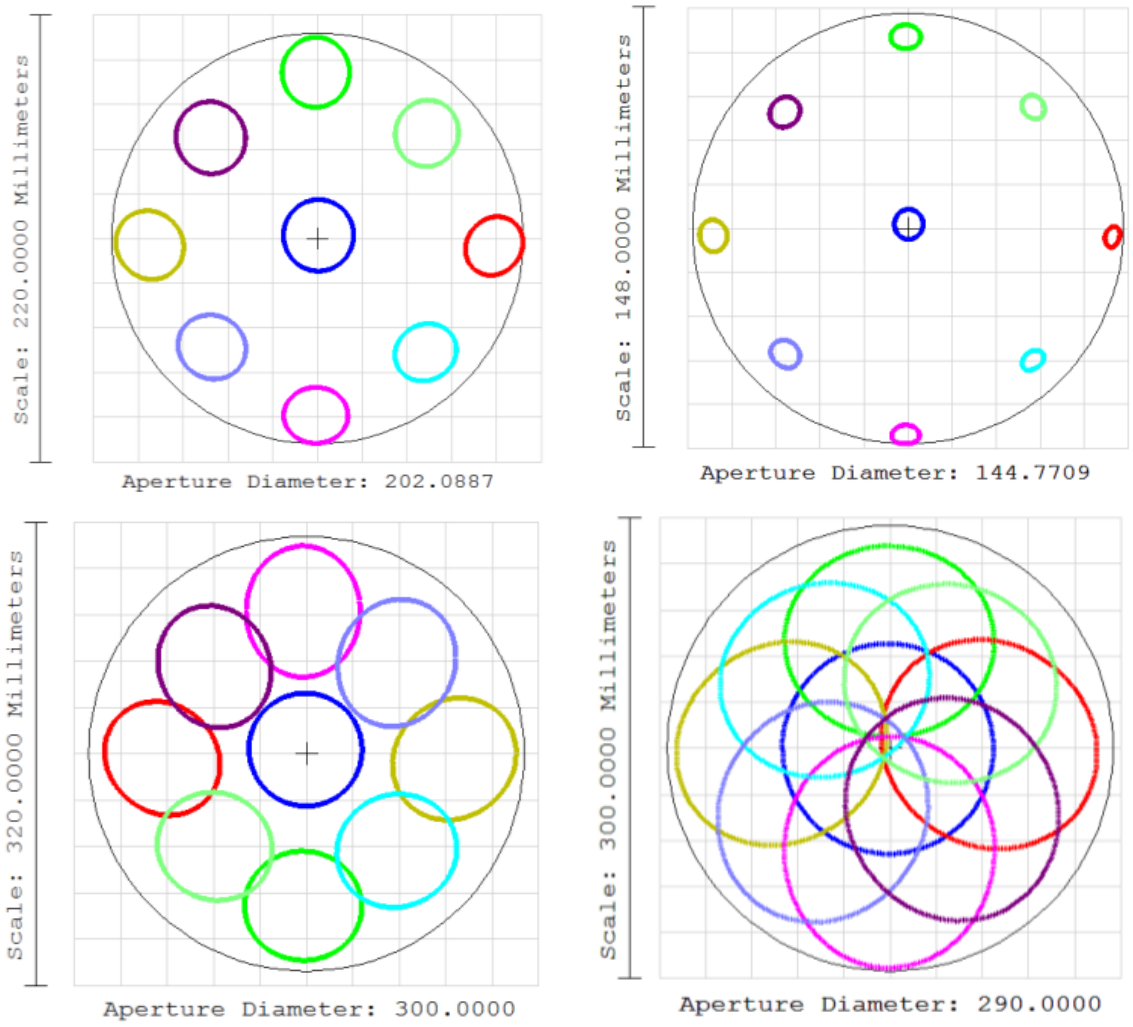

Figure 30. Zemax beam footprints for each of the cold lenses: L1, L2, L3 and L4/L5.

the last plot represents both these lenses. The aperture diameters shown for the top footprints (L1 and L2) are the clear aperture value since no aperture was defined. The bottom footprints had apertures defined. In all cases, the beam footprints shown do not exceed an aperture of 300 mm.

Spot diagrams are another method to evaluate image quality of an optical system. Zemax creates spot diagrams by ray tracing bundles of rays from the object (a spot of light) through the optical components to the detector plane. This is done for objects

at the center and around the edges of the field of view. The image is compared to the radius of the first dark ring of the Airy disk, which is the diffraction pattern for the circular, uniformly illuminated primary mirror assuming perfect optics. A diffraction limited system has all the rays within the Airy disk. Zemax calculates both a RMS spot radius and a GEO spot radius. RMS spot radius is the root-mean-square distance between each ray and the central reference point, giving an idea of the spread of the rays. The GEO spot radius is the geometric measurement of the distance between the central reference point and the ray farthest from the center (Zemax 2011). Spot diagrams should be used alongside other optical analyses to characterize the system.

Figure 31 shows the spot diagram results for the 1.1 mm band. The Airy disk radius is 3449 μm and all the spots fall within the shown circle. Figure 32 shows the spot diagram results for the 1.4 mm and 2.0 mm bands. The Airy disk radius is 4202 μm. All of the spots are smaller than the Airy disk but a few lie on the edge. Looking at the RMS spot radius, the rays on average fall within the Airy disk.

The Zemax beam field analysis was done on a reversed field model of the TolTEC optics. The Zemax beams at defined surfaces were calculated using the Zemax physical optics propagation tool. The time-reversed model was used since I had a Gaussian beam with parameters calculated from the detector feed-horn design (Austermann et al. 2018). The physical optics analysis propagates the initial Gaussian beam starting at the detector location up to the primary mirror. The analysis outputs the calculations for each defined surface in the optics model. The model looks at the 1.1 mm wavelength band since I performed all liquid nitrogen and Wyatt map tests using data from the 1.1 mm detector array. This tool propagates the electric fields through free space using diffraction calculations of the wavefront surface by surface

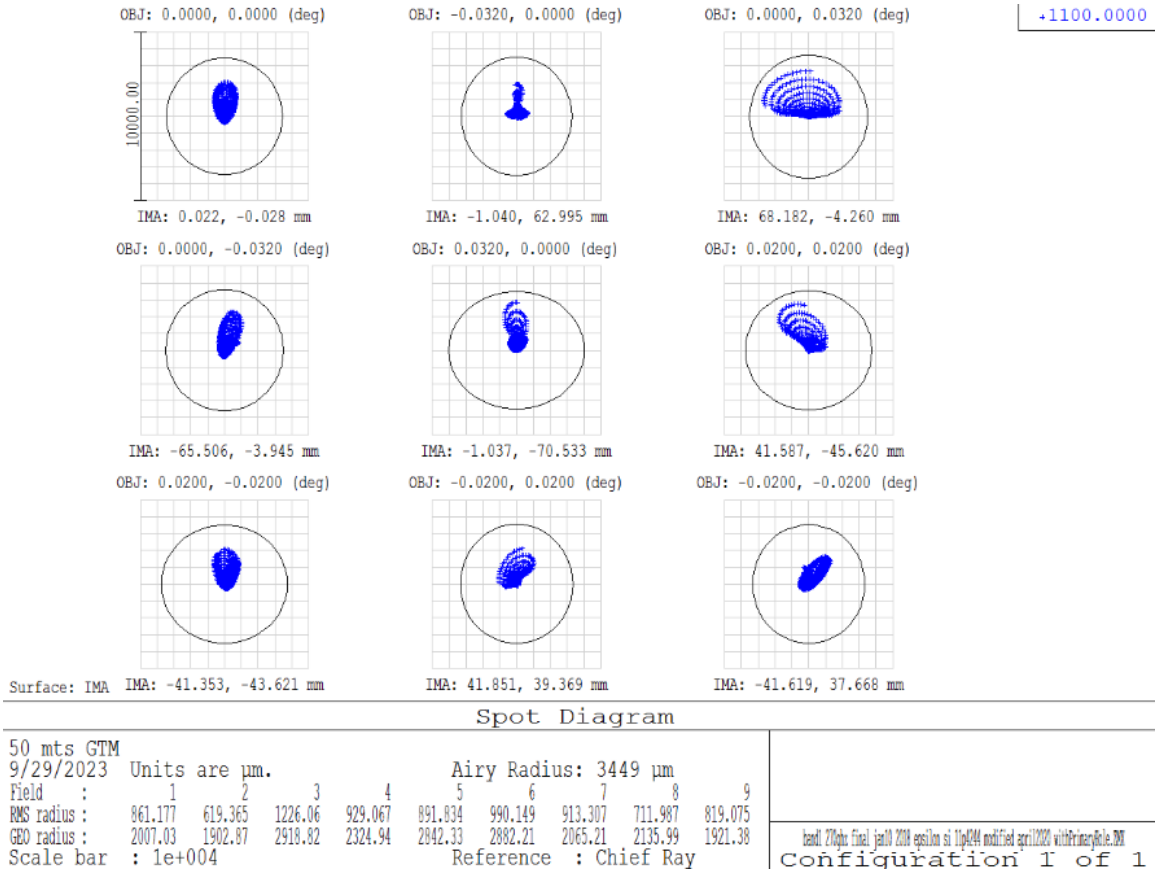

Figure 31. Zemax spot diagram for the 1.1 mm band for fields at the center and edges of the field of view.

through the system. The physical optics tool is sensitive to the Fresnel propagation process.

Figure 33 shows the simulated Zemax beams at the three different locations along the optical axis where I collected data from the TolTEC system at the LMT. The first beam was at a surface 640 mm in front of M4. This beam has a distinct annular shape with the inner bright ring having a diameter of about 50 mm. The second surface was between M3 and the Cassegrain focus at a distance of approximately 900 mm in front of the Cassegrain focus. This beam has a circular shape with a diameter of about

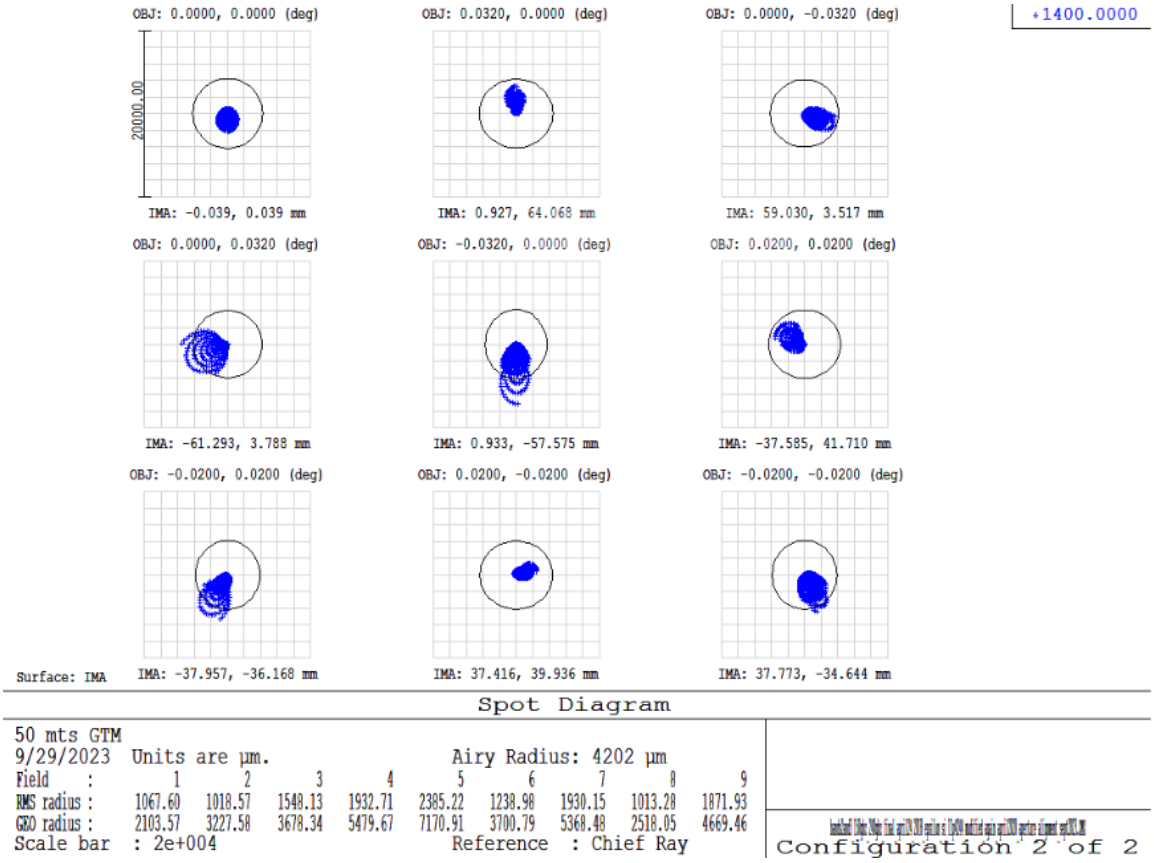

Figure 32. Zemax spot diagram for the 1.4 mm and 2.0 mm bands for fields at the center and edges of the field of view.

40 mm. The third surface was directly on the surface of M3. This circular beam has a multiple ring diffraction pattern with an outer diameter of about 200 mm.

Since I was unsure of the exact location along the beam that I measured the beam with the IR source, I measured the beam in Zemax at multiple locations between the Cassegrain focus and M3. Figure 34 shows the radial profiles at the different locations around 900 mm from the Cassegrain focus which is my estimated location of the IR beam. As the surface moves closer to the Cassegrain focus, the beam diameter is reduced and the center of the beam gets brighter as the beams converge at this location.

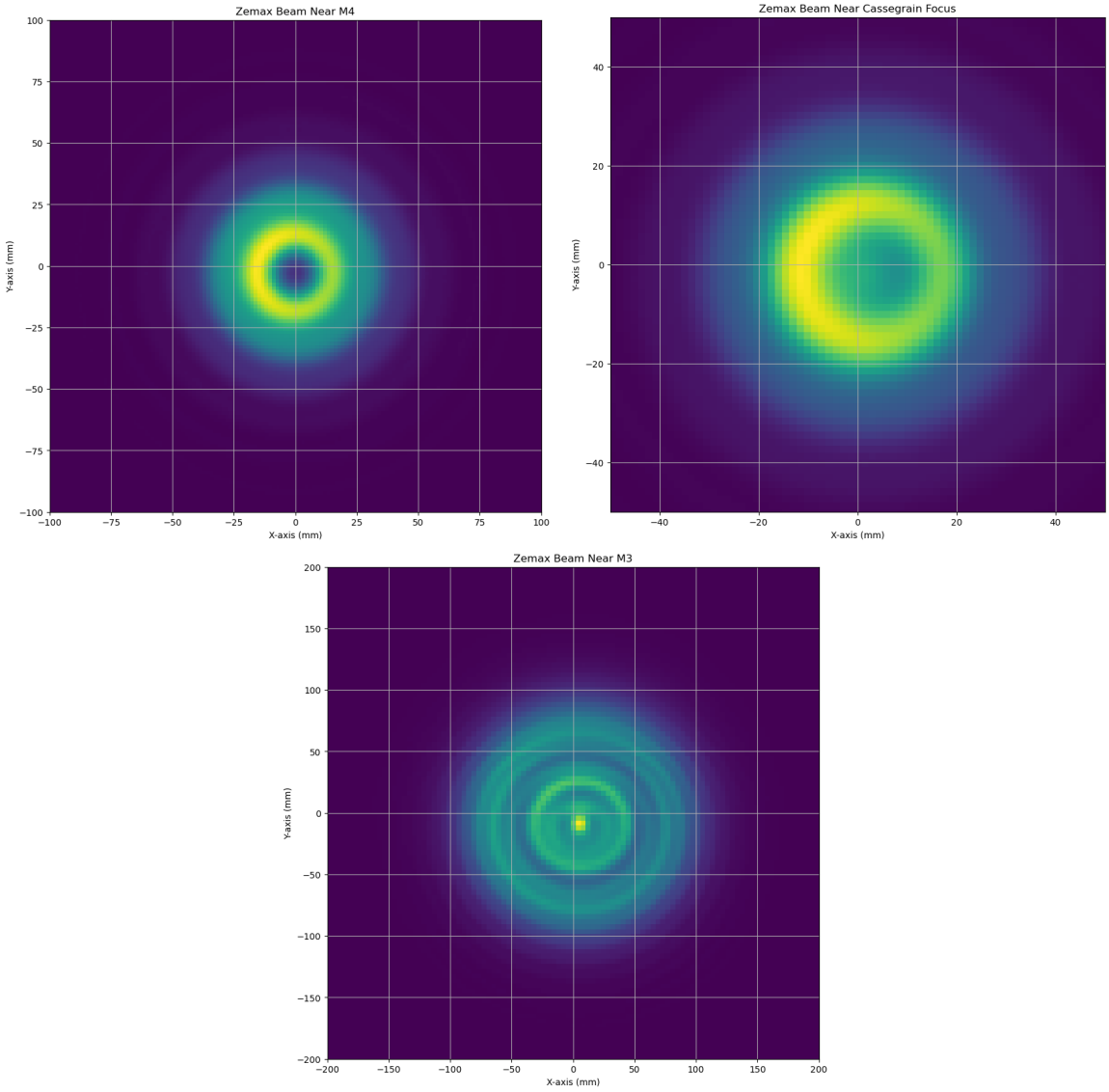

Figure 33. Zemax physical optics simulations for beams at different locations along the optical axis: near M4 (top left), near the Cassegrain focus (top right), and near M3 (bottom).

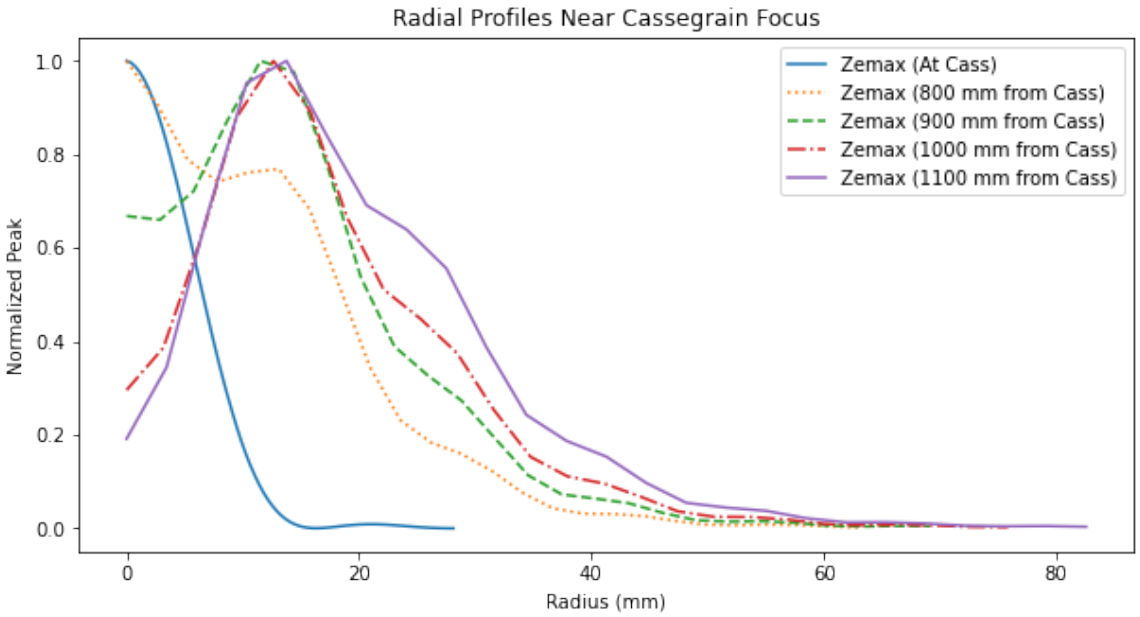

Figure 34. Radial profiles of the beam at locations near the Cassegrain focus.

3.3 Laser Theodolite Measurements

The mirror positions were measured with a laser theodolite after the warm optics were re-mounted in the receiver cabin. A theodolite is a precision instrument used to measure the x, y, and z positions of targets in reference to a zero point. The receiver cabin has a reference point on the floor directly under the center of M3. All the theodolite measurements were made relative to this point and then compared to the 3D CAD model of the warm optics. Each of the warm mirrors has four tabs around the perimeter. These tabs form a planar surface for the reflective theodolite targets to be attached. Figure 35 shows the locations of these targets on the mirrors. To be in view of the theodolite, the M5 targets were placed on the mirror tabs.

First, the tab locations of the mirrors in the CAD model were measured. Then the theodolite was used to measure the x, y, and z locations of the tabs in the receiver cabin. Using these locations, I calculated the angles of the mirror using equations 3.5

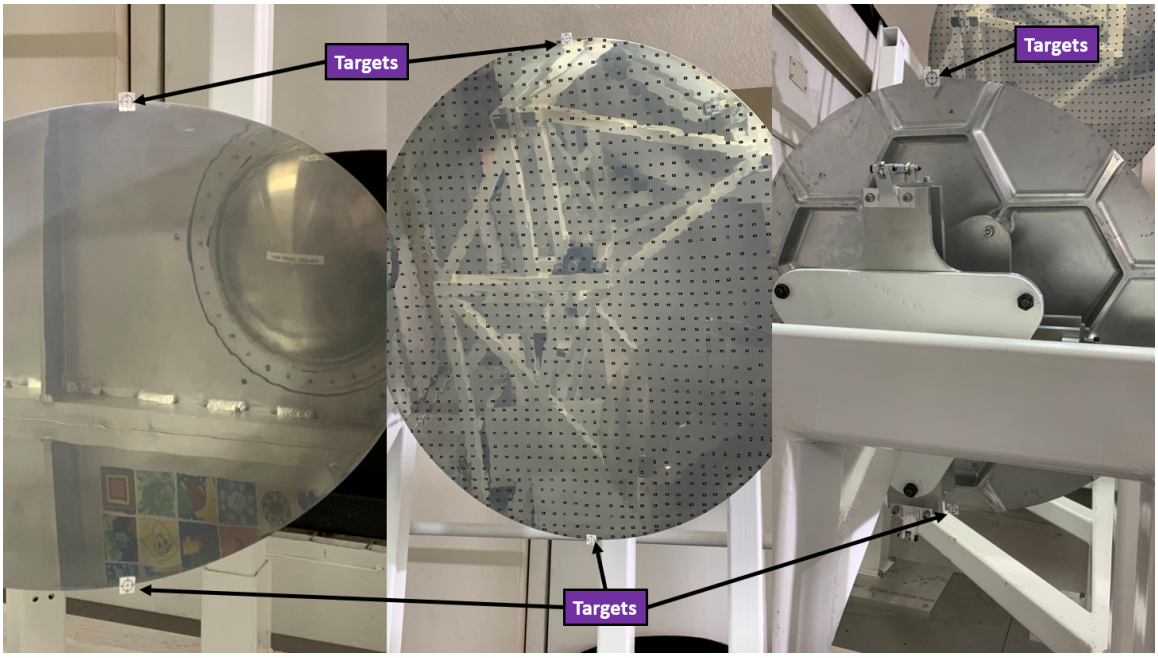

Figure 35. Locations of the laser theodolite targets on each of the warm mirrors (Lunde et al. 2022).

and 3.6 (Lunde et al. 2022). Theta is the angle about the horizontal axis and phi is the angle about the vertical axis. These are the angles that can be changed using the tip-tilt mechanism.

$$\theta = \arctan \frac{X_{top} - X_{bottom}}{Z_{top} - Z_{bottom}} \tag{3.5}$$

$$\phi = \arctan \frac{X_{left} - X_{right}}{Y_{left} - Y_{right}} \tag{3.6}$$

I calculated the angles for both the CAD model and the warm optics. Table 8 compares the Solidworks angles with the first and final measurements of the warm optics at the telescope. By finding the difference between the model angle and the real angle, I determined how much each of the mirrors needed to be adjusted. Using the tip-tilt, the vertical and horizontal angles were adjusted. These measurements and adjustments were repeated until the mirror angles were about 0.1 degrees of the model. Other methods were used to more accurately align the system since there are

Table 8. Laser Theodolite Measurements of Mirror Angles Compared to Solidworks.

Mirror	Direction	Solidworks (Degrees)	First Measurement (Degrees)	Final Measurement (Degrees)
M4	Vertical	-20.29	-20.32	-20.32
-	Horizontal	0.00	-0.30	0.02
M5	Vertical	-20.00	-18.71	-19.94
-	Horizontal	0.00	-0.36	-0.11
M6	Vertical	0.00	0.35	0.01
-	Horizontal	-45.34	-45.38	-45.39

small changes between the CAD model and the installed system due to manufacturing precision and changes made to the LMT receiver cabin.

3.4 Laser Alignment Plate

The next step in optical alignment was to use the laser alignment plate (LAP). The LAP holds a laser at the center point of the cryostat window where the center of the beam is located. Figure 36 shows the LAP mounted on the window of the cryostat. Since the cold optics are aligned with the window, this method was used to align the cryostat with the warm optics. The laser should reflect off the center of each mirror. The laser hit the center of M6 without having to adjust the cryostat position. M6 was adjusted to point the laser at the center of M5. This flat mirror was then adjusted to point at the center of M4. M4 was also adjusted to center the laser of M3, however, the laser was very faint at that long distance from the cryostat. Therefore, a different method was needed to align the warm optics with the telescope.

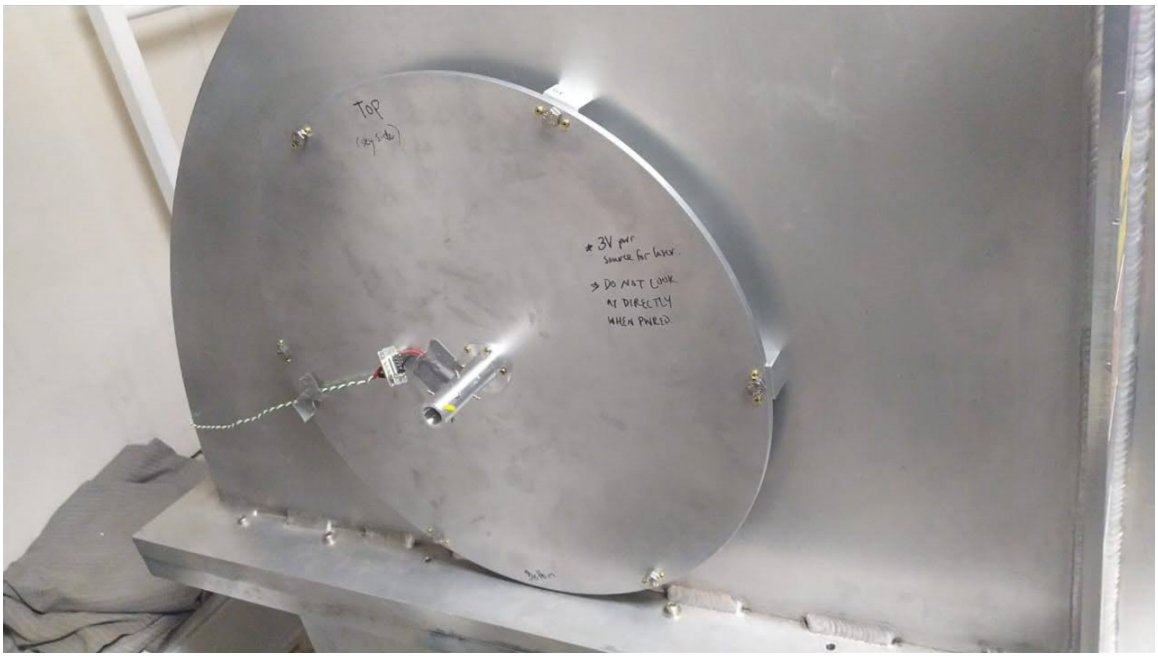

Figure 36. Laser Alignment Plate (LAP) mounted on the window of the cryostat (Lunde et al. 2022).

3.5 Liquid Nitrogen Beam Maps

To determine where the center of the beam is located, I used a set of liquid nitrogen tests. Figure 37 shows the wooden wand with black foam that was dipped in liquid nitrogen. This acts as a black body with a temperature of 77 K. When the wand was placed in front of the cryostat window, the temperature change from room temperature ($\tilde{3}$00 K) to 77 K produces a signal for the detectors to see. Figure 37 also shows the two strings tied to the tabs of M4 that mark the physical center of the mirror. By running the wand across the M4 surface while monitoring a live timestream of the central detector, I marked the approximate center of the mirror.

The timestreams show a vertical cross-section of the beam. All timestreams show data from detector 375, which was a detector near the center of the array. To more accurately measure this cross-section, the timestamps were added to the timestream.

Figure 37. Liquid Nitrogen test set up. Top left shows the tape used to mark the center of the M3 bearing. Top right shows the string used to mark the center of M4. Bottom shows the black body wand used.

The person with the wand quickly swiped the wand down through the center of the mirror to mark the start time and a second person started a timer. The first person then slowly moved the wand back up the center of the mirror calling out when the wand crossed marked positions on the mirror. The second person noted the time of each call. Figure 38 shows the resulting timestreams for two tests at M4. The red line shows the position of the starting swipe. The black line marks the center of the beam that I had approximated before. The blue line marks the string center of the mirror. No adjustments to the mirror positions were made between these two tests. These results show the repeatability of this method since the dot is approximately in the center of each of the two beams.

The next set of timestreams was done at the aperture of the bearing that holds M3. The center of the bearing was measured using tape stretched across the center shown in Figure 37. Three equally-spaced dots were marked on the piece of tape that ran vertically through the center of the bearing. These marks were referred to as "top," "center," and "bottom" to differentiate their timestamps. Following the same measurement procedure as M4, Figure 39 shows the results. The first plot shows the first measurement. The center of the beam does not line up with the center of the bearing. With two points now, a line could be drawn between the beam centers at M4 and the M3 bearing. The goal was for the beam to pass through the center of the the bearing while being parallel to the floor. Adjusting the flat M5 mirror, changes both the location and angle of the beam hitting M4. M5 was adjusted to center the beam on the bearing center. The second plot in Figure 39 shows the beam cross-section after the mirror was adjusted. The center of the beam now lines up with the center of the M3 bearing.

The final set of timestreams was done at the surface of the tertiary mirror. Figure

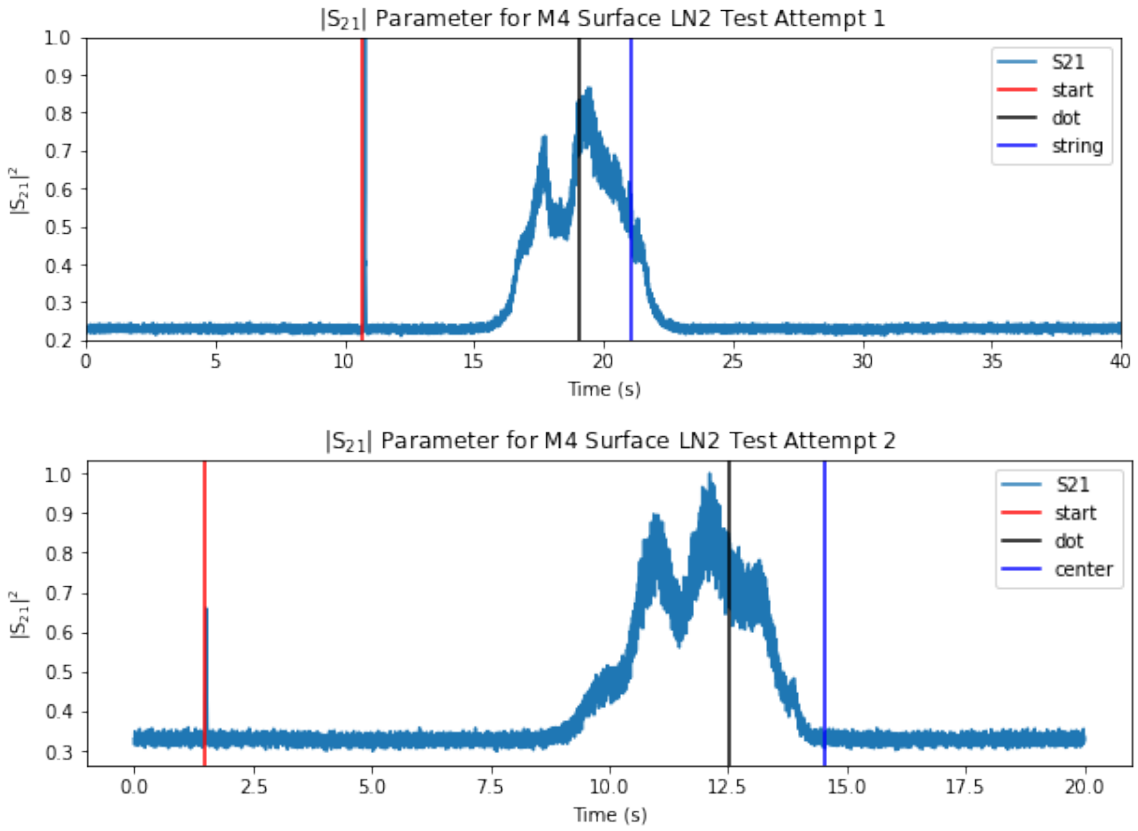

Figure 38. Liquid nitrogen test measurements just in front of the M4 surface. No changes between tests.

40 shows the results. The first plot shows the beam slice following the same procedure as before with a new wand. The new aluminum wand was longer to make it easier to reach the mirror. It also had a smaller piece of foam on the end to hopefully allow smaller features of the beam to be measured. This result has a symmetrical beam with a central peak centered on M3. However, the signal to noise was significantly worse. Since aluminum is a metal, the rod was also emitting the 77K signal causing this increase in noise. The second plot shows the result after switching back to the original wand. The noise is reduced and the beam is still centered on M3.

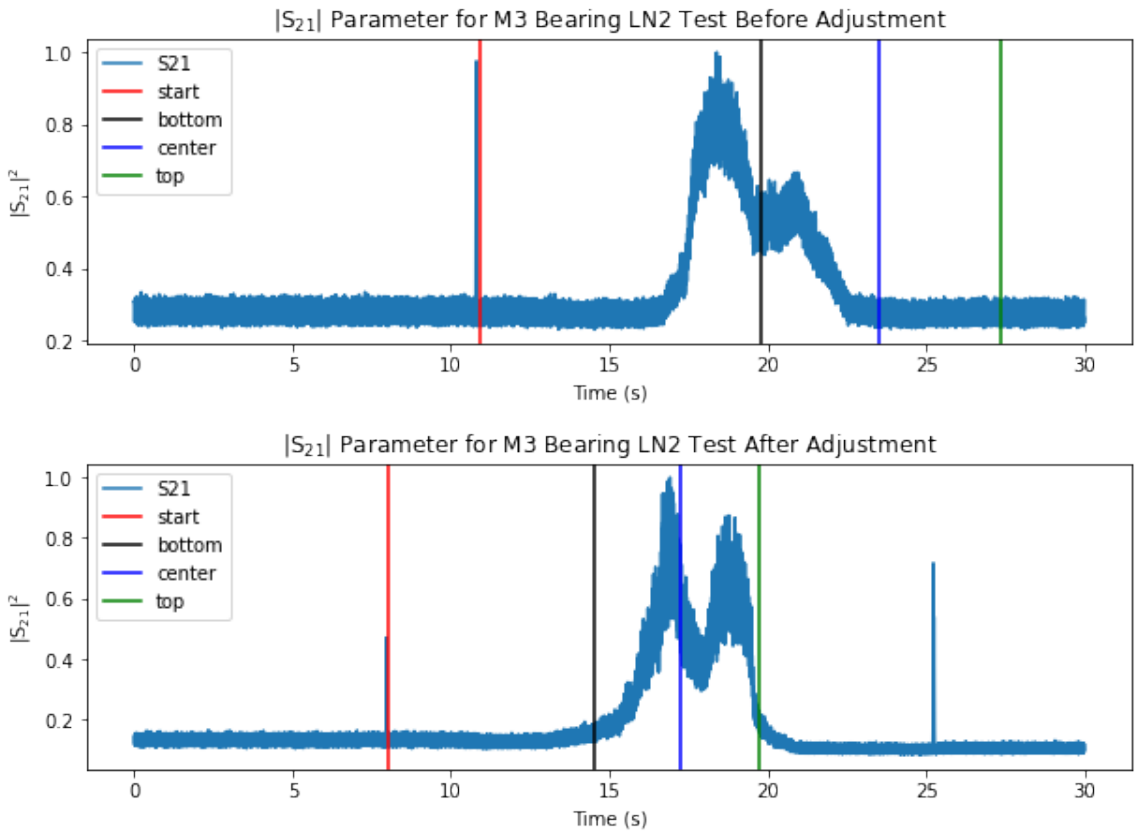

Figure 39. Liquid nitrogen test measurements at the M3 bearing. Top shows before M4 was adjusted. Bottom shows after M4 was adjusted.

3.6 Wyatt Beam Maps

After the optics were aligned, they were characterized by mapping the beam at two locations along the optical axis. The beam mapping observations were collected by measuring the detector response of a pulsable Hawkeye Technologies IR-75 source operating at 973.15 K. While the source brightness in the TolTEC frequency bands is not known, these maps show the size and shape of the beam which can then be compared to the optical model to diagnose any defects or misalignment. The IR-75 source brightness was modulated at a frequency of 10 Hz to make the source

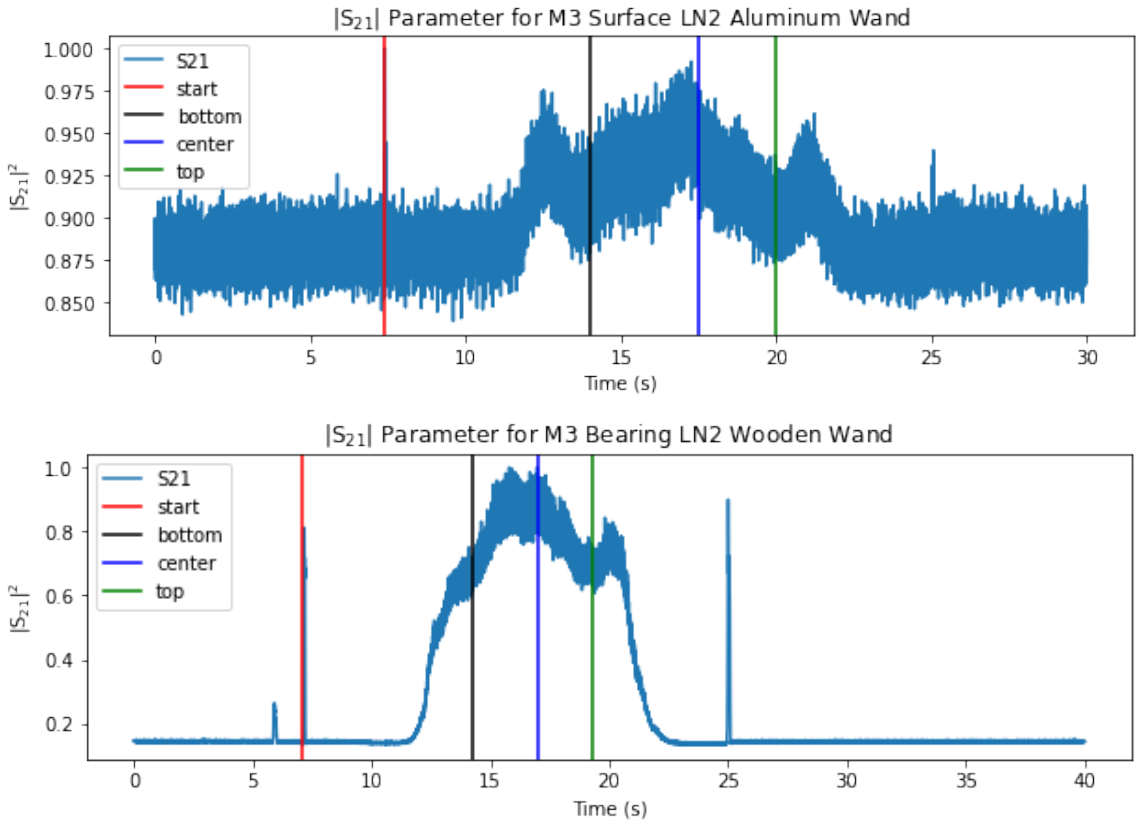

Figure 40. Liquid nitrogen test measurements just at the M3 surface. Top shows first measurement with small wand. Bottom shows the same measurement with the larger wand.

more easily observed relative to the background, by calculating the power spectral distribution (PSD) in a window around the pulsing frequency.

The source is held and moved by a computer-guided robot arm system, referred to as Wyatt, with a relative positional accuracy of 2 mm. The limbs of the robot arm are constructed from 12.5 mm diameter carbon fiber rods, with both the shoulder and elbow joints being driven by a NEMA 23 servo motor. The former is direct driven and counter-weighted, while the latter is driven with a toothed belt with a 1:1 ratio. As a result, this system can be programmed to move the source in a user-defined pattern, such as a grid of points, in the plane perpendicular to the cryostat window within a

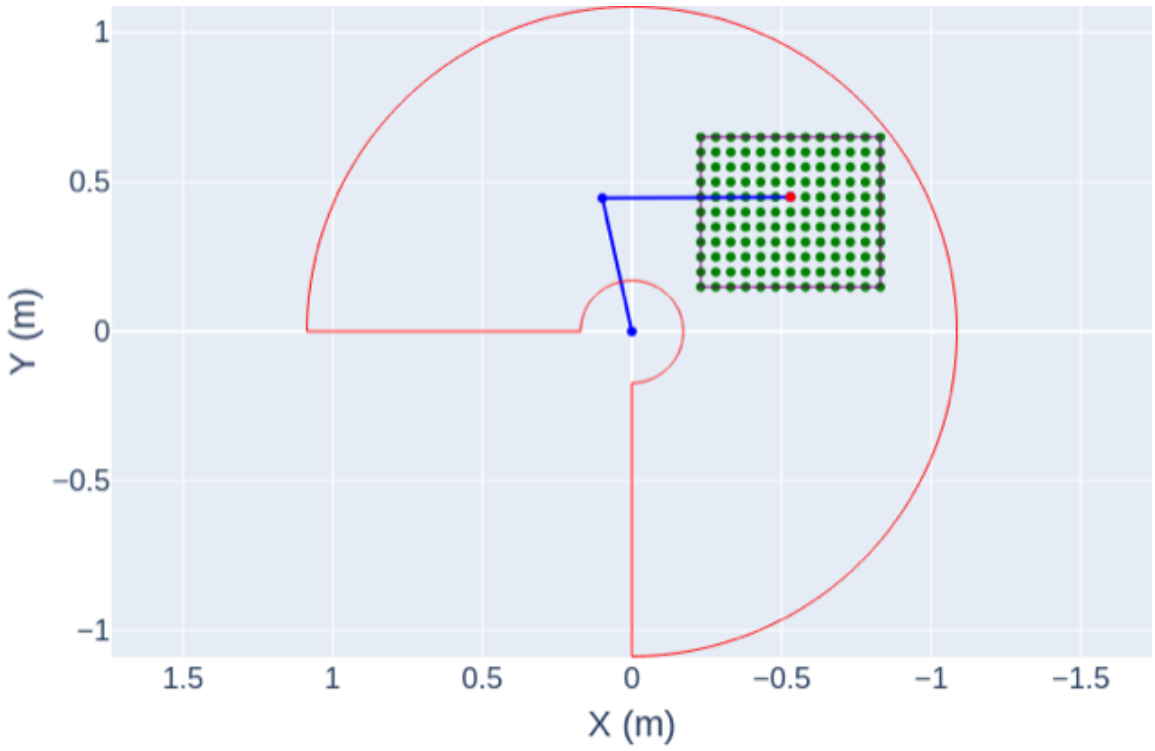

Figure 41. Example of the Wyatt robot grid configuration (green points), alongside the two robot arm limbs (blue lines), and the outline of the on the plane that the arm can reach (red line) (Lunde et al. 2020).

circular diameter of slightly more than 2 meters (Lunde et al. 2020). This region and an example grid of points are illustrated in Figure 41. For these maps, the Wyatt arm was originally set to hold the source at the height of the beam center shown in Figure 42.

Due to altitude brain fog, I forgot to measure the exact distance at which Wyatt was positioned from M4 along the optical axis. The first Wyatt map was located around 600 mm in front of the M4 surface as it was mounted on the M4 mount structure at a distance where the arm would not hit the top of M4. The Wyatt robot moved the source in a square pattern around the center of the beam with each step being 10 mm of movement. The second Wyatt map was located around 900 mm in front of the Cassegrain focus as it was mounted on between TolTEC's Cassegrain

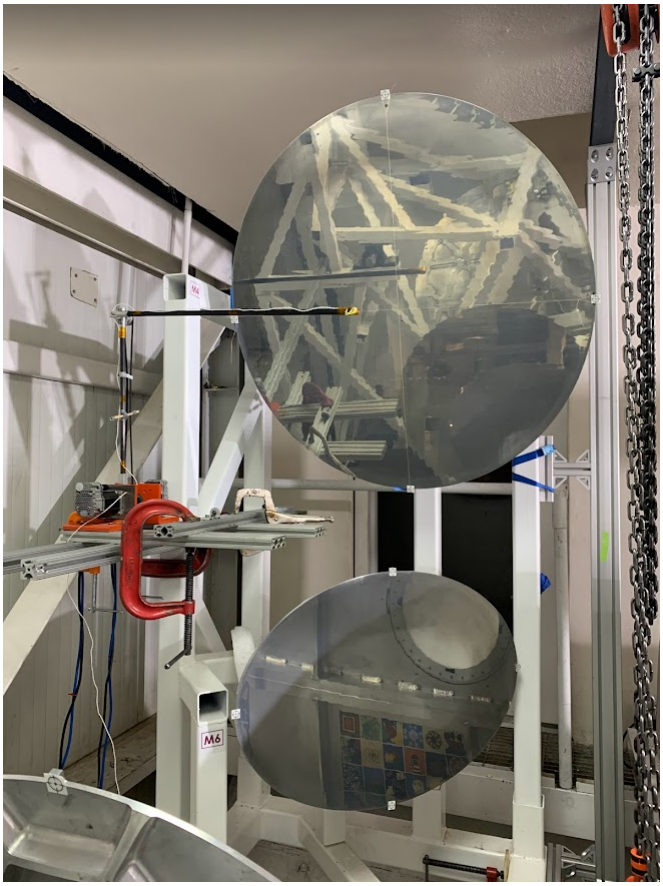

Figure 42. Wyatt robot arm mounted in front of M4. The source on the end of arm is approximately lined up with the center of the mirror.

focus and the M3 bearing. For this map where the beam is smaller, the Wyatt robot moved the source in a square pattern with each step being 5 mm of movement. Figure 43 shows the approximate positions of the planes for the two Wyatt beam maps.

To reduce the noise and make any beam features more noticeable, I stacked multiple detector's maps together which is what TolTEC can do with actual measurements. However, since the measurements were taken in close range to the detectors, not all of the detectors were able to see the Wyatt source. Since detector 375 was determined to be a detector close to the center of the array, I started my search with nearby detectors. The first selection was done based on the timestream results for the liquid

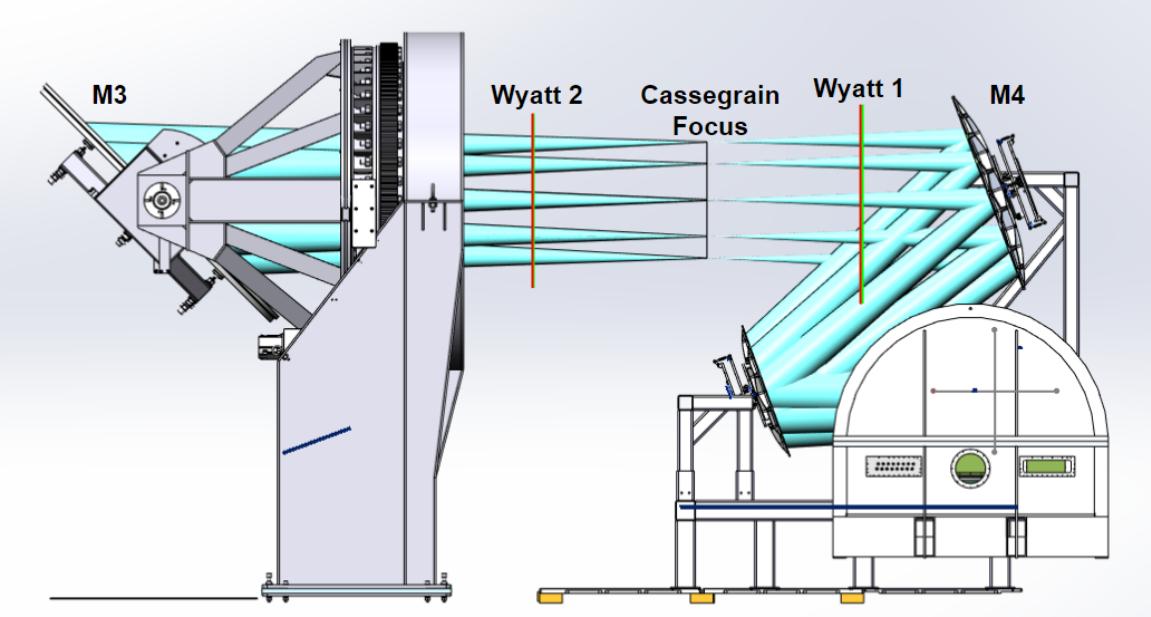

Figure 43. Approximate positions of the Wyatt robot plane for the beam maps.

nitrogen tests. Figure 44 shows a sample of the I's and Q's for 10 detectors. The red, dashed line shows detectors that I did not select since they did not see the signal. I repeated this process looking at 10 timestreams at a time for 100 of the $\tilde{4}000$ detectors of the 1.1 mm array.

I looked at the Wyatt beam map for the selected detectors and made more cuts depending on what the beam map looked like. Figure 45 shows examples of detectors that I rejected. Detectors were rejected if there was no signal, if they were too noisy, if most of the beam was cut off, and if they had double beams as shown in the examples. These detectors are ones that are not in the center of the detector array and therefore they did not accurately measure the beam. For each of the beam maps I made, I used 6 central detectors. Figures 46 and 47 show the beam maps of the detectors I selected for stacking.

To get a stacked beam, I located the center of the each individual beam. I selected the pixel near the center of the beam (marked with the red line) and lined up all

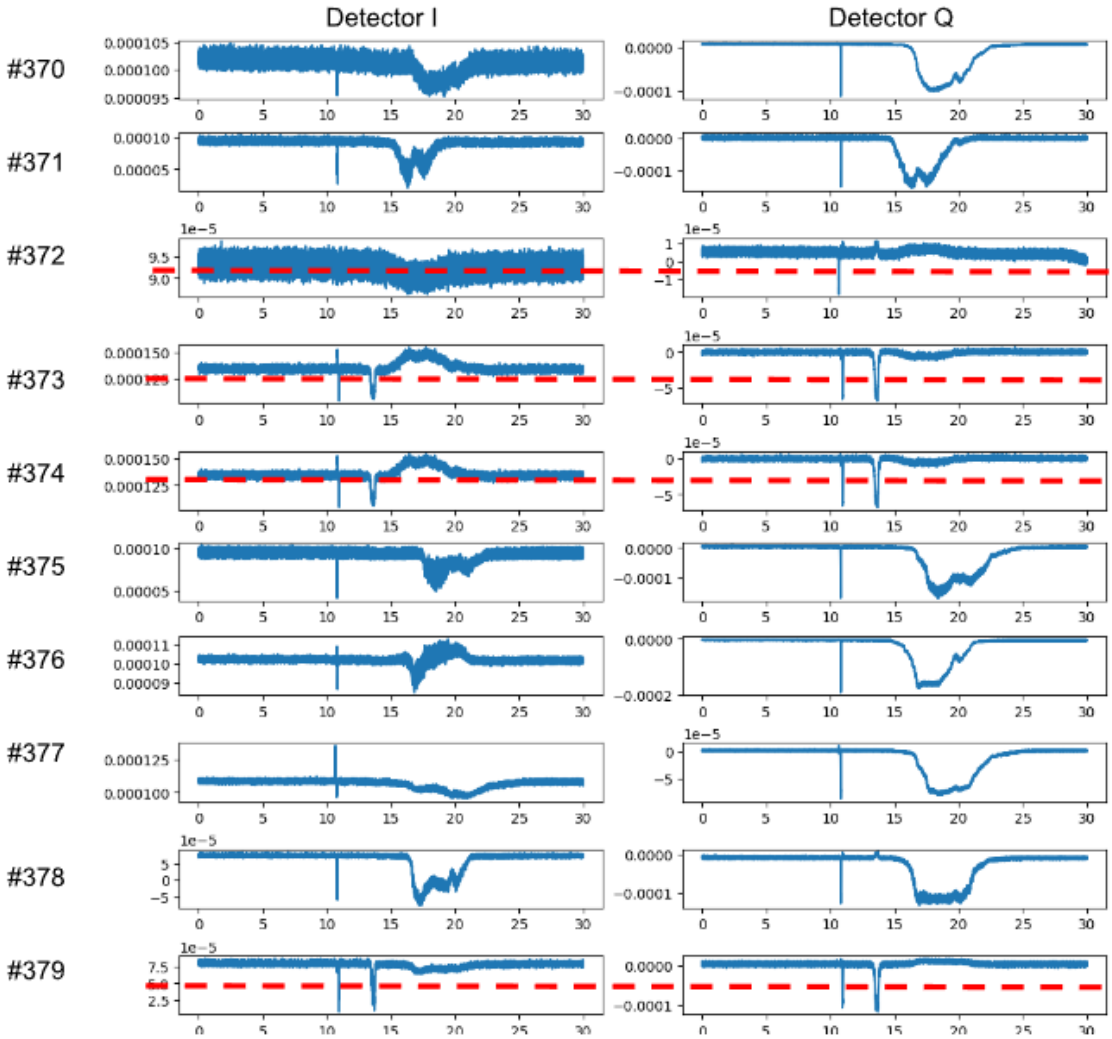

Figure 44. A selection of 10 detector's Is and Qs from the LN2 timestreams. Red dashed line shows detectors I did not select based on timestreams.

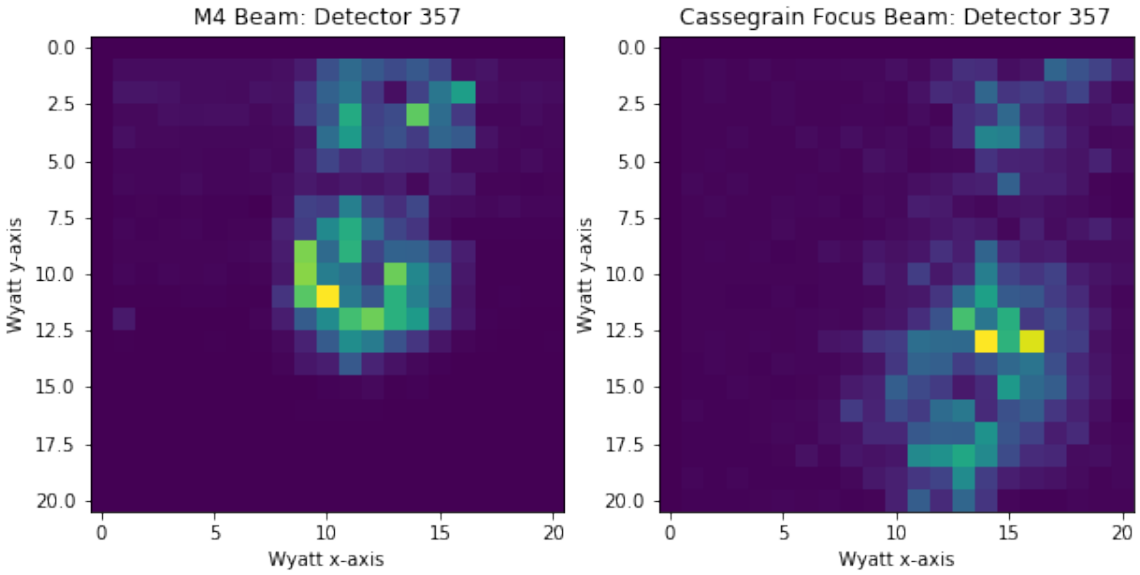

Figure 45. Examples of detectors I rejected because of abnormal shapes.

six beams. Then I averaged the pixels together. None of the beams were directly in the center of their beam map. Therefore, each pixel in the final map was created using a different number of detector pixels. For example, the central part of the beam overlaps, so in the stacked image six pixels were averaged to get the pixel in the final image. However, around the edge of the stacked beam, 2-3 detector pixels were averaged. Figure 48 shows the resulting beams. These results can be compared to the Zemax beams shown previously in Figure 33. The beam map near M4 has a diameter of about 50 mm and a annular shape. This appears to match the shape and size of the Zemax beam. The beam map near the Cassegrain focus has a diameter of about 40 mm and also has a annular shape. This appears to match the shape and size of the Zemax beam near the Cassegrain focus.

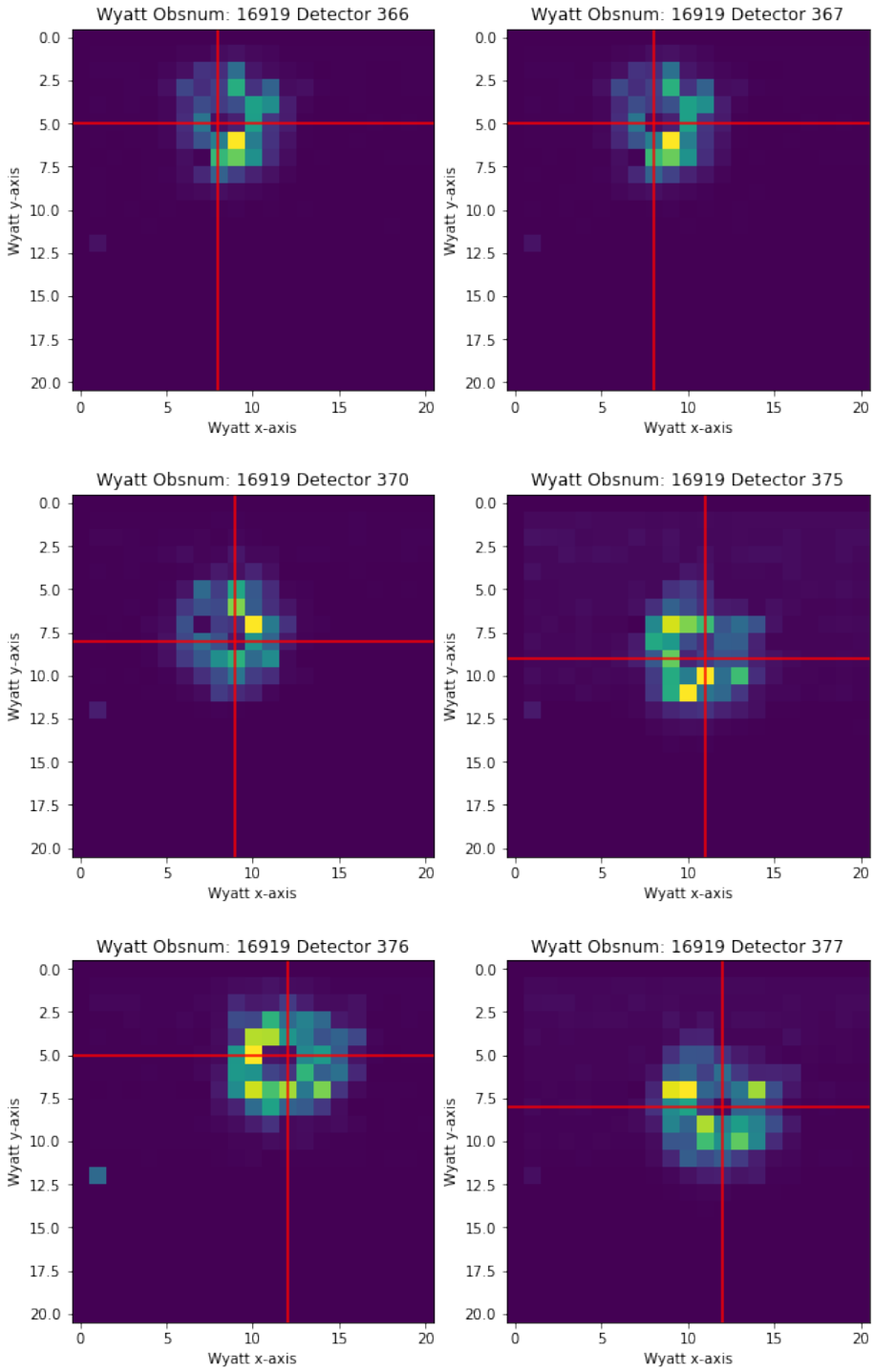

Figure 46. These are the detectors selected and used for the Wyatt beam map near the M4 surface. Red lines mark the pixel used to line up the images.

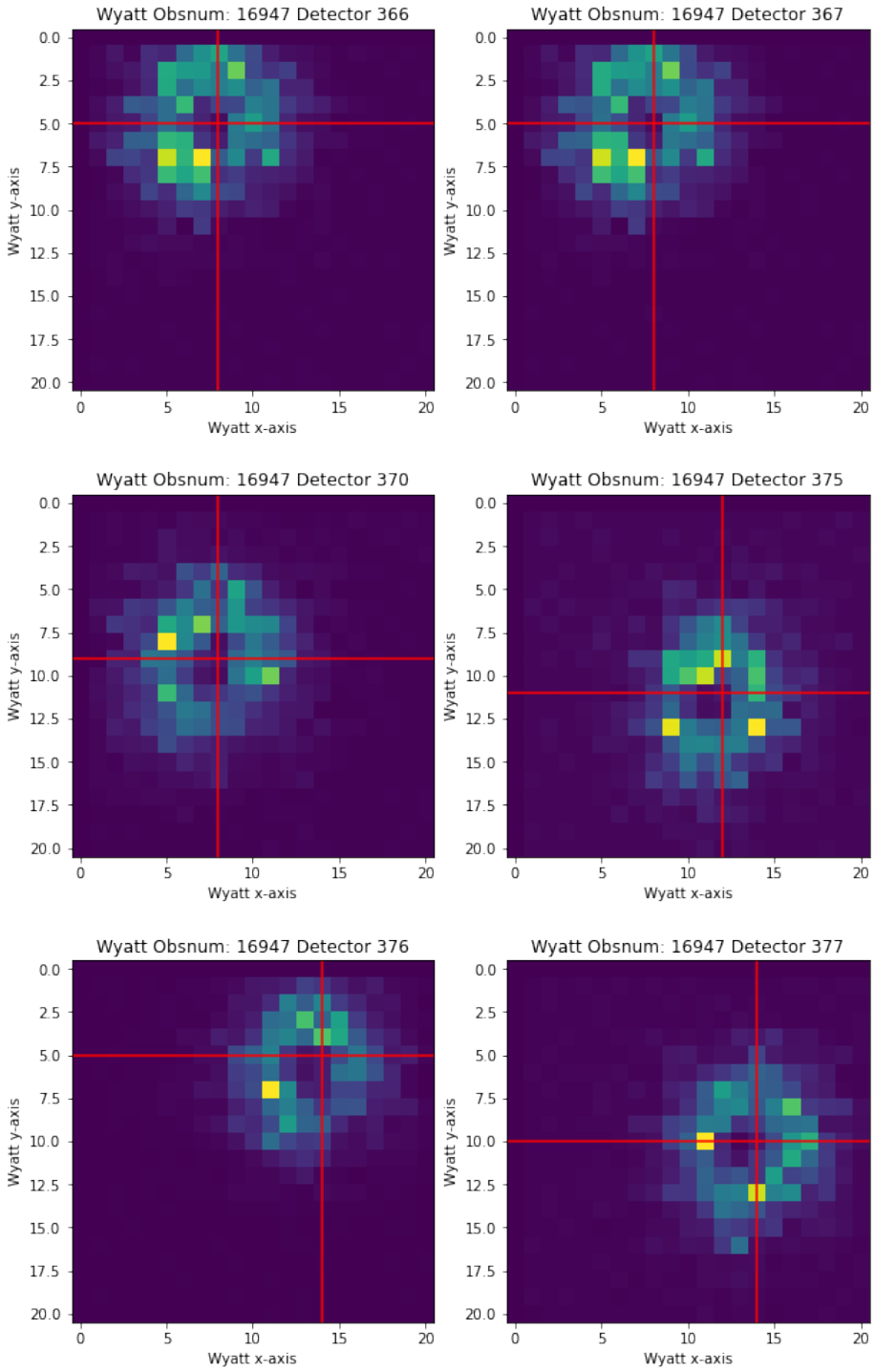

Figure 47. These are the detectors selected and used for the Wyatt beam map near the Cassegrain focus. Red lines mark the pixel used to line up the images.

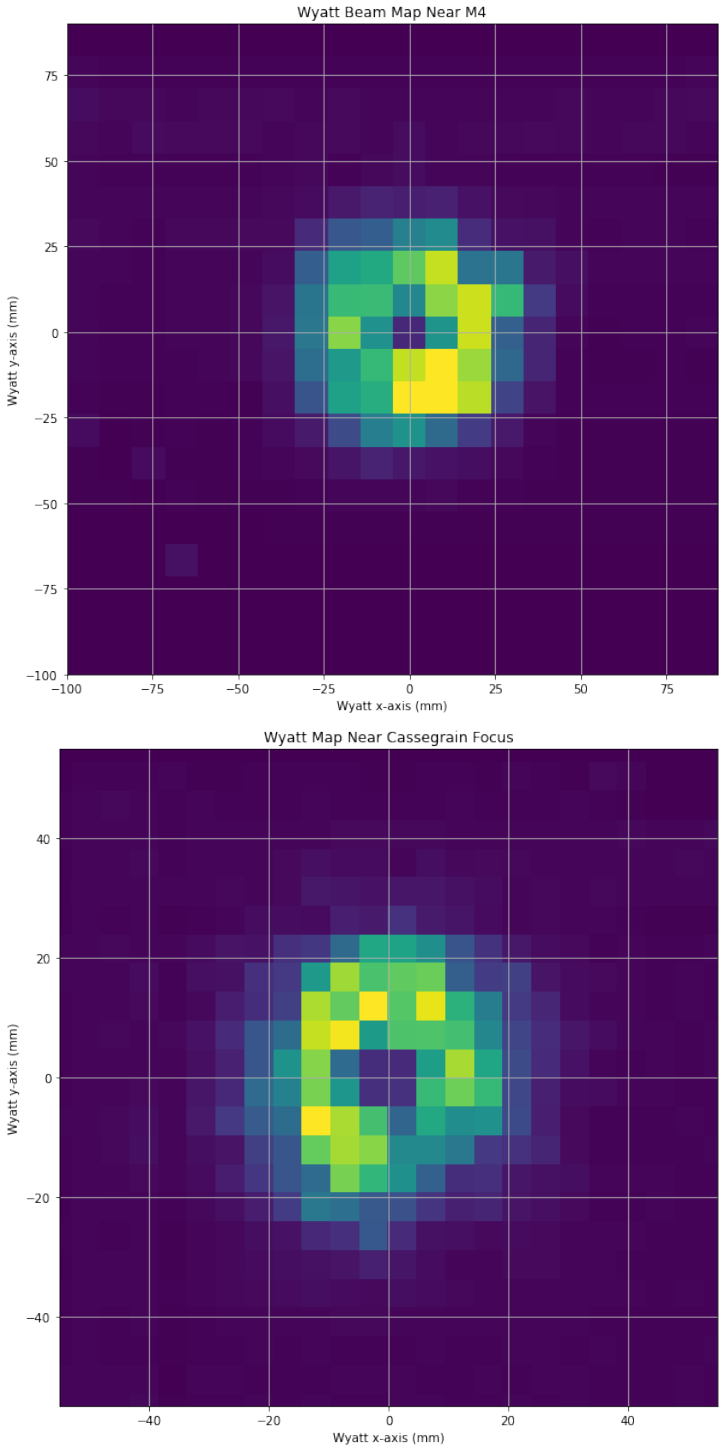

Figure 48. Wyatt beam maps at two different locations along the optical axis: near M4 (top) and near the Cassegrain focus (bottom).

3.7 Radial Profiles

Radial profiles offer a quantitative way of comparing the Wyatt beam map results with the Zemax models. I used the python photometry package, Photutils (Bradley et al. 2023). The procedure was completed for both the Zemax and Wyatt beams. First, I determined the coordinates of the beam centers. Then, I created circular ring apertures centered on the central point with a specified thickness. For the Zemax beams, I used a thickness of 2 pixels. For the Wyatt beams, I used a thickness of one pixel since these images have fewer pixels available. The mean and standard deviation were calculated for each annular aperture. Since the Wyatt IR source has an unknown brightness at TolTEC wavelengths, the radial profiles were normalized by dividing the values by the maximum radial intensity. The error bars for the Zemax beams are the standard deviations from the aperture measurements. The error bars for the Wyatt beams are the standard deviations from the aperture measurements plus an additional error from noise in the beam maps. This noise was measured by calculating the standard deviation of sections of the stacked Wyatt map that do not contain the beam. These were calculated using a weighted average method, since each pixel was stacked using a different number of images.

Figure 49 shows the radial profile results for the beams at a surface a distance of 640 mm in front of the M4 surface. The Wyatt beam and Zemax beam have the same annular shape. There is a low spot in the center of the beam. Both beams peak around 15 mm and then fall off to zero at the similar rates. This shows that the beam diameters of the both the Zemax model and the TolTEC result are the same size. The size and shape of the Wyatt beam match the predicted beam from the Zemax model.

Figure 50 shows the radial profile results for the beams at a surface a distance

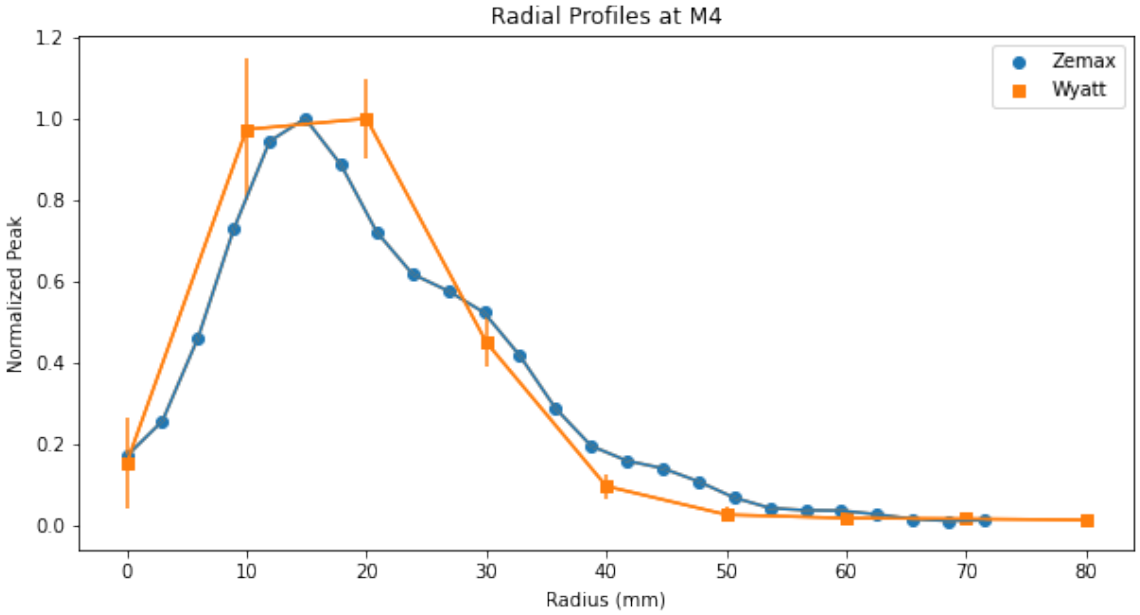

Figure 49. Radial profiles of the Zemax beam and the Wyatt beam near the M4 surface.

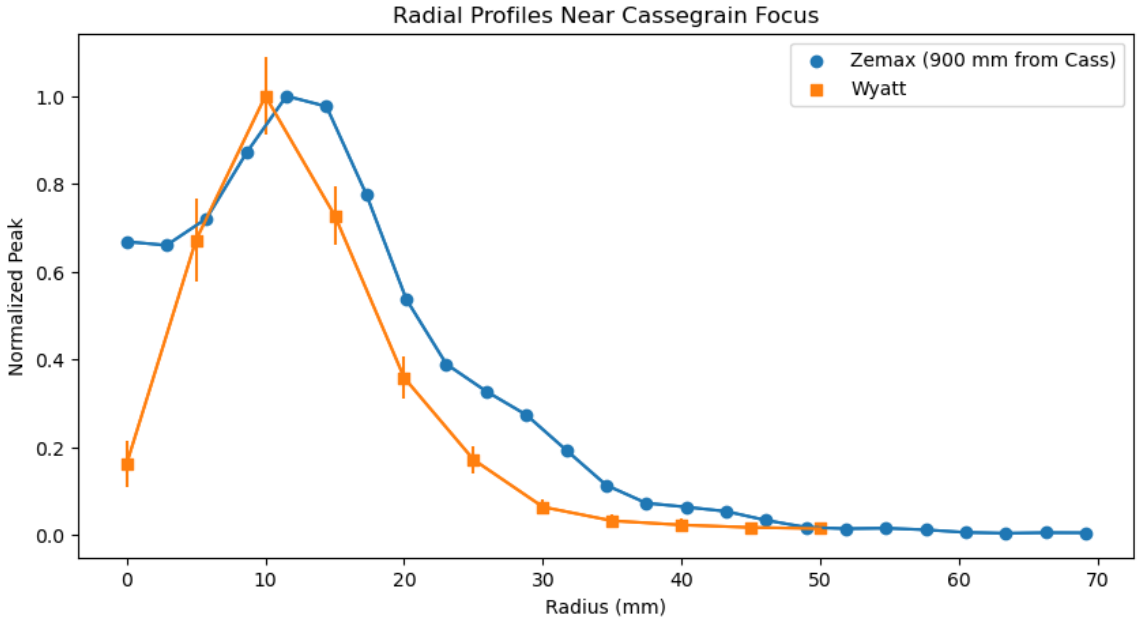

Figure 50. Radial profiles of the Zemax beam and the Wyatt beam near the Cassegrain focus.

of about 900 mm in front of the Cassegrain focus. The Zemax model and TolTEC results again fall off at a similar rate showing the beams to be close to the same size. However, where the Wyatt beam drops to nearly zero in the center, the Zemax model only has a slight dip in intensity. This difference is most likely caused by a phase difference between the model and reality. Also, I did not measure the exact distance between M4 and where the Wyatt robot was set up. Using different distances between the model surface and Wyatt positions could result in a phase change.

Figure 51 shows the radial profile result of the Zemax beam at the M3 surface and the liquid nitrogen timestream collected using the small aluminum wand for higher resolution. Since the liquid nitrogen timestream had a lot of noise, I filtered the data with a low pass filter to reduce the amplitude of the noise. The timestream does not allow me to measure the diameter of the beam. However, the shape of the Wyatt beam at the M3 surface is similar to the Zemax model. There is a peak at the center and two smaller peaks that show a multiple rings in the beam.

3.8 On-Sky Alignment

The LMT provides methods of adjusting the focus, correcting for astigmatism, and removing beam offsets. For these measurements, TolTEC looked at BL Lac, which is a radio-bright active galactic nucleus that was visible from the LMT site. The first beam maps of BL Lac showed an extended, elliptical image. The focus was corrected by adjusting the position of the secondary mirror along the optical axis. The optimal position was found by taking measurements of BL Lac with different offsets of M2. Figure 52 shows a plot of fitted flux vs M2 offset with the beam maps of each measurement to show how the shape of the beam changes with the focus. 7

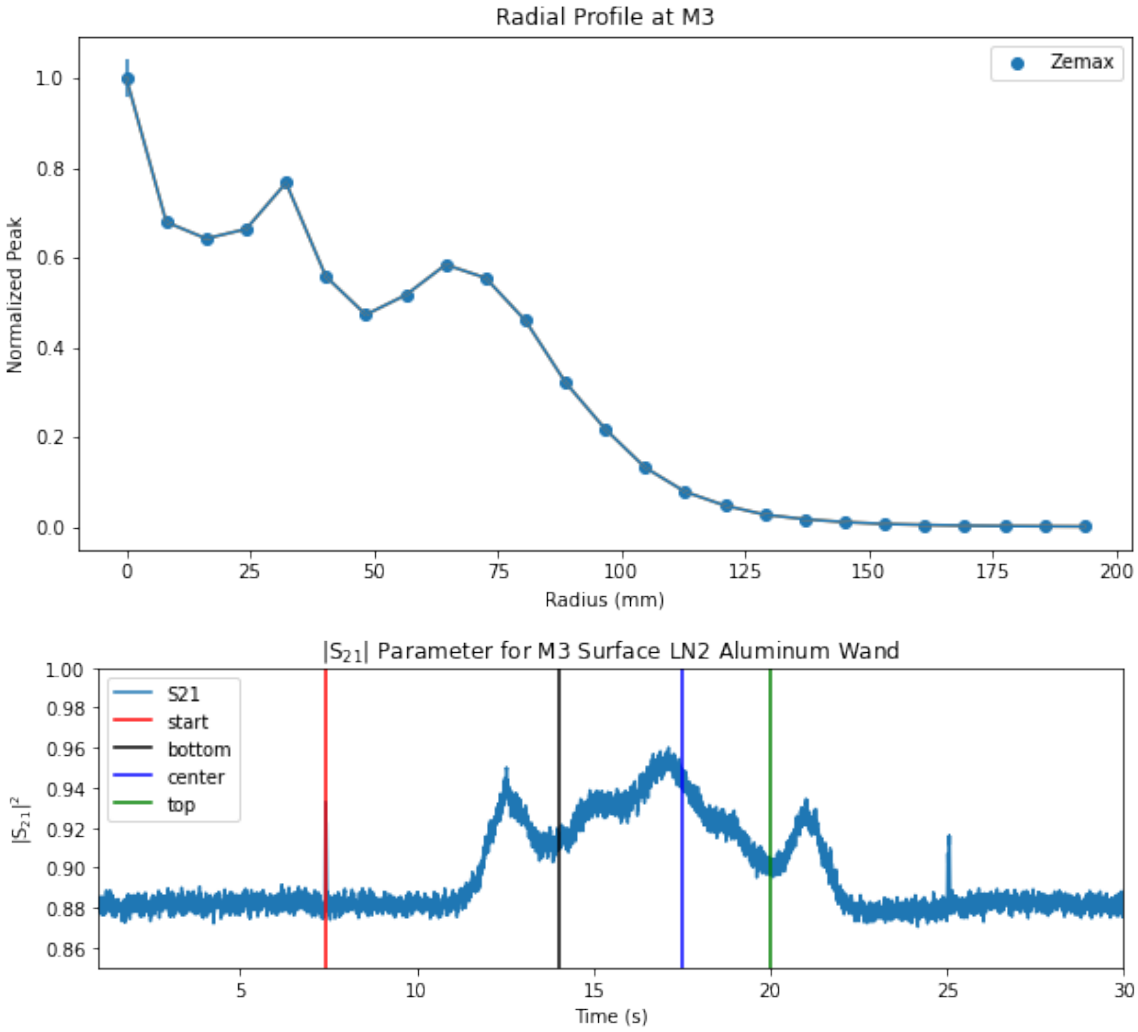

Figure 51. Radial profile of the Zemax beam at the M3 surface (top). Filtered timestream of beam at the surface of M3 for shape comparison (bottom)

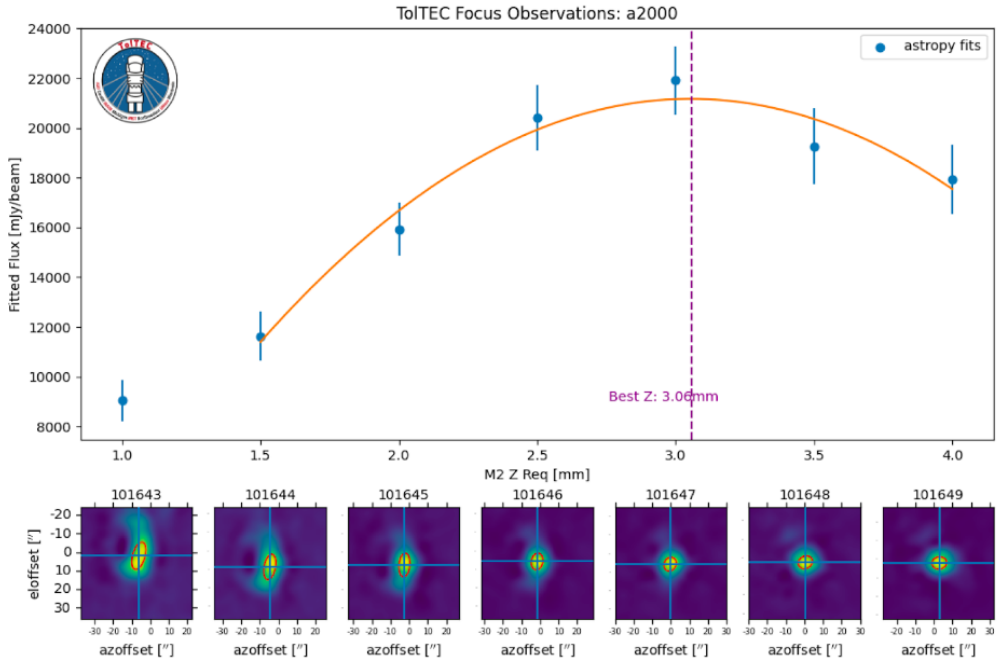

Figure 52. Focus observations on BL Lac. Plot from Grant Wilson (Lunde et al. 2022).

beam maps were collected starting with an offset of 1 mm and increasing in steps of 0.5 mm. The optimal offset along the optical axis was 3.06 mm.

A similar method was used to determine the optimal astigmatism correction. Since the LMT primary mirror has an active surface, the shape of the primary mirror can be adjusted for astigmatism corrections. Optical aberrations, like astigmatism, can be modeled using Zernike polynomials. All of the Zernike patterns are pre-programmed into the primary mirror. By using the approximately 750 actuators on the primary mirror segments, the shape of the primary is changed to correct these errors. The Figure 53 shows a plot of fitted flux vs Zernike polynomial coefficients. The beam maps of each measurement show how the shape of the beam changes with astigmatism corrections. 5 beam maps were collected starting with a coefficient of -200 mm

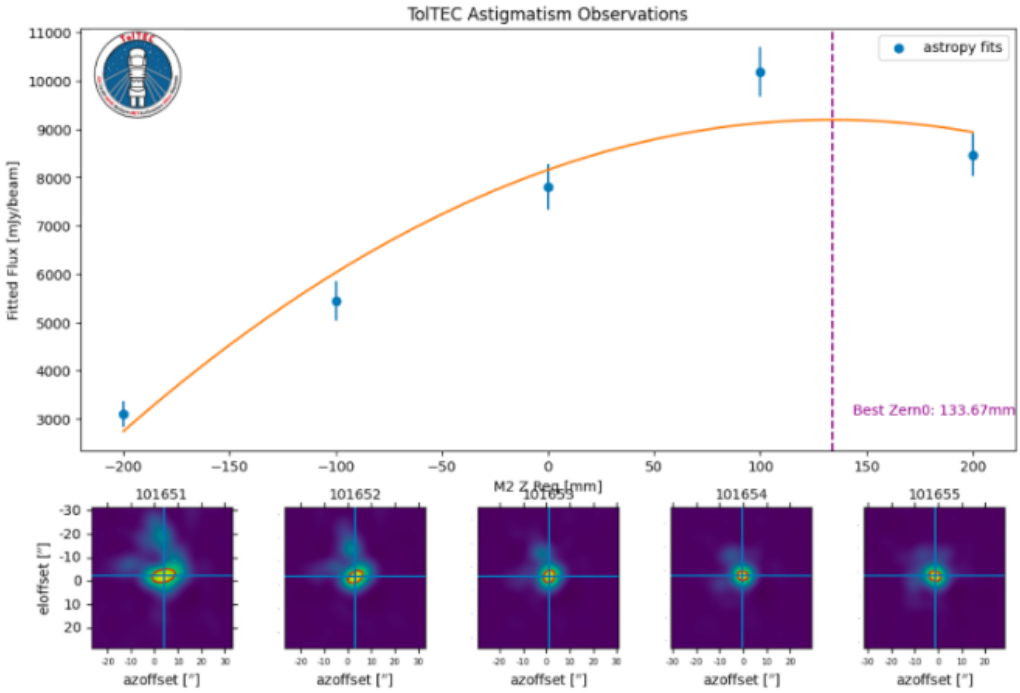

Figure 53. Astigmatism observations on BL Lac. Plot from Grant Wilson (Lunde et al. 2022).

increasing to 200 mm with steps of 100 mm. The optimal zeroth order coefficient for the Zernike polynomial is 133.67 mm.

3.9 Preliminary Commissioning Results

Commissioning is an on-going task for TolTEC that began in June 2022, continued in December 2022 after the cryostat was opened for repairs, and currently waiting for power to be returned to the LMT site. Figure 54 shows results from TolTEC commissioning done during the winter. The top row of plots show the positions of working detectors in the arrays, from left to right: the 1.1 mm array, the 1.4 mm array, and the 2.0 mm array. The detectors are colored to represent the different electronic readout chains. The three detector arrays contain different numbers of detectors: 4000

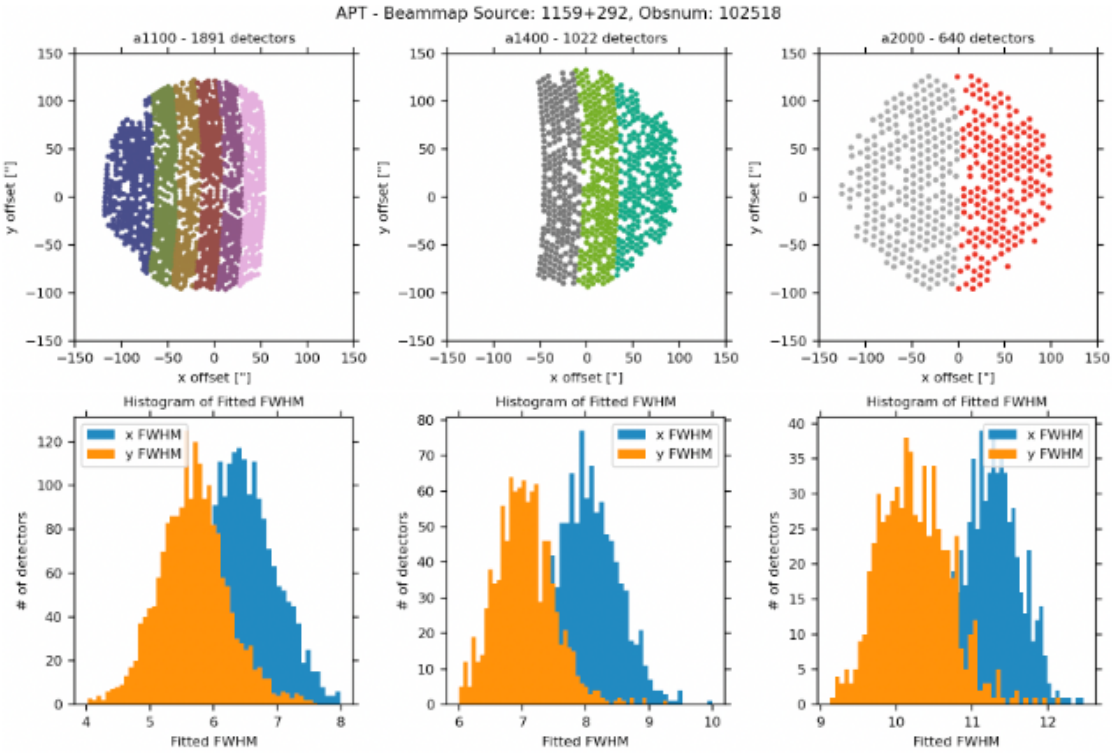

Figure 54. TolTEC beams from on-sky commissioning. Columns of plots from left to right show the 1.1 mm, 1.4 mm, and 2.0 mm detector arrays. Plot from Grant Wilson.

detectors for the 1.1 mm array, 2500 for the 1.4 mm array, and 1200 for the 2.0 mm array. However, not every detector was working during this measurement. There is a missing section of detectors in the 1.1 mm array and another in the 1.4 mm array because two of the readout chains are not working properly. Sometimes detectors get missed because of noise. For this measurement, 47% of the detectors were working in the 1.1 mm array, 41% in the 1.4 mm array, and 53% in the 2.0 mm array. These detector yields will be improved during future commissioning runs. I will also note that since each TolTEC pixel has two detectors to look at polarization, having only half the detectors show up for each of the arrays could have something to do with polarization either in the map-making code or the light.

The bottom row histograms show the full-width-half-maximum (FWHM) of beams

Table 9. Angular Resolution of the TolTEC Optics

λ	x-FWHM	y-FWHM	Average	D_{50}	D_{47}
1.1 mm	6.375 ± 0.012"	5.75 ± 0.010"	6.06 ± 0.011"	5.5"	5.9"
1.4 mm	8.0 ± 0.013"	7.0 ± 0.013"	7.50 ± 0.013"	7.0"	7.5"
2.0 mm	11.375 ± 0.021"	10.125 ± 0.021"	10.75 ± 0.021"	10.1"	10.7"

Note: This table compares the measured FWHM of the beam to the Rayleigh criterion resolution calculated for a 50 m primary aperture and a 47 m primary aperture.

fitted to each detector beam in the x and y directions. This shows the size in arcseconds of the beams on the sky while observing. Table 9 lists the mean values of the beam FWHM and compares them to the angular resolution calculated using the Rayleigh criterion shown in equation 3.7 (Rayleigh 1879).

$$\theta \approx 1.22 \frac{\lambda}{D} \left(\frac{180^\circ}{\pi} \right) \left(\frac{3600"}{1^\circ} \right) \tag{3.7}$$

where λ is the wavelength and D is the diameter of the primary mirror. I calculated the angular resolution using two different diameters. The first Rayleigh calculation uses the full 50 m diameter of the LMT primary mirror. However, with the Lyot stop, the beam illuminates slightly less than the full 50 m primary mirror. The Lyot stop reduces it to a primary aperture diameter of 47 m. For all three wavelengths, the beam appears slightly elongated along the x-axis. This could be caused by error in the focus and astigmatism. I also calculated the average FWHM of the beam by taking the average of the x and y values. This gives a beam size of 6.06" for the 1.1 mm band, 7.50 for the 1.4 mm band, and 10.75" for the 2.0 mm band. These values are consistent with the Rayleigh criterion for an optical system with a aperture diameter of 47 m.

Chapter 4

CRYOGENICS AND DETECTOR TESTING

4.1 Cryostat Redesign

Baby Beluga is the millikelvin cryostat in the lab shown in Figure 55. This cryostat uses a pulse tube cryocooler to reach a temperature of 4 Kelvin. Mounted on the 4K-plate, is a Helium-3 sorption fridge. The sorption fridge uses evaporative cooling of Helium-4 to cool to 1 K combined with evaporative cooling of Helium-3 to cool to 250 mK. The Baby Beluga cryostat needed to be updated to test the prototype microwave kinetic inductance detectors (MKIDs) for TolTEC. Alternating current (AC) and direct current (DC) cabling was needed for the millikelvin stages. Heat straps between the millikelvin and cold heads were needed to improve the thermal connections. New temperature sensors were calibrated. And a new cryostat mount was designed to reduce the risk of helium leakage in the system.

4.1.1 Replacing AC and DC wiring

To reduce the thermal load on the millikelvin stage, the original solid copper wires were replaced with cryogenic cable. The cryogenic wire has a smaller cross-sectional area than solid copper wires to reduce the thermal conduction between the millikelvin stages and the 4 kelvin stage though the DC wiring. Aluminum tape was used to thoroughly heat sink the cryogenic wire to the 4 K and the 350 mK to ensure the wire reached those temperatures before moving to the 250 mK stage.

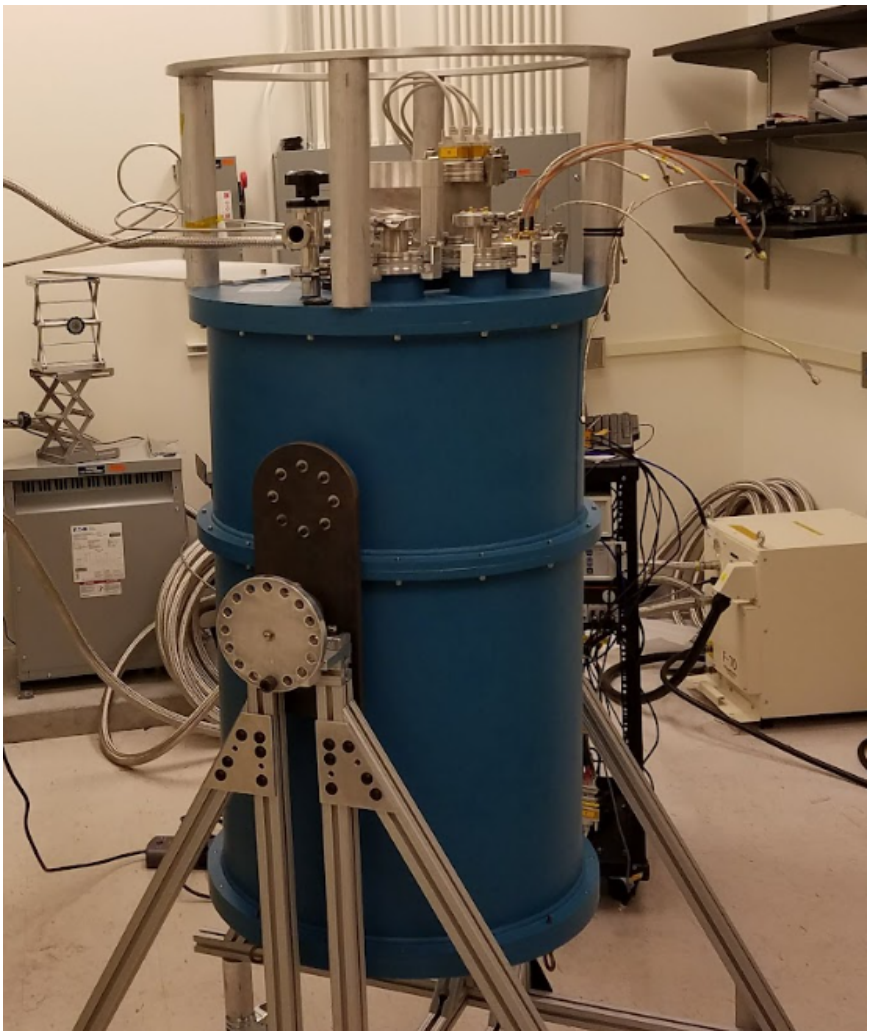

Figure 55. Baby Beluga cryostat on its original rotating cart mount.

New coaxial cables were made to readout the AC signal from the detectors on the millikelvin stages. Stainless steel cables were used between each of the different temperature stages in the cryostat. Since stainless steel has low thermal conductance, these cables reduce the thermal loading of the lower temperature stages. Figure 56 shows the coax cables between the 350 mK and 250 mK stages. Each cable was bent to contain a single loop. This loop absorbs the thermal expansion movement of the cable to prevent the rigid cable from being damaged from stresses caused by

Figure 56. Coax Cables in Baby Beluga.

movement. Copper coax cables were used provide extra flexibility for attaching the cables in the small gap between the two millikelvin stages.

4.1.2 Improving thermal connections

New copper heat straps were designed to connect the millikelvin plates to the cold heads of the helium sorption fridge. Figure 57 shows the new heat straps. These heat straps were cut from a 0.05 inch copper sheet. The width of the straps allows for contact with the entire surface area of both the ultra head and the inter head. The length gives around 2 inches of contact with the copper stages. The heat straps were bent around a 0.75 inch diameter cylindrical object and are bent to avoid possible contact with the 4 K shell. With no sharp curves, the tensile forces applied to the cold head though the strap are minimal. The straps were bolted to the cold heads and

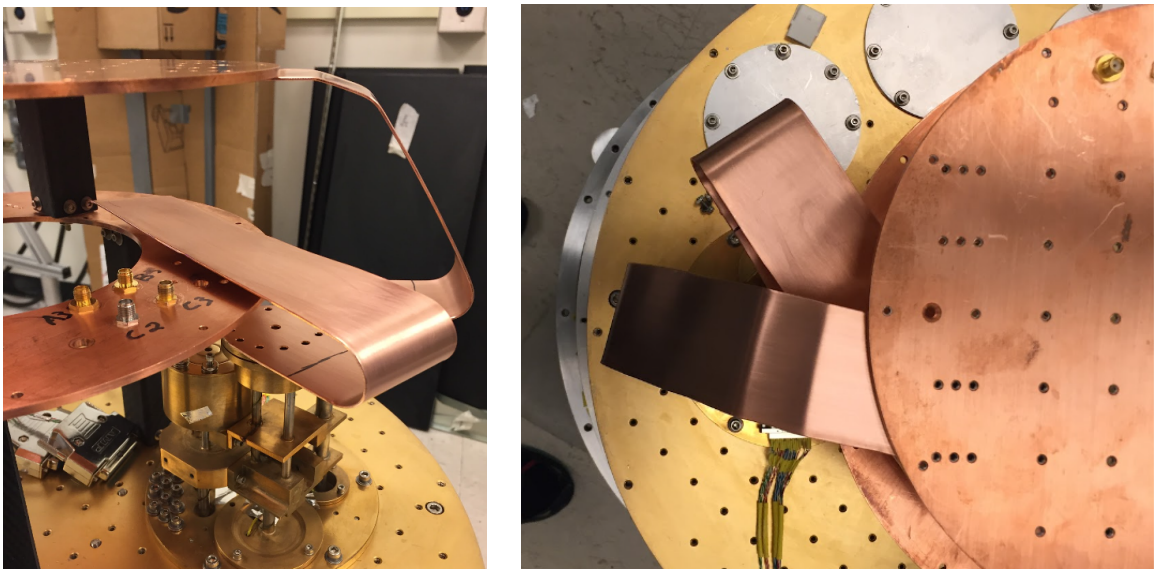

Figure 57. These images show the copper heat straps designed to connect the millikelvin plates to the cold heads.

the stages using conical spring washers designed to maintain contact through thermal expansion.

4.1.3 Calibrating temperature sensors

One of the goals with the MKID testing was to measure the thermal response of the detectors. The plan was for each detector array to have a separate temperature sensor attached directly to its packaging. To do this, I had to calibrate the two millikelvin-rated Cernox temperature sensors from room temperature (300 K) to the lowest temperature Baby Beluga can achieve. The helium sorption fridge has a built-in temperature sensor on the ultra head that is calibrated for low temperatures between 0.1-4 K. I found a third diode temperature sensor that was calibrated from 1-300 K. Figure 58 shows where I attached the three temperature sensors directly to the 250 mK ultra head. Then I closed up Baby Beluga and started a cool down.

I collected the temperature output from the ultra head and diode sensors and the resistance measurement from the two Cernox temperature sensors. I cycled the millikelvin fridge multiple times to get multiple data points. For each temperature value, I averaged the resistance outputs from the new temperature sensors. The resulting temperature curves are shown in Figure 59. The LakeShore temperature monitor stores 200 data points for each calibration file. I selected 200 temperature points between between 4-300 K and another 200 points for 250 mK-4 K to create two temperature curves. This gave the Cernox sensors a more accurate curve for sub-kelvin temperatures where detector testing occurs.

4.1.4 Designing cryostat mount

The original Baby Beluga mount was a triangular cart that allowed the cryostat to be rotated 180 degrees from its operating position to its open position where it had to be taken off of the cart and set on the ground. While its opened position allowed for easy access to the low temperature stages, the rotation required the helium lines shown in Figure 60 to be disconnected every time the cryostat was opened up. Helium lines are not designed to be repeatedly connected and disconnected for long periods of time. Over many cycles, the threads on the connections start to wear and the self-sealing mechanism begins to fail. The self-sealing mechanism keeps large amounts of helium from escaping while also preventing outside air from contaminating the system. When these couplings begin to fail, helium begins to escape during the process of connecting and disconnecting the threads. While opening up Baby Beluga after a cool down, I noticed the coupling failure signs and determined that a new mount was needed.

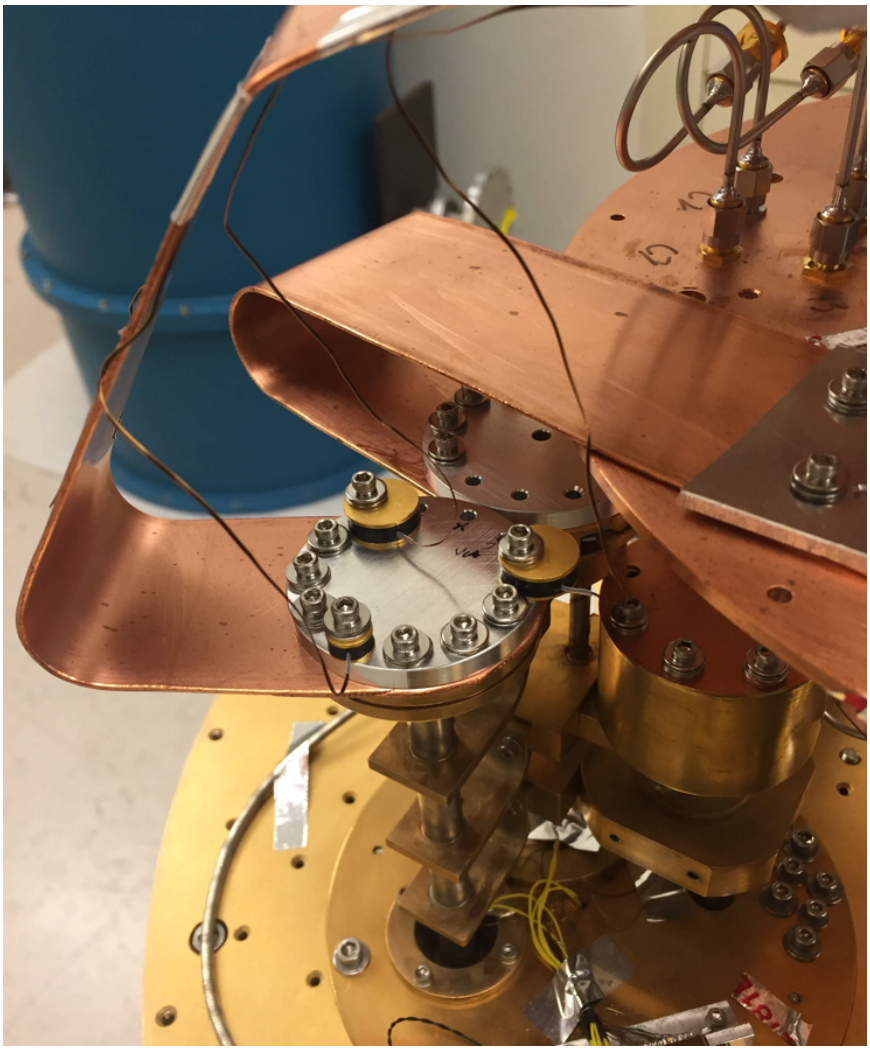

Figure 58. Temperature sensors mounted directly on the cold head for temperature calibration run.

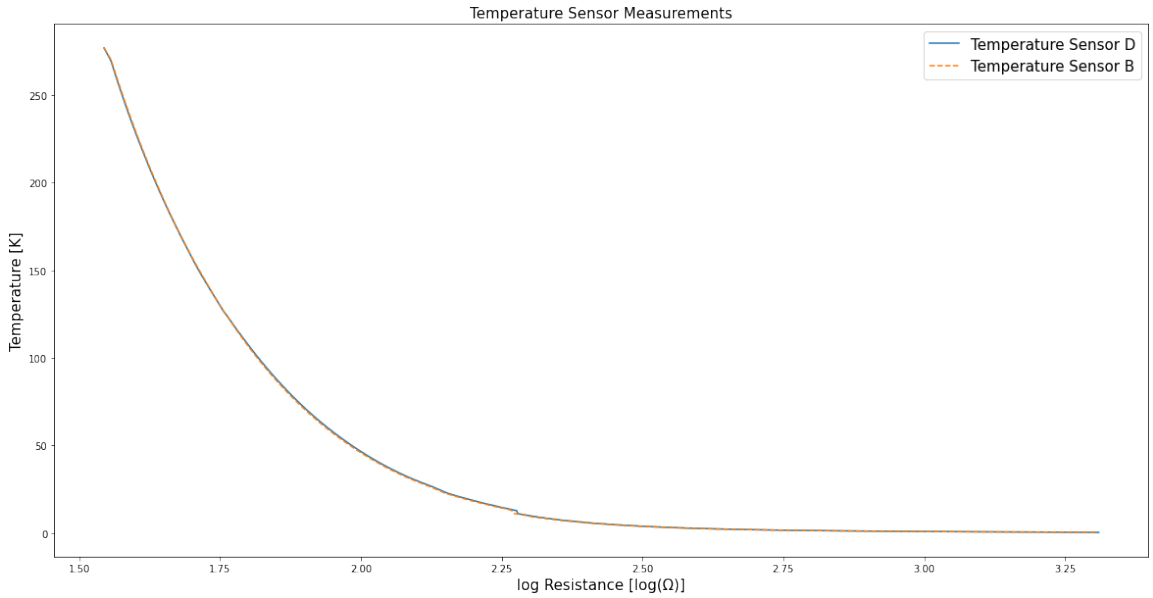

Figure 59. Temperature sensor calibration plot: temperature vs resistance.

A mount that allowed the helium lines to remain connected throughout the entire opening and closing processes.

The first step in designing was to determine the requirements the new mount must have. The weight of Baby Beluga was measured with a scale from the machine shop. The cryostat weighed 350 pounds (160 kg). This was the weight the mount must be able to support without deformations that cause strain in the helium lines. To avoid removing the helium lines, the cryostat must be held in its operating orientation at a height that allows the 300 K shell to be removed. The mount must also fit into the cryostat room and maintain a safe distance from the ceiling.

Using the solidworks model of the cryostat and the room shown in Figure 61, a structure was designed. The new mount is bolted to the wall between the sink and shelves to clear a central walkway through the room. The pump is held to the side of the mount to avoid bending the helium lines. The mount is high enough to remove the cryostat shell (shown as the transparent structure underneath the blue cryostat).

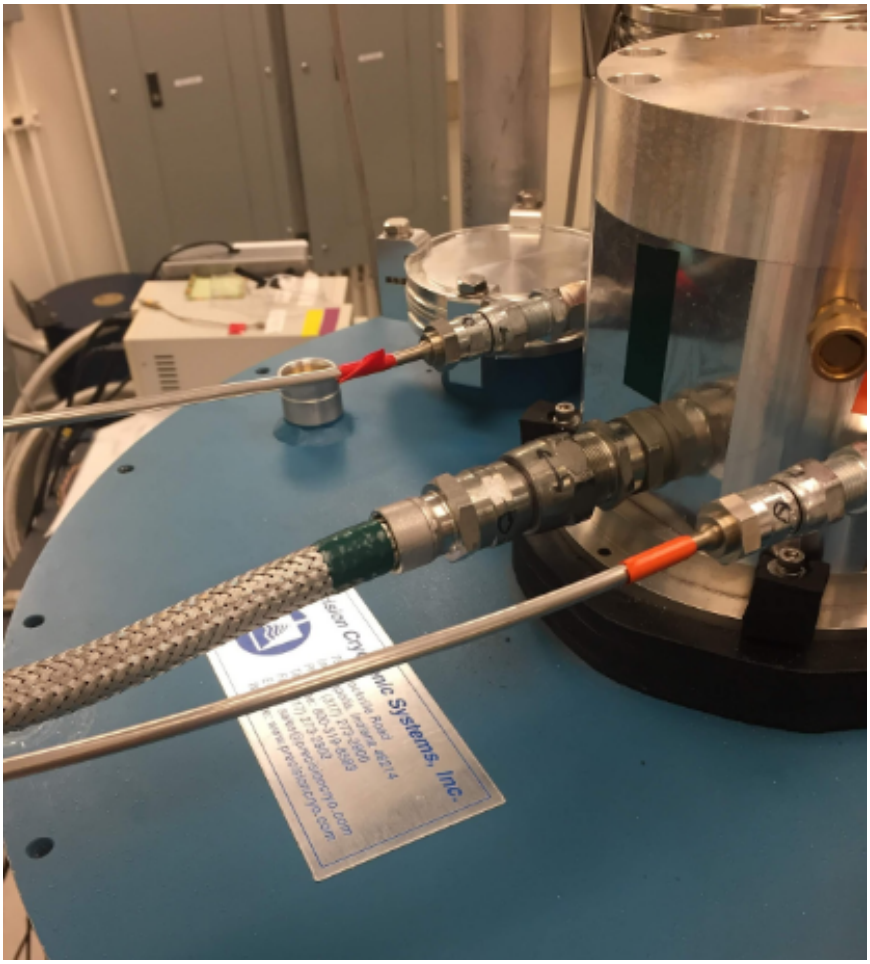

Figure 60. Helium line connections that needed to be connected and disconnected every time the cryostat was opened.

There is space between the cryostat shell and the ground for the fork lift to to raise and lower the shell.

Figure 62 shows the static and vibration analysis done for the cryostat mount design. The model was simplified by applying the cryostat weight as a remote mass to the top beams of the structure. The fixed surface of the simulation was the bottom beams where the mount touches the ground. I left out the points where the mount is bolted to the wall to see how the structure performs without the extra support. The maximum static deflection under gravity was 0.45 mm. This distance is small enough

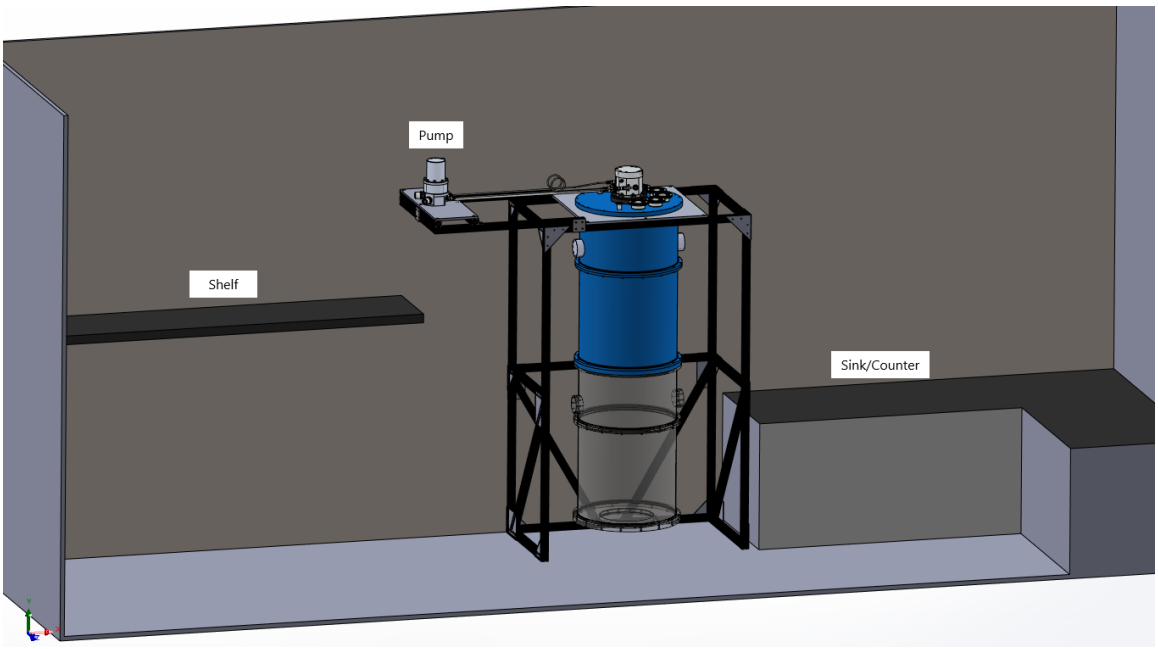

Figure 61. CAD model of the new Baby Beluga mount inside the lab room to show that it fits.

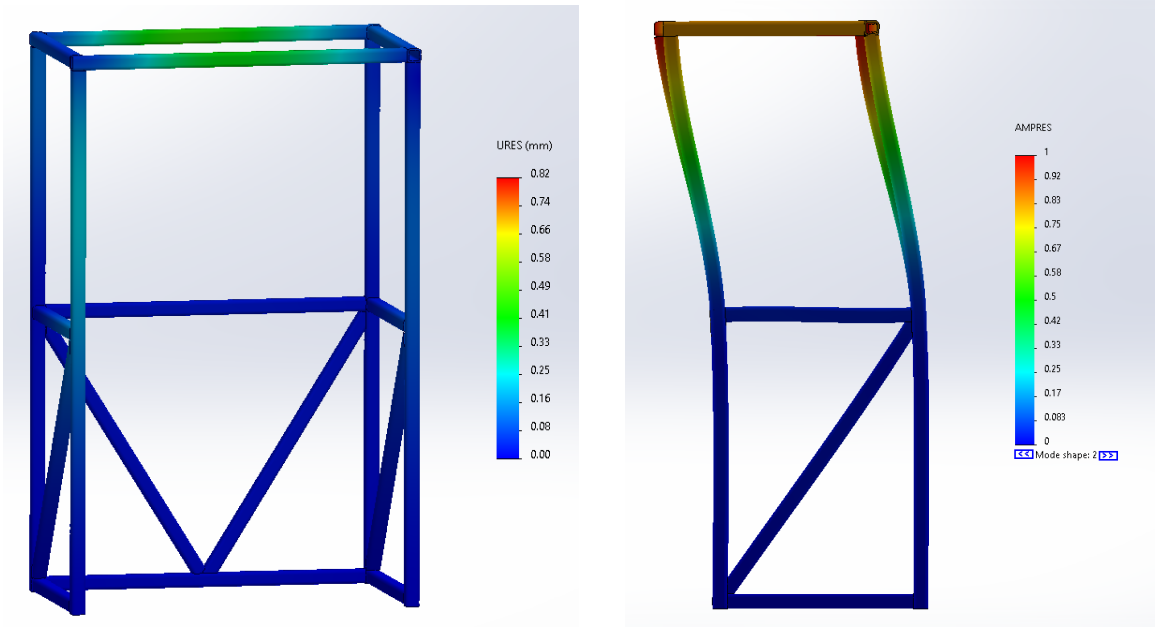

Figure 62. Static (left) and vibration (right) analysis for the Baby Beluga mount.

Figure 63. Image of Baby Beluga without its 300 K shell installed on its new mount in the lab.

to not cause any strain in the helium lines. The first resonant frequency mode occurs at 12.5 Hz in a shape that is suppressed by fixing the mount to the wall. The first 3 resonances can be shifted to higher frequencies simply by fixing the mount to the wall. Since the design met all of the requirements, the mount was constructed. Figure 63 shows Baby Beluga installed on its new mount in the lab.

4.2 Microwave Kinetic Inductance Detectors

Figure 64 shows an image and model of prototype MKIDs designed by NIST-Boulder for use in TolTEC (Austermann et al. 2018). Each TolTEC pixel contains two lumped-element MKIDs that measure perpendicular linear polarization directions. Light is absorbed by the inductors which are the vertical and horizontal bars inside the circular portion of the detector. The inductor strips are made of TiN/Ti layers and each inductive component is made to be identical. The resonator capacitor is trimmed to have a unique capacitance for each detector. This specifies the unique resonant frequency of each detector.

Each resonator is then capacitively coupled to to the transmission line (feedline) to be read out simultaneously. Mauskopf 2018 provides a description of the microwave response for capacitively coupled lumped-element MKIDs. Figure 65 shows a schematic of a lumped-element MKID. The resonant frequency of an MKID is describe by equation 4.1.

$$\omega_0 = 2\pi f_0 = \frac{1}{\sqrt{L_r(C_c + C_r)}} \tag{4.1}$$

Where L_r is the resonator inductance which combines the standard inductance of the detector plus the kinetic inductance which is affected by the absorbed light. C_r is

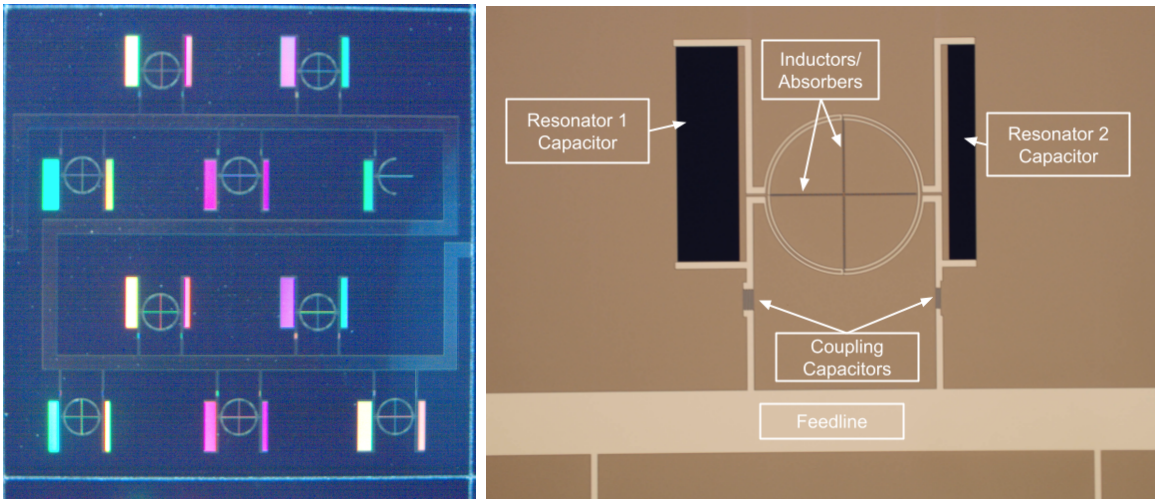

Figure 64. *Left:* Image of a prototype array. *Right:* Model shows a single pair of TolTEC detectors. Light is detected on the vertical and horizontal bars inside the circle. Images from Austermann et al. 2018

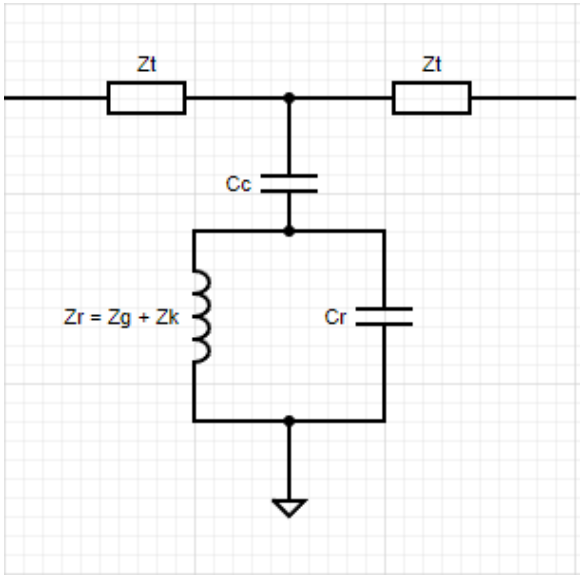

Figure 65. Schematic of a simple capacitively coupled kinetic inductance detector.

the resonator capacitance that is tuned to give each resonator a different resonance frequency. C_c is the capacitance used to couple the resonator to the transmission line.

Kinetic inductance occurs in superconductors as a result of a material's inertia in the presence of an electromotive force, since all particles want to move at a constant

velocity unless acted upon by an outside force. As an example, the kinetic inductance through a length (l) of wire with a cross-sectional area, A, can be calculated. The current through a wire is:

$$I = nq\nu A \tag{4.2}$$

where n is the number of charged particles, q is their charge, and ν is their velocity. Solve 4.2 for the velocity and take the derivative with respect to time:

$$\nu = \frac{1}{nqA} I \tag{4.3}$$

$$\frac{d\nu}{dt} = \frac{1}{nqA} \frac{dI}{dt} \tag{4.4}$$

Using Newtonian physics and the Lorentz force of a charged particle moving through an electric field (E) gives:

$$F = ma = qE = \frac{qV}{l} \tag{4.5}$$

where V is the voltage. Solve for the voltage and use the definition of acceleration:

$$V = \frac{mla}{q} = \frac{ml}{q} \frac{d\nu}{dt} \tag{4.6}$$

Substitute equation 4.4 into equation 4.6:

$$V = \frac{ml}{nq^2 A} \frac{dI}{dt} \tag{4.7}$$

The relationship between voltage, current and inductance is:

$$V = L \frac{dI}{dt} \tag{4.8}$$

Finally a description of kinetic inductance L_k can be found by substituting equation 4.8 into equation 4.7.

$$L_k = \frac{ml}{nq^2 A} \tag{4.9}$$

For kinetic inductance detectors, the number of superconducting charges, n, decreases when electromagnetic radiation is absorbed as described by Mattis and Bardeen 1958. Increasing the inductance, the absorption of light causes the resonant frequency to shift to a lower frequency. By monitoring the resonant frequencies, instruments can then use MKIDs to detect light. Input powers and operating temperature can also cause shifts in the resonant frequencies. It is important to characterize the shifts caused by non-light sources to ensure light detections can be identified.

4.3 Cryostat Testing of MKIDs

I was interested in looking at the response of kinetic inductance detectors to different temperatures and input powers. To use these devices, I needed to cool the MKIDs to their sub-kelvin operating temperature. The prototype TolTEC MKID devices were mounted on the mK-stage of the Baby Beluga cryostat shown in Figure 66. Each detector casing had its own temperature sensor and a heater to adjust the temperature. The heater is a resistor stuck to a copper strip with epoxy and bolted to the top of the device. A copper base was machined for each of the devices since the mounting bolt pattern of the device did not match the bolt pattern on the mK-plate. The aluminum devices are bolted to the copper base and the copper base was bolted to the plate.

Figure 67 shows the AC wiring diagram for the readout chains in the cryostat. There were two TolTEC devices, I focused on the device labeled TolTEC 2 for my measurements. On the input line, there was 30 dB of attenuation inside the cryostat to reduce the input signal from the Vector Network Analyzer (VNA) and prevent detector saturation. A DC block between the 4 K-stage and the 350mK-stage prevented any

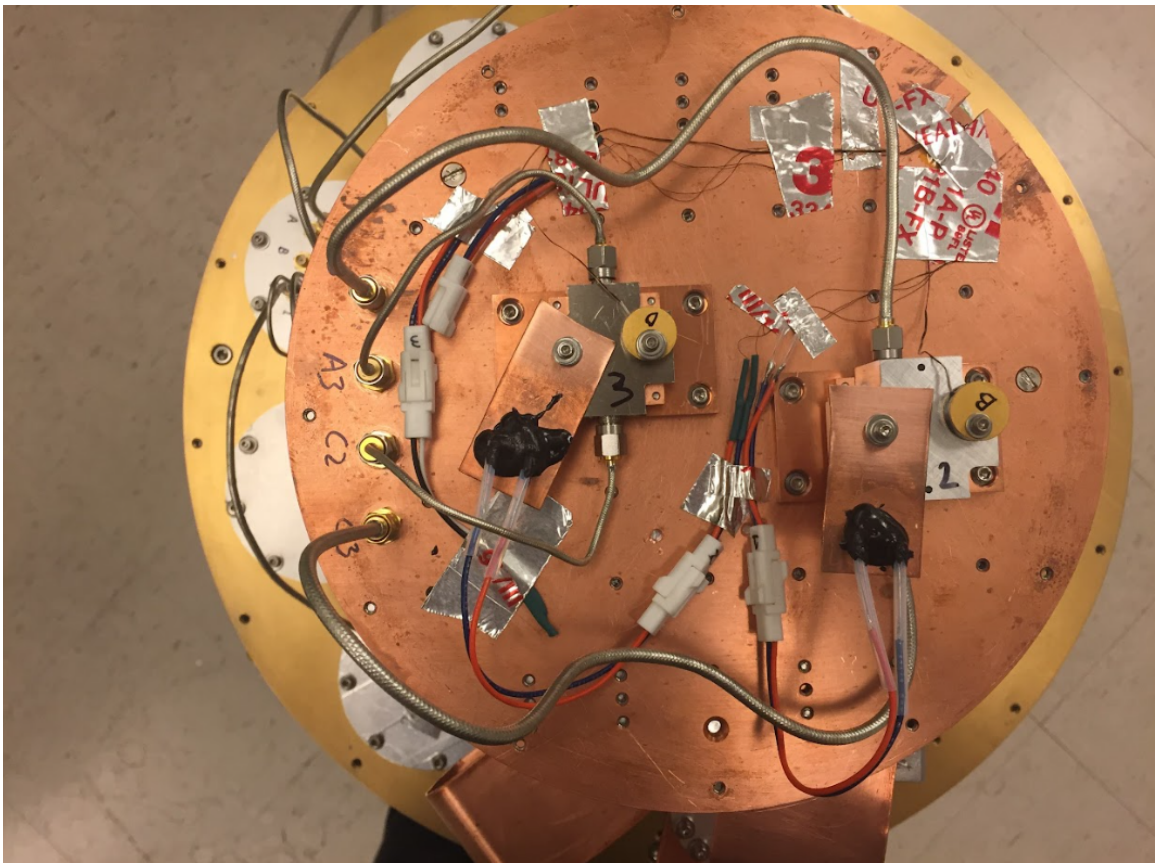

Figure 66. The two prototype TolTEC MKID arrays mounted on the mK-stage of Baby Beluga.

DC signals from reaching the detectors and helped reduce the thermal conduction along the input coaxial cable line. The detector box was mounted to the 250 mK-stage. On the output line, another DC block reduced the thermal conduction along the output line. A 4 K low noise amplifier (LNA) amplified the output signal from the detectors to increase the signal-to-noise ratio (SNR).

To test the MKIDs, I used a VNA to measure the s-parameters of the devices. The VNA uses two test ports to measure the scattering parameters of the network to show how a signal travels through it. Scattering parameters represent how waves are transmitted and reflected off of the different ports. For a two port system there are

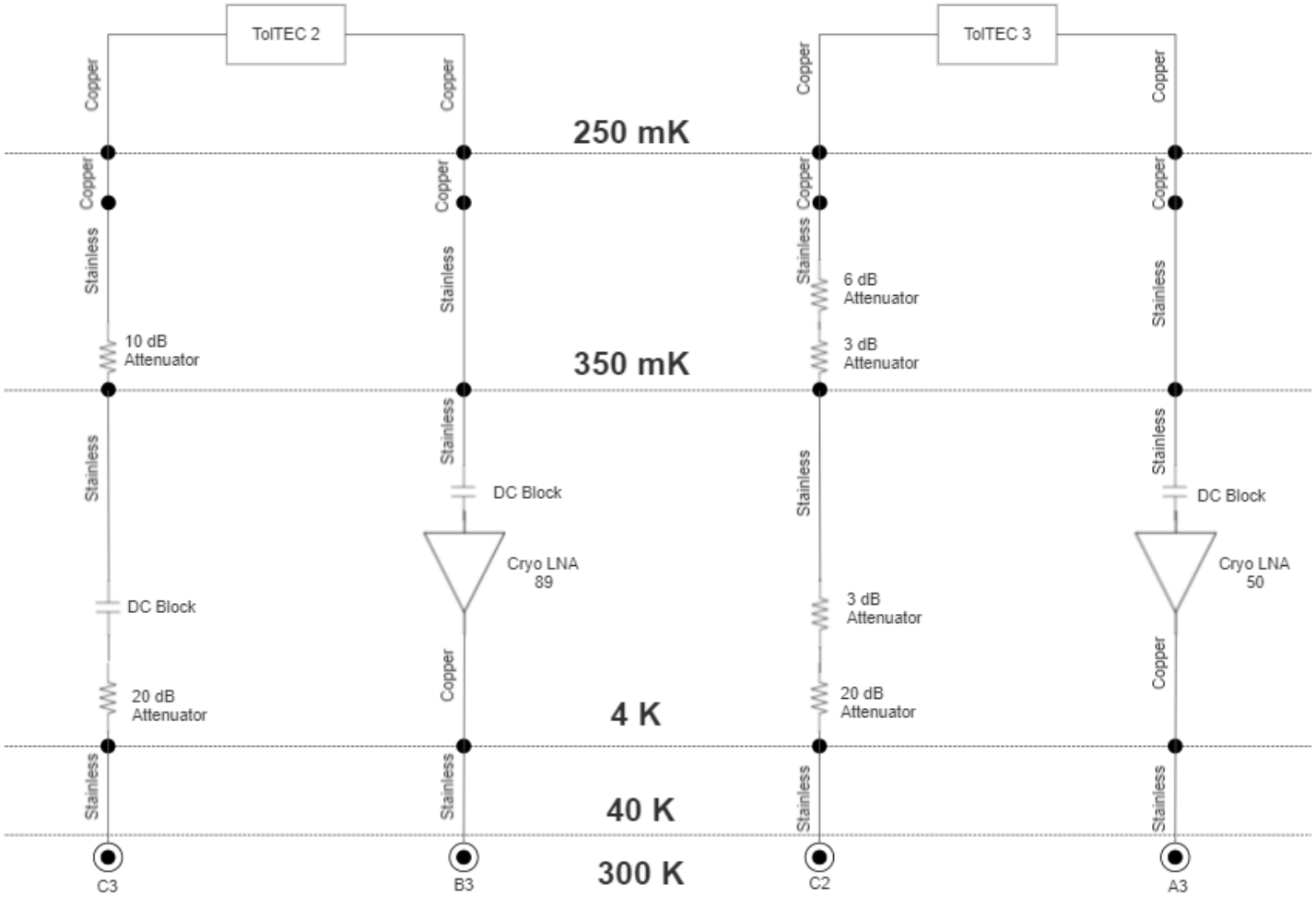

Figure 67. AC Wiring Diagram of Baby Beluga for the Testing of the Prototype TolTEC MKID Detectors.

4 s-parameters shown in equation 4.10 (Pozar 2011). S21 refers to the transmission from port 1 to port 2. Similarly, S12 is the transmission from port 2 to port 1. While S11 and S22 refer to the signals reflection off of ports 1 and 2 respectively.

$$S = \begin{vmatrix} S11 & S12 \\ S21 & S22 \end{vmatrix} \tag{4.10}$$

Figure 68 shows the s-parameters of the MKID array zoomed in on a single resonator. The S21 curve shows the transmission from the input to the output of the cryostat. The dip in the center occurs at the resonant frequency of the MKID. The MKID network is dependent on the direction because of the LNA on the output line. The amplifier increases the signal-to-noise on the output, allowing the resonance to be seen. The S12 curve shows the transmission from the output of the cryostat to the input. This curve is very noisy because very little signal is being transmitted in this direction.

The first set of tests measured the MKID's response to different readout powers or biases. Increasing the readout power will cause the resonant frequency to shift to lower frequencies and decrease the depth of the resonance. At high readout powers, the KIDs can be saturated causing the detectors to bifurcate. Bifurcation means the detector has two possible responses at the same readout frequency. If light absorption causes the detectors to switch between the different responses the system would need to be rebiased (Mauskopf 2018). KIDs should be biased with a readout power below the bifurcation point.

Figure 69 shows the transmission through an MKID resonator with different readout powers. I selected a single detector that had a deep resonance at my starting power of -20 dBm. Then I measured the same detector with lower powers. At -45 dBm, the signal started to become noisy. Then I increased the power. As the

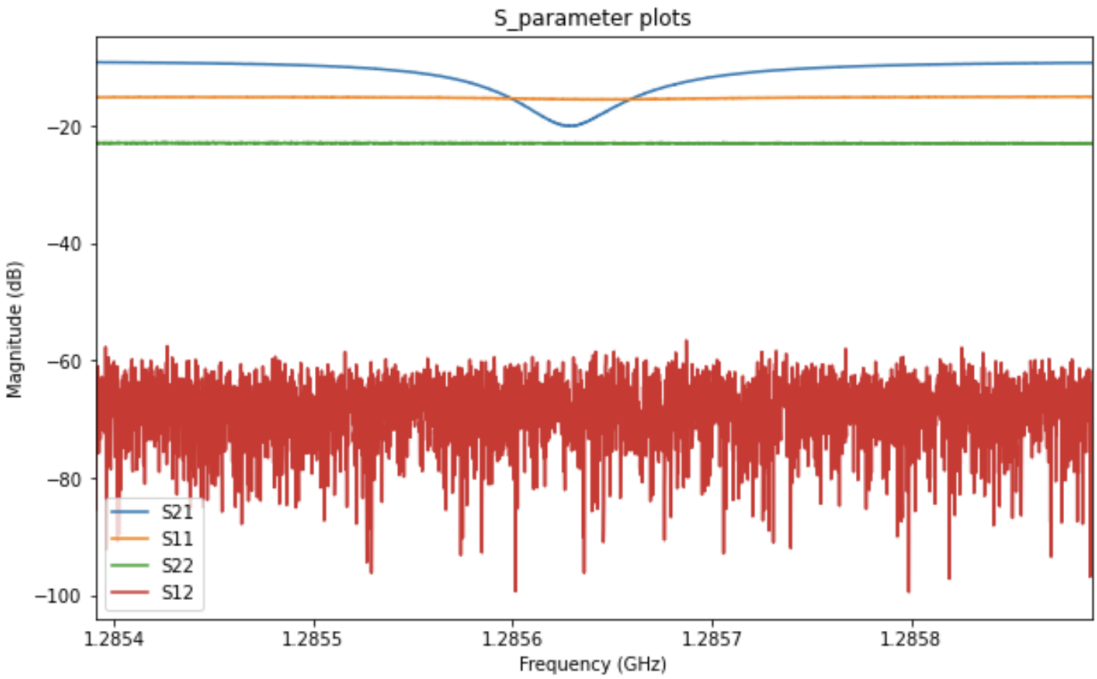

Figure 68. This plot shows the S-parameters of a single MKID resonator.

power increased, the resonance shifted to lower frequencies, the depth of the resonance decreased, and the shape of the resonator became less symmetrical. This reduction in symmetry showed that the detector was reaching the point of saturation.

The second set of tests measured the MKID's response to different detector temperatures. Changes in the resonant frequency and depth happen because of changes in quasiparticle density of the superconductor. These detectors are completely enclosed in their aluminum casing. They are considered dark detectors since no light is being detected. This means that the quasiparticle density is made of thermally generated quasiparticles (Mauskopf 2018). Higher temperature should equate to more quasiparticles. Resonances should shift to lower frequencies and decrease in depth as the temperature increases.

Figure 70 shows the transmission through the MKID resonator with different

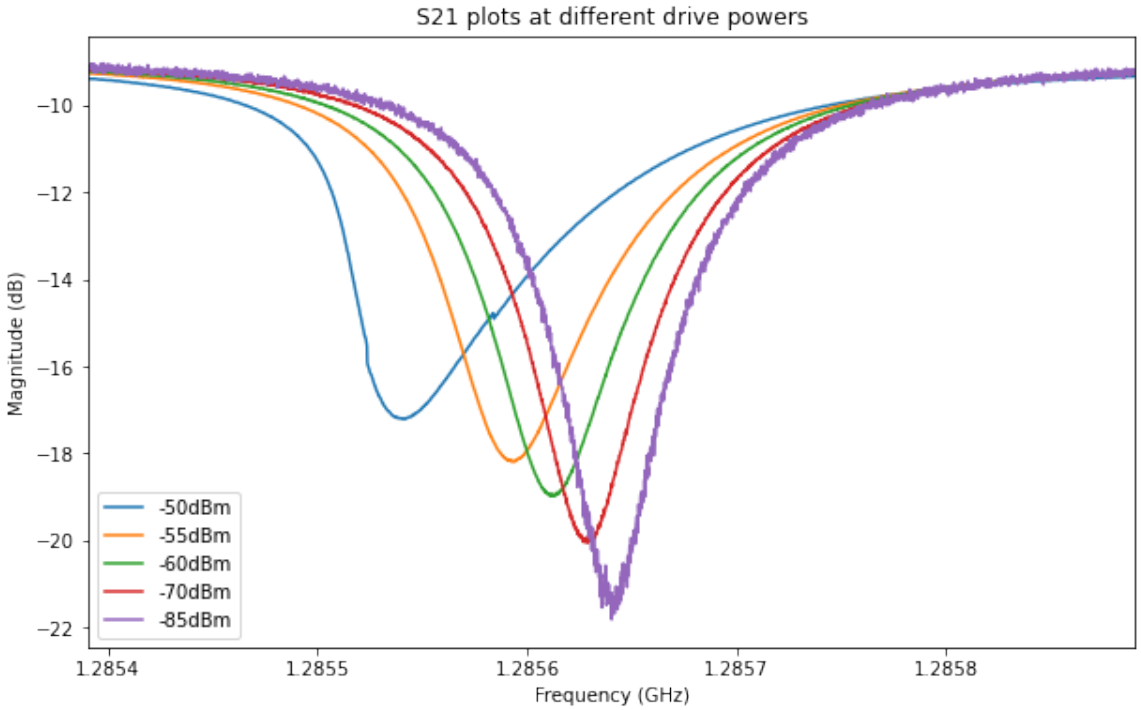

Figure 69. Transmission through an MKID resonator with different drive powers.

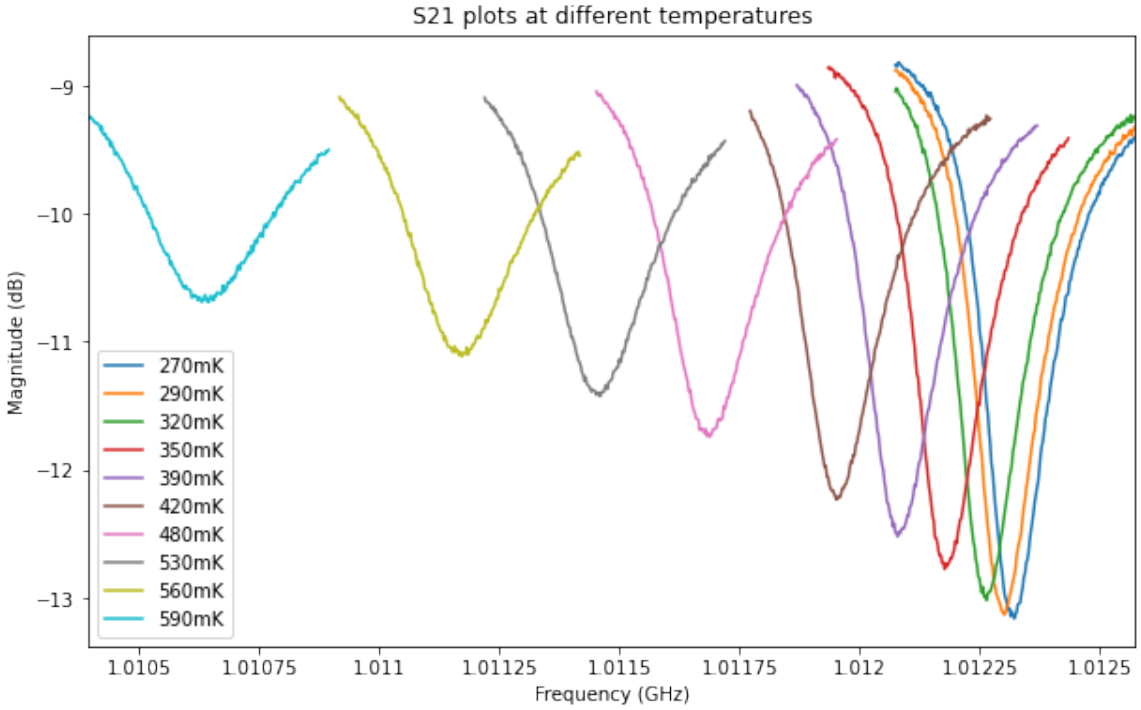

Figure 70. Transmission through an MKID resonator at different temperatures.

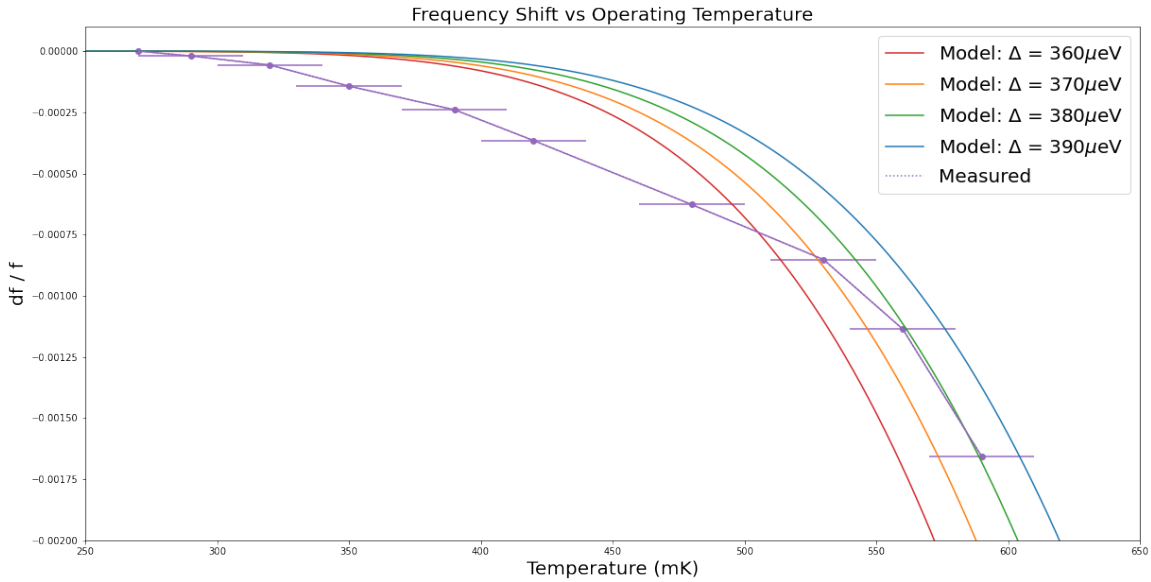

Figure 71. Frequency shift of the resonator versus temperature. This plot compares the frequency shifts measured in the lab with multiple fits of the model.

detector temperatures. These measurements were taken with a different resonator from the power measurements. The initial measurement was taken once the cryostat had cooled and stabilized at its operating temperature. For this cooldown, the mK-stage reached a temp of 266 mK. I then applied a small DC current to the heater attached to the detector. I monitored the temperature sensor until it stabilized at a new temperature. The temperature sensors stabilized to a temperature measured with an uncertainty of 20 mK. Then I measured the s-parameters of the network again. I repeated this process, increasing the DC current to collect data at 10 different temperatures. As predicted, the resonance shifts to lower frequencies when the temperature is increased. The depth of the resonance also decreases as the temperature increases.

The thermal response of MKIDs can be derived from expressions of the Mattis-Bardeen theory to predict the frequency shift in MKIDs at different temperatures (Mattis and Bardeen 1958). The following equation from Mauskopf 2018 can be

integrated with respect to temperature to show the temperature, T, dependence of resonant frequency, f_{res}:

$$\frac{df_{res}}{dT} = \frac{\alpha f_0 e^{-\Delta_0/kT}}{T}\sqrt{\frac{2\pi kT}{\Delta_0}}\left(\frac{1}{2}+\frac{\Delta_0}{kT}\right)\left(1+\sqrt{\frac{2\Delta_0}{\pi kT}}e^{-\xi}I_0(\xi)\right) \tag{4.11}$$

where k is the Boltzmann constant, $\hbar$ is Planck's constant, I_0 is a Bessel function, and ξ is calculated with the following equation:

$$\xi = \frac{\hbar\omega}{2kT} \tag{4.12}$$

The kinetic inductance fraction, α, is the ratio of the kinetic inductance to the total inductance of the resonator. For the TiN/Ti inductors used in TolTEC this value is approximately 1.

$$\alpha = \frac{L_K}{L_{tot}} \tag{4.13}$$

Δ_0 is the superconducting energy gap. This is a material property that I do not know for TiN/Ti resonators. I used this variable as a fit value in my analysis. Figure 71 compares the measured results with four different Δ_0 values between 360-390 μeV. The horizontal error bars on the measured values show the level of instability in holding the detectors at specific temperatures in the cryostat. The measured values follow the same trends as the different models.

Chapter 5

MEASURING THE SUNYAEV-ZEL'DOVICH EFFECT WITH THE ATACAMA COSMOLOGY TELESCOPE

5.1 Sunyaev-Zel'dovich Effect and Galaxies

The Sunyaev-Zel'dovich effect occurs wherever there is hot ionized gas, such as in galaxies or galaxy clusters. For this project, I am mostly interested in measuring the SZ effect around galaxies. With this measurement, I can estimate the thermal energy in the gas around the galaxies and determine if that energy comes from a combination of gravitational heating and shock heating from AGN feedback. Spacek et al. (2016) worked out models of gas heating with and without AGN feedback. The model for thermal energy of a galaxy which does not include AGN feedback is given by the following equation

$$E_{therm,gravity} = 5.4^{+5.4}_{-2.9} \times 10^{60}\, erg\, \frac{M_{stellar}}{10^{11} M_{\odot}} (1+z)^{-3/2}. \tag{5.1}$$

An estimate of the AGN feedback heating can be made using the model described in Scannapieco and Oh (2004). The energy is characterized as the heating of gas by a fraction ϵ_k of the total bolometric luminosity of the AGN. This gives the following equation for the thermal energy that includes AGN feedback

$$E_{therm,feedback} = 4.1 \times 10^{60}\, erg\, \epsilon_{k,0.05}\, \frac{M_{stellar}}{10^{11} M_{\odot}}\, (1+z)^{-3/2}, \tag{5.2}$$

For this project, I follow the procedure described in Spacek et al. (2017). I adopt a ΛCDM model from Planck Collaboration et al. (2016). The Hubble constant is $h = 0.68$ with units of 100 km/s/Mpc. The total matter, vacuum, and baryonic

densities are $\Omega_0 = 0.31$, $\Omega_\Lambda = 0.69$, and $\Omega_b = 0.049$, respectively in units of critical density.

The structure of this chapter is as follows: in Section 2, I discuss the data that will be used to make the tSZ measurements. In Section 3, I explain how I find the galaxies in the ACT CMB maps. In Section 4, I discuss how I filter the ACT images. In Section 5, I explain the stacking procedure. In Section 6, I remove dust from the 148 GHz stacks. In Section 7, I discuss the implications for AGN feedback.

5.2 Data

I need a large number of galaxies for the stacking analysis. Therefore this analysis will focus on the Stripe-82 region, which has been imaged in multiple wavelengths by many telescope surveys, including the Sloan Digital Sky Survey (SDSS), the Wide-field Infrared Survey Explorer (WISE), the Dark Energy Survey (DES) and the ACT. This area of the sky has data available in ultraviolet, visible, infrared, and microwave bands of light, giving a lot of information about the galaxies in Stripe-82. The Stripe-82 region runs from -1.25 deg. to 1.25 deg. declination and -65 deg. to 60 deg. right ascension, with an area of 312 square degrees.

I received a new catalog containing 5726 sources that was created using data from DES and WISE. Galaxies best suited for the tSZ measurements are massive elliptical galaxies with redshifts $0.5 \leq z \leq 1.5$. These galaxies were selected from the WISE catalog with over 500 million sources with a signal-to-noise ratio greater than 5.

Table 10 shows the average values of some of the relevant galaxy parameters. I am focused on measuring the tSZ signature around massive quiescent elliptical galaxies. The selected galaxies are older than 1 Gyr and have specific star formation rates

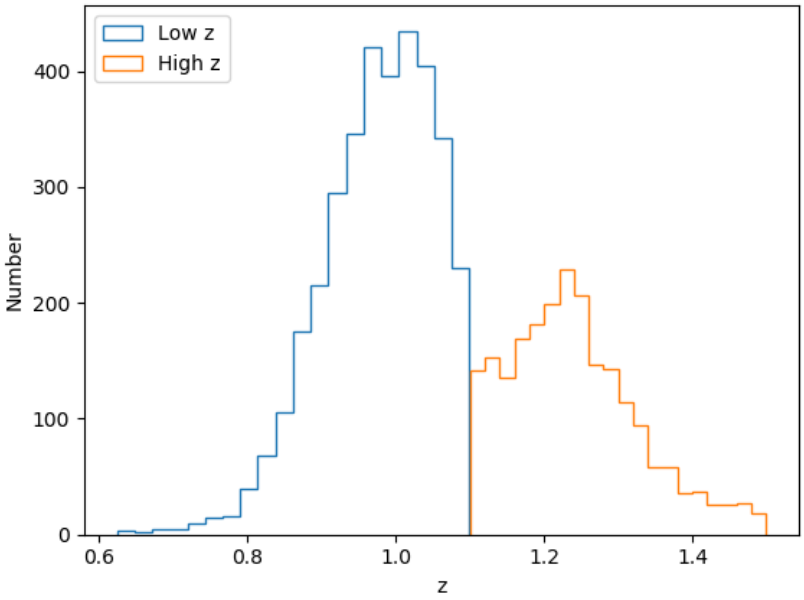

Figure 72. Redshift distributions of the galaxies selected for this analysis. Blue lines represent the 3527 low-redshift galaxies ($0.5 \leq z \leq 1.1$) and orange lines represent the 2199 high-redshift galaxies ($1.1 \leq z \leq 1.5$).

Table 10. Mean Values of Parameters for the Galaxies Used in This Analysis.

Cut	z range	Number	z	Mass ($M_{\odot}$)	Age (Gyr)	l_{ang} (Gpc)
ALL	0.5–1.5	5726	1.08	5.00x10^{11}	2.65	1.706
Low	0.5–1.1	3527	0.97	4.45x10^{11}	2.61	1.677
High	1.1–1.5	2199	1.24	6.02x10^{11}	2.71	1.754

$\leq 0.01 Gyr^{-1}$. This gives galaxies that are not actively forming stars. Figures 72, 73 and 74 show the redshift, mass and age distributions of the selected galaxies.

The 6 m Atacama Cosmology Telescope is located on Cerro Toco in Chile. The data used in this analysis was taken with the Millimeter Bolometric Array Camera (MBAC). The data that covers the equatorial Stripe-82 region is from ACT seasons 3 and 4 using the 148 and 220 GHz bands of light.[2] I will use the "src_free" data,

[2]https://lambda.gsfc.nasa.gov/product/act/act_maps2013_get.cfm

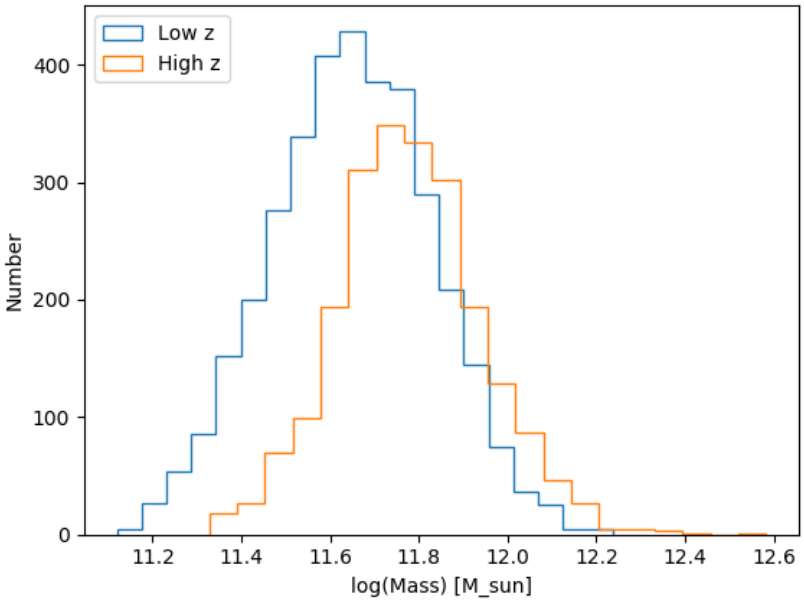

Figure 73. Mass distributions of the galaxies selected for this analysis. Blue lines represent the 3527 low-redshift galaxies ($0.5 \leq z \leq 1.1$) and orange lines represent the 2199 high-redshift galaxies ($1.1 \leq z \leq 1.5$).

where the point sources have been removed, and the "1way" labeled maps made from the entire subset of data, since I am not doing power spectrum analysis.

In the ACT 148 GHz band, I should measure a significant reduction in photons since this frequency is well below the null frequency of 217.6 GHz. At the ACT 220 GHz band I should see no results since it is very close to the null frequency where the tSZ effect does not occur (Spacek et al. 2017).

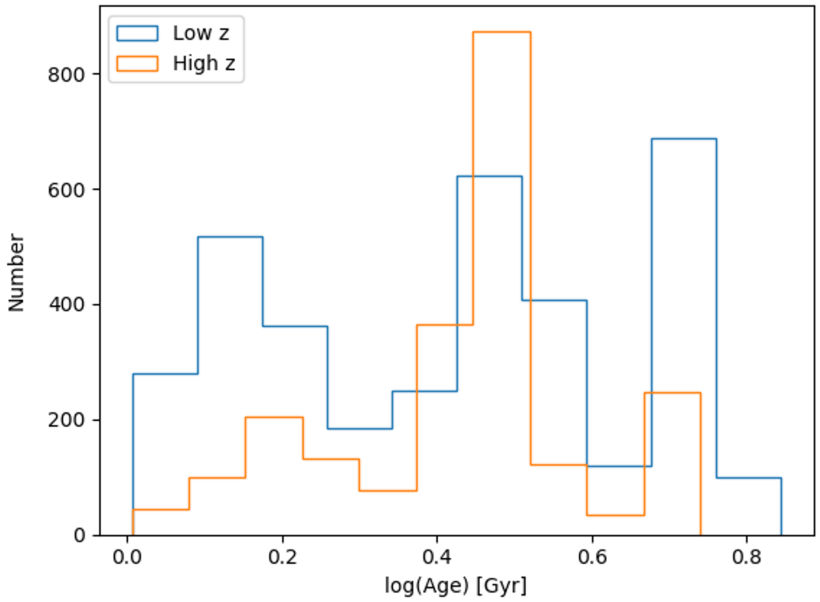

Figure 74. Age distributions of the galaxies selected for this analysis. Blue lines represent the 3527 low-redshift galaxies ($0.5 \leq z \leq 1.1$) and orange lines represent the 2199 high-redshift galaxies ($1.1 \leq z \leq 1.5$).

Table 11. Values from The .fits File Header Used for Coordinate System Transformation.

X-axis Variable	Value	Y-axis Variable	Value
NAXIS1	38275 pix	NAXIS2	611 pix
CTYPE1	RA	CTYPE2	DEC
CRPIX1	7972 pix	CRPIX2	292 pix
CRVAL1	0 deg	CRVAL2	0 deg
CDELT1	-0.00825 deg/pix	CDELT2	0.00825 deg/pix

5.3 Locating Galaxies

First, I need to be able to locate the galaxies within the ACT CMB maps. Right ascension (RA) and declination (DEC) values can be converted into pixel values using the information in the header shown in Table 11.

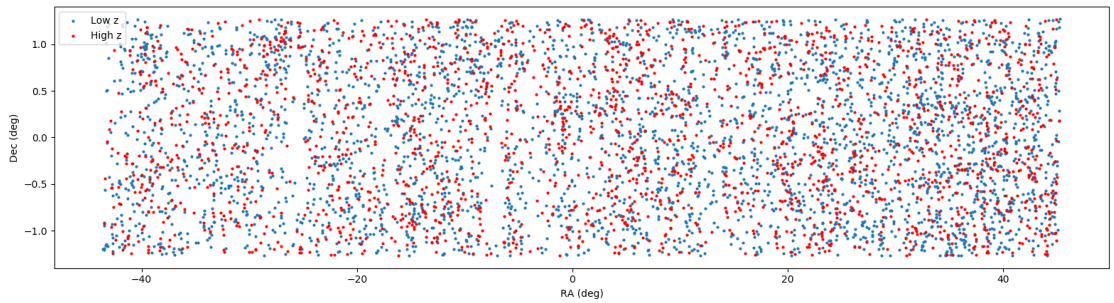

Figure 75. Sky locations of the galaxies used to make the tSZ measurements. Note that this image has been stretched vertically for clarity. Blue represents the 3527 low-redshift galaxies ($0.5 \leq z \leq 1.1$) and red represents the 2199 high-redshift galaxies ($1.1 \leq z \leq 1.5$).

RA is found on the x-axis of the image while DEC is found on the y-axis. The CDELTn values give the change in degrees of each pixel. This can be used as a slope value. CRPIXn is the reference pixel that is mapped to the RA or DEC value shown as CRVALn. Now the intercepts can be found, since the RA and DEC origin is located at pixel (7972,292), by using the equation $y = mx + b$. Using equations 5.3 and 5.4, I can locate any galaxy within the CMB map.

$$RA = -0.00825 pixel + 65.769 \tag{5.3}$$

$$DEC = 0.00825 pixel - 2.409 \tag{5.4}$$

Figure 75 shows the positions of the galaxies on the sky. These positions can be translated to the ACT CMB maps using the procedure described above.

5.4 Filtering Maps

Before I could stack the data around the selected galaxies, the primary CMB anisotropy must be removed and the signal-to-noise ratio must be maximized. The galaxies can be represented as a slightly extended source with an angular diameter of

1.5 arcmin which is the size of the ACT beam. To remove the larger structures in the CMB, I used a Gaussian with a full width half max (FWHM) more than 3 times the size of the object that I am interested in studying. First, I filtered the image using a Gaussian with a FWHM of 5.0 arcmin. Then I subtracted the filtered image from the original image. This removed CMB structures larger than 5.0 arcmin, leaving me with only smaller secondary anisotropies like the Sunyaev-Zel'dovich effect.

5.5 Stacking Galaxies

The stacking analysis results in 2 final images for each of the three cuts of galaxies. I start by locating the selected galaxies within the filtered ACT maps for seasons 3 and 4. Then I create a 8.4×8.4 arcmin (17×17 pixel) stamp around each of the galaxies. These individual stamps are then averaged together, resulting in two stacked stamps for each band in each season. Finally, the stamps for each season were averaged together. Figure 76 shows the stacking results using all 5726 galaxies from the catalog.

Figure 76 shows a signal close to zero. There is no detection of the tSZ effect in this stack. I expected to see a negative signal at 148 GHz since it is below the null frequency of 217.6 GHz. Looking at the 220 GHz stack (Figure 76), I expected to see no signal since it is very close to the null frequency. However, this stamp shows a large positive signal. This seems to indicate that the tSZ signal is obscured by a significant contaminating signal, most likely dust.

To estimate the uncertainty in the in my measurements, I was given 8254 points generated from many random points in Stripe-82 on the sky. These points were selected from the larger group of random points using the same contaminant source

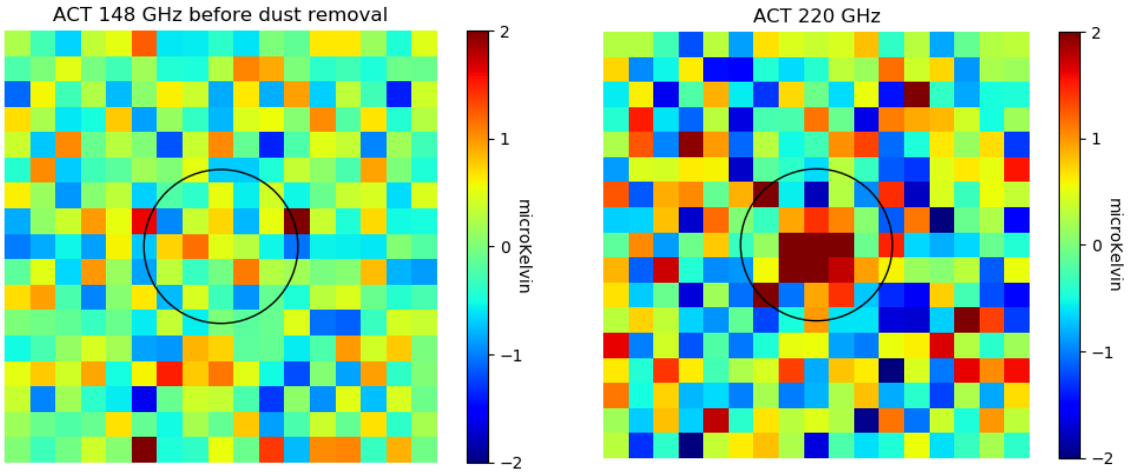

Figure 76. Season-averaged galaxy stamps for the two different frequencies: 148 GHz (left) and 220 GHz (right). These are the stacks for all 5726 galaxies. Units are μK, with black circles representing the 1.5 arcmin radius aperture used for the measurements.

cuts that were applied to the galaxy catalog. I applied the same stacking method described above to these random points on the sky. Once these season averaged stacks were created, I calculated the root mean square (RMS) value of the image. I then scaled this value using a ratio of the number of random points to the number of galaxies in the catalog.

$$\sigma_{pix} = \sqrt{\frac{N}{n}} RMS \tag{5.5}$$

In equation 5.5, $N = 8254$ and n is the number of galaxies (5726 for all, 3527 for low-redshift, and 2199 for high-redshift). The results for 1.5 arcmin sums and uncertainties are shown in Table 12. The shaded column highlights the 1.5 arcmin radius sum values for each of the galaxy cuts. I want to make sure I measure the whole galaxy, by increasing the radius I can estimate the size. Looking at the 220 GHz band, the signal should increase as I increase the radius until I reach the edge of the signal. 1.5 arcmin is the peak for the stacks of all galaxies and the low-redshift cut.

Table 12. Season-averaged Sums Before Dust Removal Measured with Different Radial Sizes.

Cut	Band (GHz)	1.0 arcmin ($\mu K arcmin^2$)	1.5 arcmin ($\mu K arcmin^2$)	2.0 arcmin ($\mu K arcmin^2$)
ALL	148	0.72±0.54	0.29±0.88	0.44±1.05
Low	148	0.17±0.66	-0.29±0.21	0.37±1.29
High	148	1.60±0.85	1.22±1.09	0.55±1.66
ALL	220	4.66±0.73	5.31±1.20	4.62±1.42
Low	220	3.79±0.95	4.99±1.56	4.00±1.85
High	220	6.06±1.23	5.84±2.03	5.62±2.40

While the high-redshift cut decreases, the 1.5 arcmin signal is within the uncertainty of the 1.0 arcmin signal.

It is clear that there contaminating signal in the measurements. This requires separating the tSZ signal from the contaminating signal. This will be addressed in the following section.

5.6 Removing Dust

There is significant dust contamination in the stacks that affects the tSZ measurements. Even though the galaxies selected have very little dust, the stacking analysis allows the dust to be seen. To obtain better results, I need to model and remove any contamination due to dust.

The signal in the 220 GHz band is dominated by dust since it is near the tSZ null frequency where not signal from the SZ should be seen. The dusty 220 GHz maps can be scaled by the dust spectrum down to 148 GHz and subtracted from the lower frequency maps. Dust can be modeled as a gray-body,

$$D(\nu, T) \propto B(\nu, T)\nu^{\beta} \approx x^{2+\beta}\,(Rayleigh - Jean's) \tag{5.6}$$

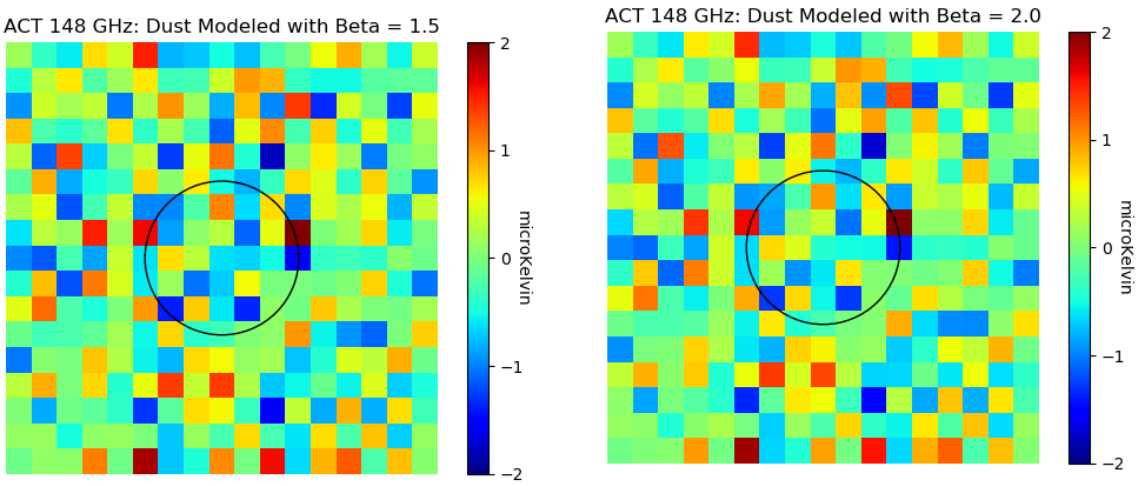

Figure 77. 148 GHz stacks for two models of dust: $\beta = 1.5$ (left) and $\beta = 2.0$ (right). These are the stacks for all 5726 galaxies. Units are μK, with black circles representing the 1.5 arcmin radius aperture used for the measurements.

where β is the emissivity of the dust, $B(\nu, T)$ is the Planck distribution for the dust, and the Rayleigh-Jean's limit can be applied since the dust peaks in infrared frequencies. Since the ACT maps have units of temperature, I need a scale factor that converts the 220 GHz temperature into a 148 GHz temperature. This scale factor is:

$$\delta T_{dust}(\nu) = \delta T_{220} \left(\frac{dB_{220}}{dT_{CMB}}\right) \left(\frac{dT_{CMB}}{dB_{\nu}}\right) \left(\frac{x_{\nu}}{x_{220}}\right)^{2+\beta} \tag{5.7}$$

$$\delta T_{dust}(\nu) = \delta T_{220} \left(\frac{x_{220}}{x_{\nu}}\right)^{2-\beta} e^{(x_{220}-x_{\nu})} \left(\frac{e^{(x_{\nu})}-1}{e^{(x_{220})}-1}\right)^{2} \tag{5.8}$$

where δT_{220} is the temperature map at 220 GHz and x is the unit-less frequency given in equation 1.3. This map can be scaled, using different emissivity values using equation 5.8, to 148 GHz.

Figure 77 shows the ACT 148 GHz band stack after dust was removed for two different values of β. Figure 77 assumes that the emissivity is $\beta = 1.5$. Figure 77 assumes that the emissivity is $\beta = 2.0$. Inside of the 1.5 arcmin aperture now appears to be marginally negative. This is more easily seen from the aperture sums shown in 13.

Table 13. Final Values After Dust Removal for 1.5 arcmin Sum, Angularly Integrated Compton-y Parameter, and Thermal Energy.

Cut	Beta	1.5 arcmin ($\mu Karcmin^2$)	1.5 Y ($10^{-7}Mpc^2$)	E_{Therm} (10^{60} ergs)
ALL	1.5	-1.34±0.29	1.3±0.3	4.3±0.9
ALL	2.0	-1.05±0.29	1.0±0.3	3.4±0.9
Low	1.5	-1.82±0.37	1.6±0.3	5.6±1.1
Low	2.0	-1.55±0.37	1.4±0.3	4.8±1.1
High	1.5	-0.57±0.47	0.6±0.5	1.9±1.6
High	2.0	-0.25±0.47	0.3±0.5	0.9±1.6

5.7 Results

The total tSZ signal can be characterized using the angularly integrated Compton-y parameter, Y. This value can be obtained from the following equation from Spacek et al. (2017):

$$Y = -3.2 \times 10^{-8} Mpc^2 \left(\frac{l_{ang}}{Gpc}\right)^2 \frac{\int \Delta T_{148}(\Omega) d\Omega}{\mu K arcmin^2} \tag{5.9}$$

Similarly, the total thermal energy surrounding a galaxy is characterized by the tSZ measurement. This value can be calculated from the 148 GHz temperature measurement using the following equation from Spacek et al. (2017):

$$E_{therm} = -1.1 \times 10^{60} Mpc^2 \left(\frac{l_{ang}}{Gpc}\right)^2 \frac{\int \Delta T_{148}(\Omega) d\Omega}{\mu K arcmin^2} \tag{5.10}$$

In both of these equations l_{ang} is the angular diameter distance and the temperature integral is the 1.5 arcmin sum measured from the 148 GHz stacks after dust was removed. Table 13 contains the values calculated for the angularly integrated Compton-y parameter and the total thermal energy surrounding a galaxy.

Using equation 5.1 and the redshifts and masses from Table 10, I can look at the thermal energies in the gas around the elliptical galaxies due to gravity and AGN feedback. The estimates for gravitational heating are $E_{therm,grav} = 9.0^{+9.0}_{-4.8} \times 10^{60}$erg for

all the selected galaxies, $E_{therm,grav} = 8.7^{+8.6}_{-4.7} \times 10^{60}$erg for low-redshift galaxies, and $E_{therm,grav} = 9.7^{+9.7}_{-5.2} \times 10^{60}$erg for high-redshift galaxies. The excess non-gravitational thermal energy can then be estimated by subtracting the theoretical gravitational energy from the thermal energy calculated with the tSZ measurements. The estimates for excess non-gravitational heating are $E_{therm,feed,data} = -4.3^{+9.0}_{-4.9} \times 10^{60}$erg for all the selected galaxies, $E_{therm,feed,data} = -3.1^{+8.7}_{-4.8} \times 10^{60}$erg for low-redshift galaxies, and $E_{therm,feed,data} = -7.8^{+9.8}_{-5.4} \times 10^{60}$erg for high-redshift galaxies. These are the results using the dust model with $\beta = 1.5$. All of these results are consistent with zero detection of non-gravitational heating. These galaxies have a large variation in mass which gives large error bars for gravitational energy estimate. A more detailed analysis was performed by Meinke et al. 2021 that explores the relation between thermal energy and mass by breaking a larger galaxy sample into groups by mass. The galaxy sample for ACT was too small to break into mass groups.

Chapter 6

CONCLUSIONS AND FUTURE WORK

6.1 Optics Characterization Summary

The TolTEC camera is currently installed at the LMT and is performing commissioning tasks. Using liquid nitrogen timestreams, the optical beam was centered on the tertiary mirror of the LMT. Between M3 and M4, the light travels parallel to the floor, along its designed optical axis. I measured the beam at two locations using an IR source. The beam maps created were compared to the Zemax optical model. At the two locations the beam's shape matched the optical model. Additional focus adjustments were done by changing the position of M2 along the optical axis. Astigmatism corrections were made by changing the shape of the primary mirror. Through the optical alignment process discussed in chapter 3, the TolTEC optics appear to be aligned with the LMT.

On sky beam maps shows the beam on the sky with average angular resolution of 6.06 ± 0.011" for the 1.1 mm band, 7.50 ± 0.013 for the 1.4 mm band, and 10.75 ± 0.021" for the 2.0 mm band. However, there is still some slight ellipticity to the beam shape with the beam being slightly wider in the x-direction. This could be the result of astigmatism or focus errors in the optics hopefully to be resolved once commissioning restarts.

6.2 Optics Optimization: Future Steps

There are two main optics related tasks that should be addressed once commissioning restarts. First, increasing the detector yield. The TolTEC team plans to do noise testing to better characterize the detector readout chains. By optimizing the signal-to-noise of the detectors, more detectors should be found. Noise testing will hopefully allow the problem with the missing readout chains on the 1.1 mm and 1.4 mm array to be diagnosed and fixed.

Second, further on-sky beam maps should be taken to determine the cause of the beam ellipticity. I propose looking at the FWHM of the beam in the x and y directions as adjustments are made with M2 for focus and M1 for astigmatism. Both these types of adjustments have reduced beam ellipticity in previous measurements. If the ellipticity cannot be removed with this method, it could point to the cryostat position needing to be adjusted. Further analysis can be done using Zemax to determine the effect that the location of the Lyot stop along the optical axis has on the ellipticity of the beam.

6.3 Galaxy Stacking with TolTEC

TolTEC is especially suited for measuring the SZ-effect. The three wavebands are located at where different SZ-features show. The 1.4 mm band is located at the null frequency while the 2.0 mm band should see a decrease in flux and the 1.1 mm band should see an increase in flux. Combined with a high angular resolutions of $\approx 6 - 11$", TolTEC could get more precise measurements for the galaxy stacking project. This

would give a better measurement of the thermal energy in high-redshift, quiescent galaxies to compliment the galaxy stacks I made using ACT data.

REFERENCES

Adam, R., Adane, A., Ade, P. A. R., André, P., Andrianasolo, A., Aussel, H., Beelen, A., et al. 2018. "The NIKA2 large-field-of-view millimetre continuum camera for the 30 m IRAM telescope." *A&A* 609:A115. https://doi.org/10.1051/0004-6361/201731503.

Austermann, J. E., J. A. Beall, S. A. Bryan, B. Dober, J. Gao, G. Hilton, J. Hubmayr, et al. 2018. "Millimeter-Wave Polarimeters Using Kinetic Inductance Detectors for TolTEC and Beyond." *Journal of Low Temperature Physics* 193, no. 3 (November): 120–127. https://doi.org/10.1007/s10909-018-1949-5.

Benson, B. A., P. A. R. Ade, Z. Ahmed, S. W. Allen, K. Arnold, J. E. Austermann, A. N. Bender, et al. 2014. "SPT-3G: a next-generation cosmic microwave background polarization experiment on the South Pole telescope." In *SPIE Proceedings,* edited by Wayne S. Holland and Jonas Zmuidzinas. SPIE, July. https://doi.org/10.1117/12.2057305.

Bradley, Larry, Brigitta Sipőcz, Thomas Robitaille, Erik Tollerud, Zè Vinícius, Christoph Deil, Kyle Barbary, et al. 2023. "astropy/photutils: 1.8.0." Zenodo, May. https://doi.org/10.5281/zenodo.7946442.

Brien, Tom, Simon M. Doyle, Edgar Castillo-Domínguez, Daniel Ferrusca, David H. Hughes, Enzo Pascale, Sam Rowe, et al. 2018. "MUSCAT: the Mexico-UK Sub-Millimetre Camera for AsTronomy." In *Millimeter, Submillimeter, and Far-Infrared Detectors and Instrumentation for Astronomy IX,* edited by Jonas Zmuidzinas and Jian-Rong Gao. SPIE, June. https://doi.org/10.1117/12.2313697.

Bryan, Sean, Jason Austermann, Daniel Ferrusca, Philip Mauskopf, Jeff McMahon, Alfredo Montaña, Sara Simon, Giles Novak, David Sánchez-Argüelles, and Grant Wilson. 2018. "Optical design of the TolTEC millimeter-wave camera." In *Millimeter, Submillimeter, and Far-Infrared Detectors and Instrumentation for Astronomy IX,* edited by Jonas Zmuidzinas and Jian-Rong Gao, 10708:48–55. International Society for Optics and Photonics, SPIE. https://doi.org/10.1117/12.2314130.

Castillo-Dominguez, E., P. Ade, P. S. Barry, T. Brien, S. Doyle, D. Ferrusca, V. Gomez-Rivera, et al. 2018. "Mexico-UK Sub-millimeter Camera for Astronomy." *Journal of Low Temperature Physics* 193, nos. 5-6 (July): 1010–1015. https://doi.org/10.1007/s10909-018-2018-9.

Coppi, Gabriele, Peter A. Ade, Peter C. Ashton, Jason E. Austermann, Erin G. Cox, Mark J. Devlin, Bradley J. Dober, et al. 2020. "In-flight performance of the

BLAST-TNG telescope platform." In *Ground-based and Airborne Telescopes VIII,* edited by Heather K. Marshall, Jason Spyromilio, and Tomonori Usuda. SPIE, December. https://doi.org/10.1117/12.2560849.

Coughlin, K. P., J. J. McMahon, K. T. Crowley, B. J. Koopman, K. H. Miller, S. M. Simon, and E. J. Wollack. 2018. "Pushing the Limits of Broadband and High-Frequency Metamaterial Silicon Antireflection Coatings." *Journal of Low Temperature Physics* 193, nos. 5-6 (December): 876–885. https://doi.org/10.1007/s10909-018-1955-7. arXiv: 1804.08368 [astro-ph.IM].

Datta, R., C. D. Munson, M. D. Niemack, J. J. McMahon, J. Britton, E. J. Wollack, J. Beall, et al. 2013. "Large-aperture wide-bandwidth antireflection-coated silicon lenses for millimeter wavelengths." *Applied Optics* 52, no. 36 (December): 8747. https://doi.org/10.1364/ao.52.008747.

Day, Peter, Henry Leduc, Benjamin Mazin, Anastasios Vayonakis, and Jonas Zmuidzinas. 2003. "A broadband superconducting detector suitable for use in large arrays." *Nature* 425 (October): 817–21. https://doi.org/10.1038/nature02037.

Dempsey, J. T., P. Friberg, T. Jenness, R. P. J. Tilanus, H. S. Thomas, W. S. Holland, D. Bintley, et al. 2013. "SCUBA-2: on-sky calibration using submillimetre standard sources." *Monthly Notices of the Royal Astronomical Society* 430, no. 4 (March): 2534–2544. https://doi.org/10.1093/mnras/stt090.

Essinger-Hileman, Thomas M., Trevor M. Oxholm, Gage L. Siebert, Peter A. Ade, Christopher J. Anderson, Alyssa Barlis, Emily M. Barrentine, et al. 2020. "Optical Design of the Experiment for Cryogenic Large-Aperture Intensity Mapping (EXCLAIM)." In *Millimeter, Submillimeter, and Far-Infrared Detectors and Instrumentation for Astronomy X,* edited by Jonas Zmuidzinas and Jian-Rong Gao. SPIE, December. https://doi.org/10.1117/12.2576254.

Fasano, Alessandro, Alexandre Beelen, Alain Benoit, Andreas Lundgren, Peter Ade, Manuel Aravena, Emilio Barria, et al. 2022. *CONCERTO: a breakthrough in wide field-of-view spectroscopy at millimeter wavelengths.* arXiv: 2206.15146 [astro-ph.IM].

Ferrusca, D., and J. Contreras R. 2014. "Weather monitor station and 225 GHz radiometer system installed at Sierra Negra: the Large Millimeter Telescope site." In *Ground-based and Airborne Instrumentation for Astronomy V,* edited by Suzanne K. Ramsay, Ian S. McLean, and Hideki Takami, 9147:914730. Society of Photo-Optical Instrumentation Engineers (SPIE) Conference Series. July. https://doi.org/10.1117/12.2055005.

Henderson, S. W., R. Allison, J. Austermann, T. Baildon, N. Battaglia, J. A. Beall, D. Becker, et al. 2016. "Advanced ACTPol Cryogenic Detector Arrays and Readout." *Journal of Low Temperature Physics* 184, nos. 3-4 (March): 772–779. https://doi.org/10.1007/s10909-016-1575-z.

Holland, W. S., D. Bintley, E. L. Chapin, A. Chrysostomou, G. R. Davis, J. T. Dempsey, W. D. Duncan, et al. 2013. "SCUBA-2: the 10 000 pixel bolometer camera on the James Clerk Maxwell Telescope." *Monthly Notices of the Royal Astronomical Society* 430, no. 4 (March): 2513–2533. https://doi.org/10.1093/mnras/sts612.

Hughes, David H., Juan-Carlos Jáuregui Correa, F. Peter Schloerb, Neal Erickson, Jose Guichard Romero, Mark Heyer, David Huerta Reynoso, et al. 2010. "The Large Millimeter Telescope." In *Ground-based and Airborne Telescopes III,* edited by Larry M. Stepp, Roberto Gilmozzi, and Helen J. Hall, 7733:773312. International Society for Optics and Photonics, SPIE. https://doi.org/10.1117/12.857974.

Institute for Basic Standards, U. S. 1977. *LNG materials & fluids: a user's manual of property data in graphic format.* Boulder, Colo: U.S. National Bureau of Standards.

Karkare, K. S., P. S. Barry, C. M. Bradford, S. Chapman, S. Doyle, J. Glenn, S. Gordon, et al. 2020. "Full-Array Noise Performance of Deployment-Grade SuperSpec mm-Wave On-Chip Spectrometers." *Journal of Low Temperature Physics* 199, nos. 3-4 (February): 849–857. https://doi.org/10.1007/s10909-020-02407-4.

Koopman, Brian J. 2018. "Advanced ACTPol: telescope systems and project status (Conference Presentation)." In *Millimeter, Submillimeter, and Far-Infrared Detectors and Instrumentation for Astronomy IX,* edited by Jonas Zmuidzinas and Jian-Rong Gao, vol. 10708. International Society for Optics and Photonics, SPIE. https://doi.org/10.1117/12.2314078.

Kurowski, P. 2022a. *Engineering Analysis with SOLIDWORKS Simulation 2022.* 5–31. SDC Publications. https://books.google.com/books?id=uptXEAAAQBAJ.

———. 2022b. *Vibration Analysis with SOLIDWORKS Simulation 2022.* 5–34. SDC Publications. https://books.google.com/books?id=-f9tEAAAQBAJ.

Lunde, E., P. Ade, M. Berthoud, R. Contente, N.S. DeNigris, S. Doyle, D. Ferrusca, et al. 2020. "The optical design and performance of TolTEC: a millimeter-wave imaging polarimeter." In *Millimeter, Submillimeter, and Far-Infrared Detectors and Instrumentation for Astronomy X,* vol. 11453. SPIE. https://doi.org/10.1117/12.2562798.

Lunde, E., M. Berthoud, N.S. DeNigris, S. Doyle, D. Ferrusca, J. Golec, S. Kuczarski, et al. 2022. "The TolTEC camera: optical alignment and characterization." In *Millimeter, Submillimeter, and Far-Infrared Detectors and Instrumentation for Astronomy XI,* vol. 12190. SPIE. https://doi.org/10.1117/12.2630340.

Lyon, K. G., G. L. Salinger, C. A. Swenson, and G. K. White. 1977. "Linear thermal expansion measurements on silicon from 6 to 340 K." *Journal of Applied Physics* 48, no. 3 (March): 865–868. https://doi.org/10.1063/1.323747.

Mattis, D. C., and J. Bardeen. 1958. "Theory of the Anomalous Skin Effect in Normal and Superconducting Metals." *Physical Review* 111, no. 2 (July): 412–417. https://doi.org/10.1103/PhysRev.111.412.

Mauskopf, P. D. 2018. "Transition Edge Sensors and Kinetic Inductance Detectors in Astronomical Instruments." *Publications of the Astronomical Society of the Pacific* 130, no. 990 (August): 082001. https://doi.org/10.1088/1538-3873/aabaf0.

Meinke, Jeremy, Kathrin Böckmann, Seth Cohen, Philip Mauskopf, Evan Scannapieco, Richard Sarmento, Emily Lunde, and J'Neil Cottle. 2021. "The Thermal Sunyaev-Zel'dovich Effect from Massive, Quiescent $0.5 \leq z \leq 1.5$ Galaxies." *The Astrophysical Journal* 913, no. 2 (June): 88. https://doi.org/10.3847/1538-4357/abf2b4. arXiv: 2103.01245 [astro-ph.CO].

Planck Collaboration, P.A.R. Ade, N. Aghanim, and et al. 2016. "Planck 2015 results. XIII. Cosmological parameters." *Astronomy and Astrophysics* 594, no. A13 (February). https://doi.org/arXiv:1502.01589.

Pozar, D.M. 2011. *Microwave Engineering, 4th Edition.* 178–185. Wiley.

Rayleigh. 1879. "XXXI. Investigations in optics, with special reference to the spectroscope." *The London, Edinburgh, and Dublin Philosophical Magazine and Journal of Science* 8 (49): 261–274. https://doi.org/10.1080/14786447908639684.

Scannapieco, E., and S.P. Oh. 2004. "Quasar Feedback: The Missing Link in Structure Formation." *The Astrophysical Journal* 608, no. 1 (June): 62–79. https://doi.org/10.1086/386542.

Shackelford, J.F. 2015. *Introduction to Materials Science for Engineers.* 210–227. Pearson.

Sobrin, J. A., P. A. R. Ade, Z. Ahmed, A. J. Anderson, J. S. Avva, R. Basu Thakur, A. N. Bender, et al. 2018. "Design and characterization of the SPT-3G receiver." In *Millimeter, Submillimeter, and Far-Infrared Detectors and Instrumentation for*

Astronomy IX, edited by Jonas Zmuidzinas and Jian-Rong Gao, 10708:187–197. International Society for Optics and Photonics, SPIE. https://doi.org/10.1117/12.2314366.

Spacek, A., E. Scannapieco, S. Cohen, B. Joshi, and P. Mauskopf. 2016. "Constraining AGN Feedback in Massive Ellipticals with South Pole Telescope Measurements of the Thermal Sunyaev-Zel'dovich Effect." *The Astrophysical Journal* 819, no. 2 (March). https://doi.org/10.3847/0004-637X/819/2/128.

———. 2017. "Searching For Fossil Evidence of AGN Feedback in WISE-Selected Stripe-82 Galaxies by Measuring the Thermal Sunyaev-Zel'dovich Effect with the Atacama Cosmology Telescope." *The Astrophysical Journal* 834, no. 2 (January). https://doi.org/10.3847/1538-4357/834/2/102.

Sunyaev, R.A., and Y.B. Zel'dovich. 1970. "Small-scale Fluctuations of Relic Radiation." *Ap&SS* 7 (3).

———. 1972. "The Observation of Relic Radiation as a Test of the Nature of X-ray Radiation from the Clusters of Galaxies." *CoASP* 4 (173).

ToolBox, The Engineering. 2017. *Beams Natural Vibration Frequency.* https://www.engineeringtoolbox.com/structures-vibration-frequency-d_1989.html.

Vieira, Joaquin, James Aguirre, C. Matt Bradford, Jeffrey Filippini, Christopher Groppi, Dan Marrone, Matthieu Bethermin, et al. 2020. *The Terahertz Intensity Mapper (TIM): a Next-Generation Experiment for Galaxy Evolution Studies.* arXiv: 2009.14340 [astro-ph.IM].

Wilson, Grant W., Sophia Abi-Saad, Peter Ade, Itziar Aretxaga, Jason Austermann, Yvonne Ban, Joseph Bardin, et al. 2020. "The TolTEC camera: an overview of the instrument and in-lab testing results." In *Millimeter, Submillimeter, and Far-Infrared Detectors and Instrumentation for Astronomy X,* vol. 11453. SPIE. https://doi.org/10.1117/12.2562331.

Zeballos, M., D. Ferrusca, J. Contreras R., and D. H. Hughes. 2016. "Reporting the first 3 years of 225-GHz opacity measurements at the site of the Large Millimeter Telescope Alfonso Serrano." In *Ground-based and Airborne Telescopes VI,* edited by Helen J. Hall, Roberto Gilmozzi, and Heather K. Marshall, vol. 9906, 99064U. Society of Photo-Optical Instrumentation Engineers (SPIE) Conference Series. July. https://doi.org/10.1117/12.2232168.

Zemax. 2011. *Zemax Optical Design Program: User's Manual.* Radian ZEMAX LLC, July.

APPENDIX A

SAMPLE OF ENGINEERING DRAWINGS FOR THE TOLTEC OPTICS

Engineering drawings are a method of conveying information about an object to specify tolerances, dimensions, and assembly instructions often for manufacturing purposes. These technical drawings should have enough details to completely describe an object without providing redundant information. Since my work involved designing the optics and mounts for the TolTEC camera, I spent time making engineering drawings for each individual component along with assembly drawings to dictate how the parts are put together. I am providing a sample of the engineering drawings to highlight some important details.

Figure 78 shows the final engineering drawing for lens 3. For the lenses it is important to include the equation for the conic section that describes the surface of the lens. This includes noting what the radius of curvature and the conic constant are so the lens can be cut in the correct shape. A detailed view of the lens edge shows the dimensions of the mounting flange. Since the each lens has AR coatings cut into its surface, the frequencies must also be listed on the drawing to ensure the proper cuts are made.

Figure 79 shows the engineering drawing for one part of a lens mount. Detailed views show closer views of smaller details that were hard to call out on the full scale view. Section views cut the parent view along the indicated line with arrows to show which side of the cut to look at. Sections views give a look at inside details of the part that cannot be viewed from a standard side view.

Figure 80 shows the engineering drawing for mirror 4. Just like with the lens drawings, it is important to include the equation for the conic section that describes the surface of the mirror. However, for mirrors, it is also important to include a surface finish specification. The triangle symbol with a tail indicates that material removal by a machine is required for the surface roughness to be 1.6 microns on scales smaller than 20 mm. The curved surface accuracy is noted to be an RMS of 60 microns on scales larger than 20 mm.

Figure 81 shows the assembly drawing for the M4/M6 mirror mount. This is a drawing that shows how each of the cut steel tubing gets welded together. Each part is numbered and listed in a parts table showing which drawing belongs to the part number and the quantity of each part that needs to be cut. In total there were 40 separate drawing pages just for each individual steel beam.

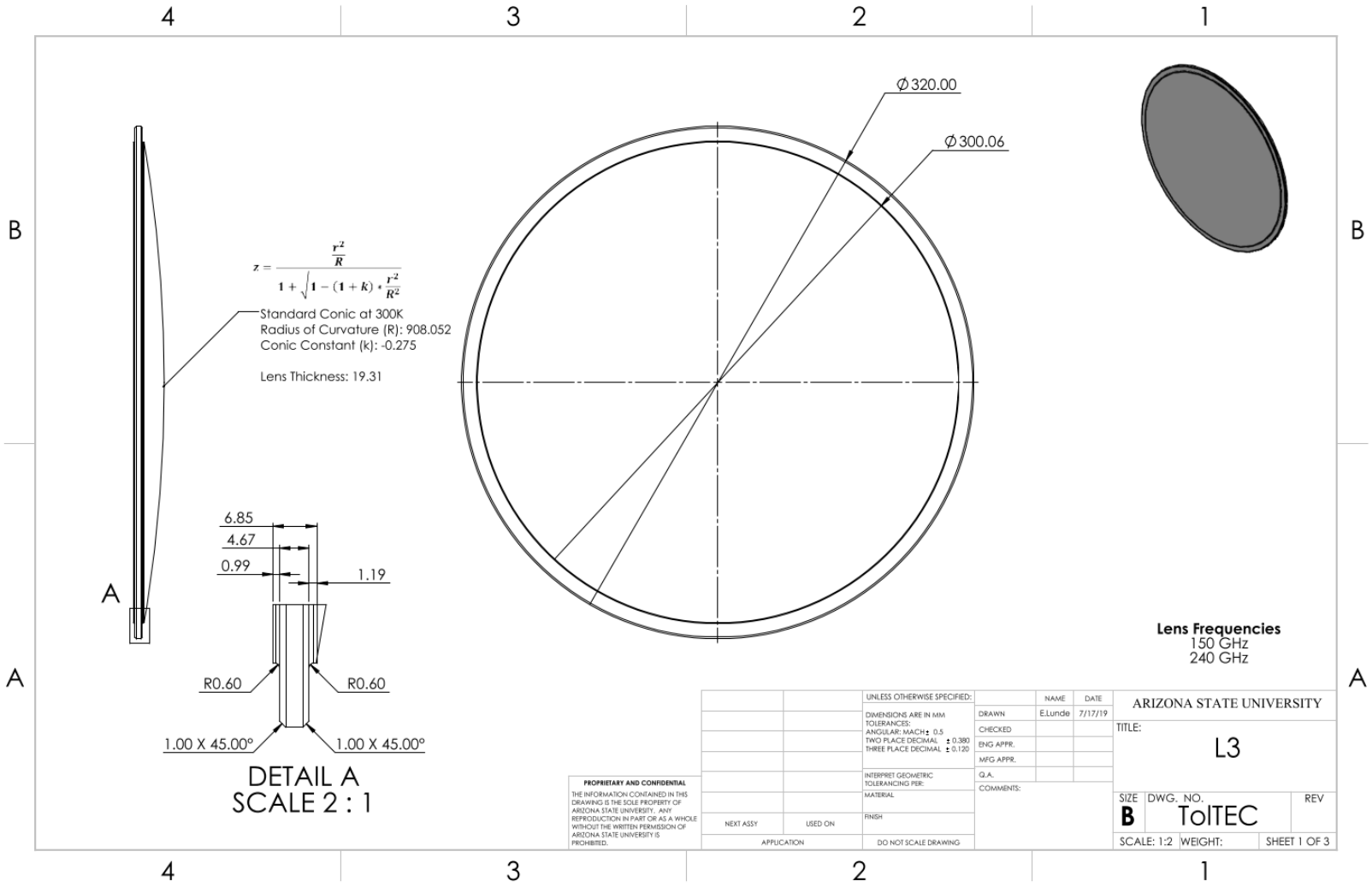

Figure 78. Lens 3 Engineering Drawing

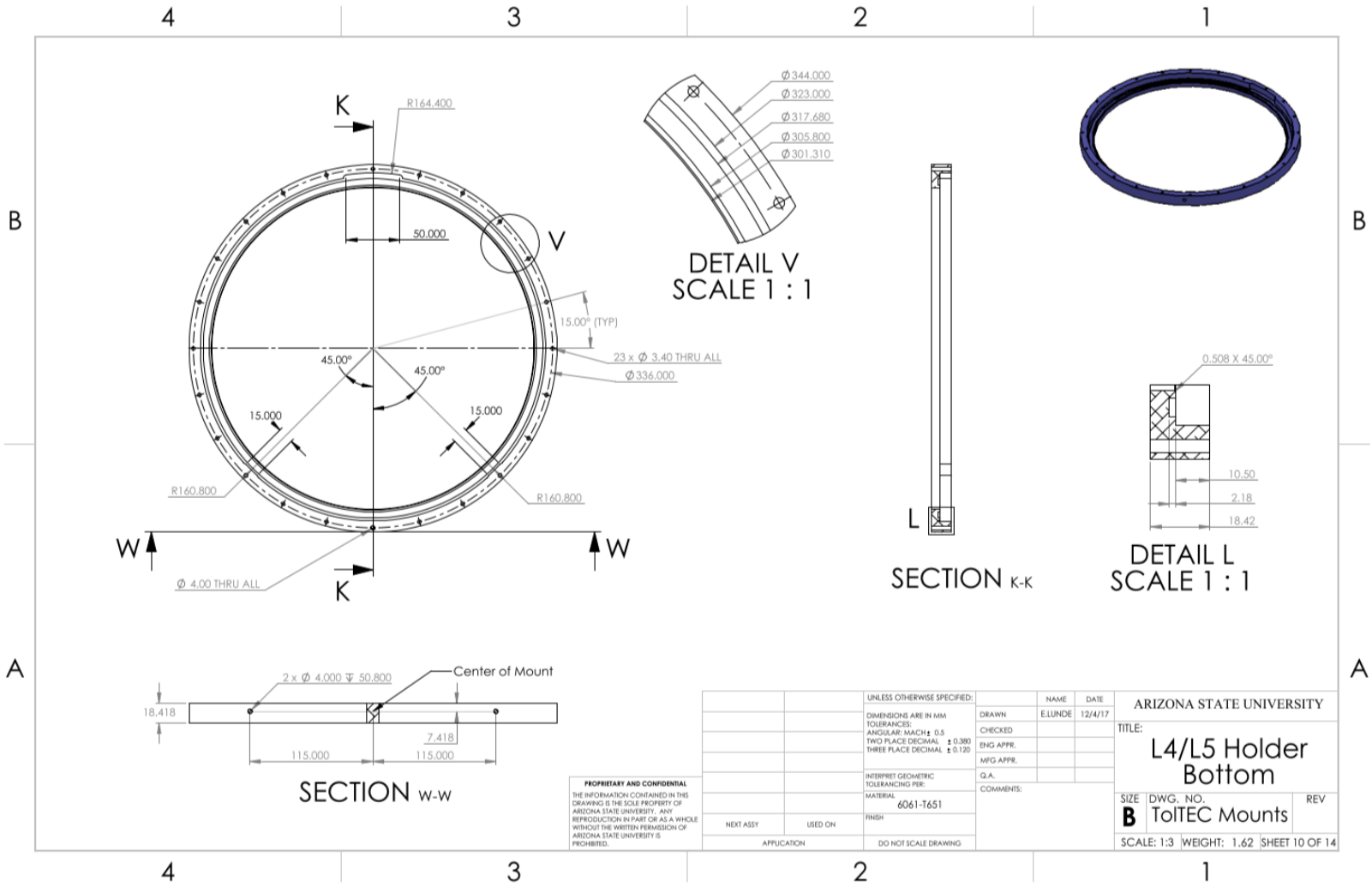

Figure 79. Lens Mount Engineering Drawing

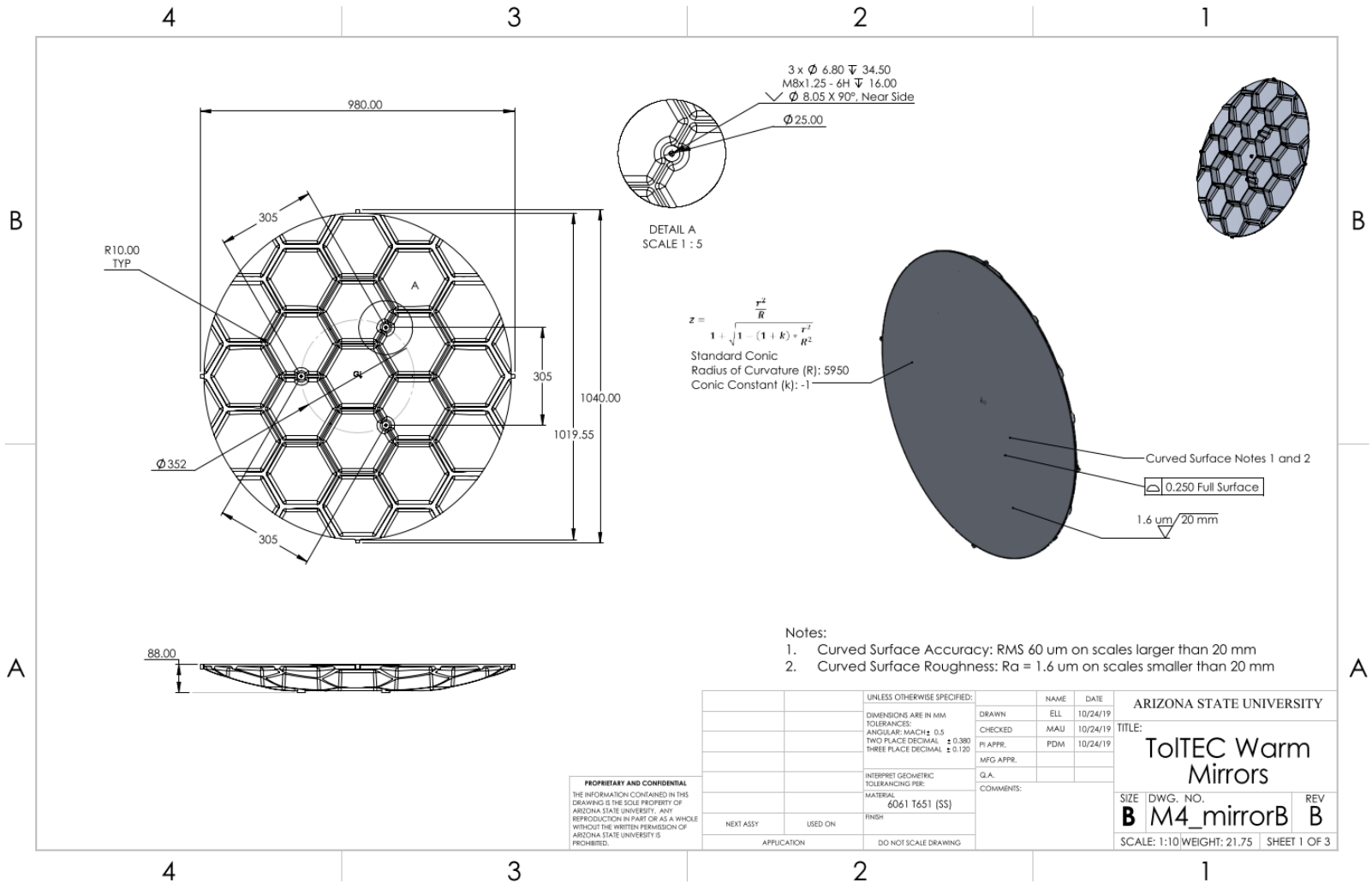

Figure 80. Mirror 4 Engineering Drawing

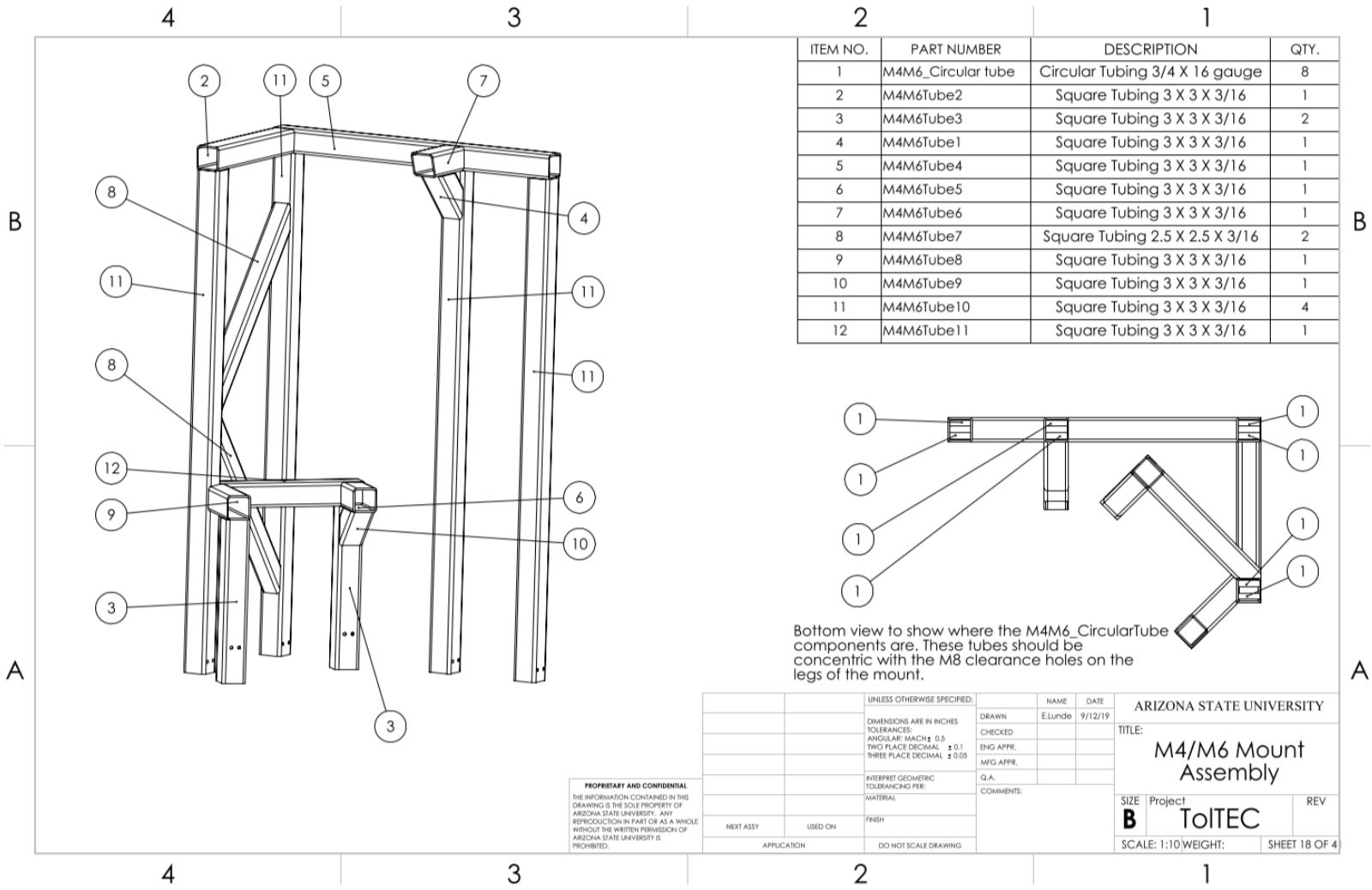

Figure 81. Mirror Mount Engineering Drawing

APPENDIX B

EXAMPLE OF LARGE MOUNT DESIGN USING SOLIDWORKS STATIC AND RESONANCE ANALYSIS: THE BABY BELUGA MOUNT

B.1 Setting Up Solidworks Static and Vibration Analyses

This appendix explores the Solidworks design process for the mount to hold the Baby Beluga cryostat. As discussed in Chapter 4, the mount must be able to support the 350 pound cryostat without deflections causing strain in the helium lines. The cryostat must be held in its operating orientation, high enough to remove the 300 K shell. Its resonance frequency must be higher than the 1-2 Hz frequency applied by the pulse tube cooler by a safety factor of 10. The safety factor accounts for errors in measuring the mass of the cryostat and makes the mount overall feel safer.

The first step to set up a FEA analysis in Solidworks is to set the material properties of the structure. The cryostat mount is constructed from square, aluminum beams, specifically the 6061-T6 alloy. Solidworks has an extensive materials library to select from. After selecting a material, the connections between the beams must be defined for the FEA solver to calculate how the loads apply to the whole structure. I used the Solidworks component interactions tool to automatically select the surfaces where beams interact and set these connections to be bonded since the mount is bolted together at these locations.

Next, I set the external loads applied to the structure. Figure 82 shows the loads for the static and vibration analyses. The mount shown here has all of the final cross beam locations, however, the loads were applied at the same locations for all the analyses. The first CAD image shows the external loads and reaction forces for the static analysis. The pink arrows on the top of the structure show where the weight of the cryostat was applied for the static analysis. The red arrow shows the direction of gravity. The green arrows show the fixed positions where the reaction forces are applied. The second CAD image shows the loads for the vibration analysis. I applied the cryostat weight as a remote mass by defining the cryostat's weight, center of mass, and moment of inertia. The pink dot represents the center of mass and the pink lines represent the rigid connection to the top of the mount. With the loads defined, I created a mesh for the structure and ran the static and vibration analyses for the cryostat mount.

B.2 Mount Design Changes from Static Analysis

Figure 83 shows the results for the static analyses done for the three different mount designs. These figures show the resultant displacement (URES) in millimeters. The first CAD image shows the first mount design. With only 0.65 mm deflection at its highest point, this mount meets the requirement for not adding strain to the helium lines. However, there is a small amount of buckling that occurs in the tall beams. To remove some of this buckling, I added support beams across the center of the tall

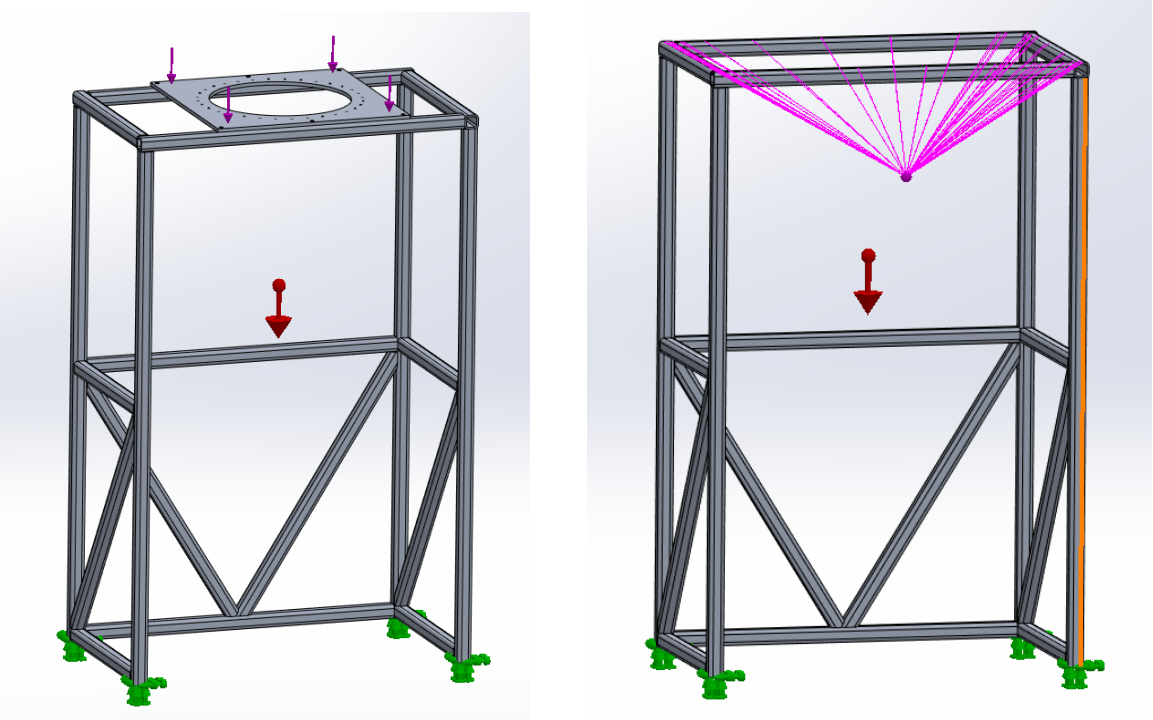

Figure 82. CAD Model That Shows the Locations of the Loads for Both the Static and Vibration Analyses.

beams. The resulting static analysis shown in the second CAD image. This model has a similar maximum deflection but the buckling in the tall beams was successfully reduced. The third CAD image in this figure shows the static analysis for the final support beam configuration. These beams were added during the vibration analysis steps. This design shows a small increase in the maximum deflection (0.79 mm), however, this still meets the design requirement.

B.3 Mount Design Changes from Vibration Analysis

No vibration analysis was done for the first beam configuration since the static analysis prompted me to add the support beams across the center of the vertical beams. Figure 84 shows the vibration analysis of the second mount design. Each of the sub-images shows the shape of the first five resonance modes. The units of the color bars are a normalized resonance amplitude (AMPRES). Normalized since the deflection of the resonance depends on the driving frequency's amplitude. After looking at the shapes of the resonances, I added the angled beams from the ground to the central cross beams to counter-act these shapes. Figure 85 shows the vibration

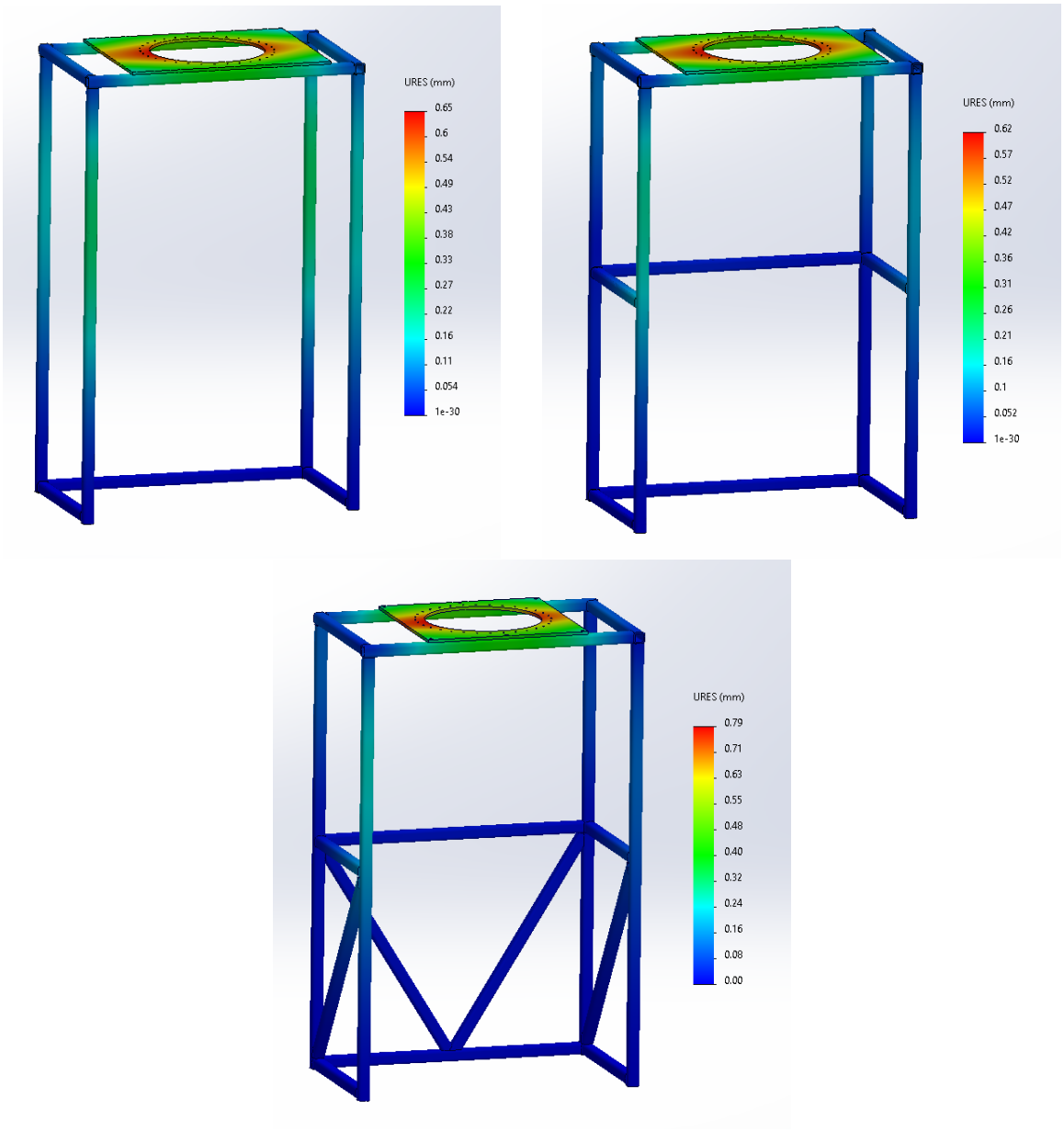

Figure 83. Static CAD Analysis Results for the First, Second, and Third Mount Iterations.

Table 14. Baby Beluga Mount Mechanical Resonance Modes

Design	Mode 1 (Hz)	Mode 2 (Hz)	Mode 3 (Hz)	Mode 4 (Hz)	Mode 5 (Hz)
Second	14.11	18.65	23.67	55.06	58.31
Third	21.91	29.95	38.47	60.28	64.60

analysis of the final mount design. Again, each of the sub-images shows the shape of the first five resonance modes. The shapes of the resonance modes have been altered. Table 14 compares the resonances of the second and final mount designs. By adding new cross beams, I increased the frequencies of the resonances.

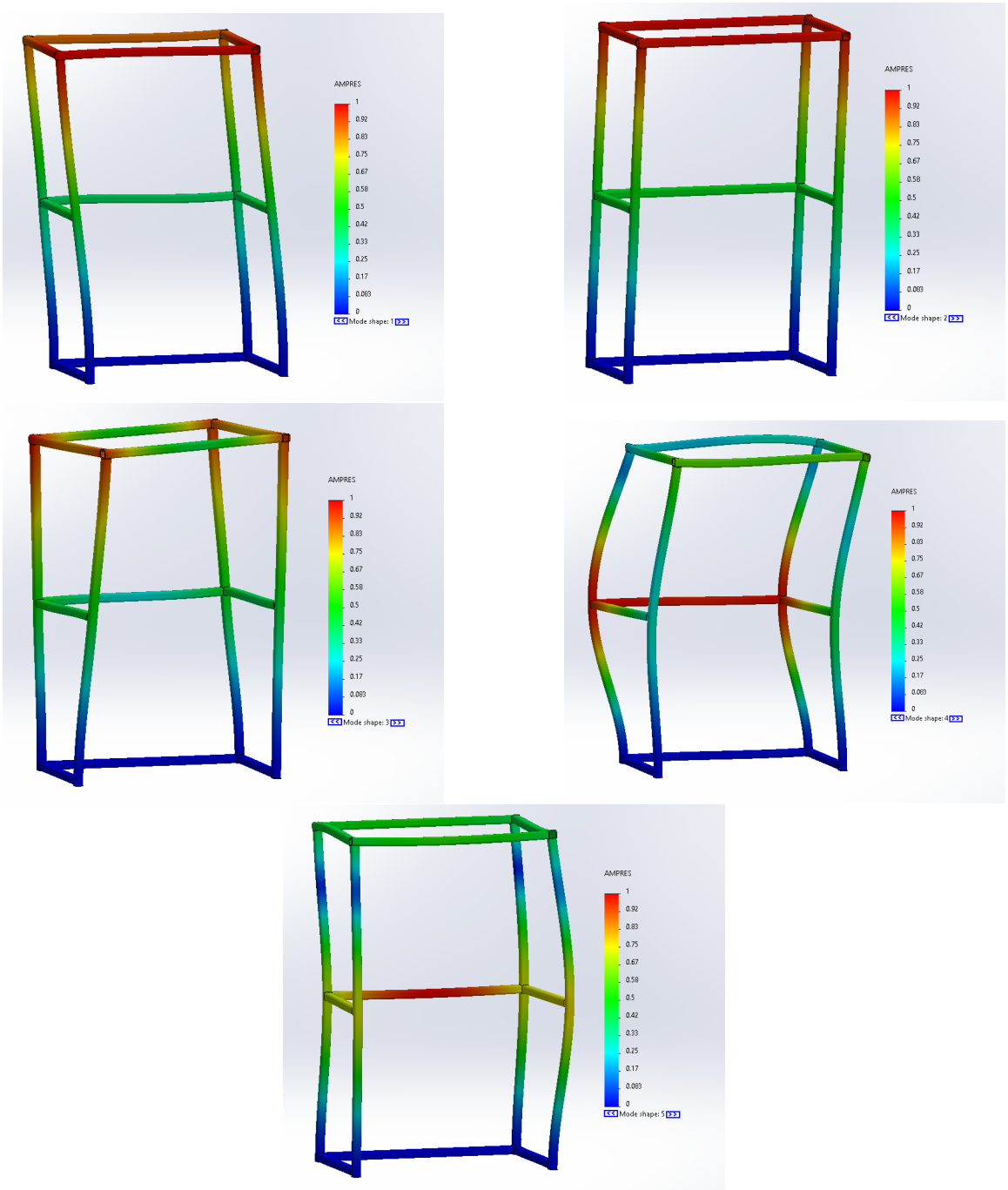

Figure 84. Resonance Analysis for the Second Baby Beluga Mount Design. Shows the Shape of the First 5 Resonance Modes.

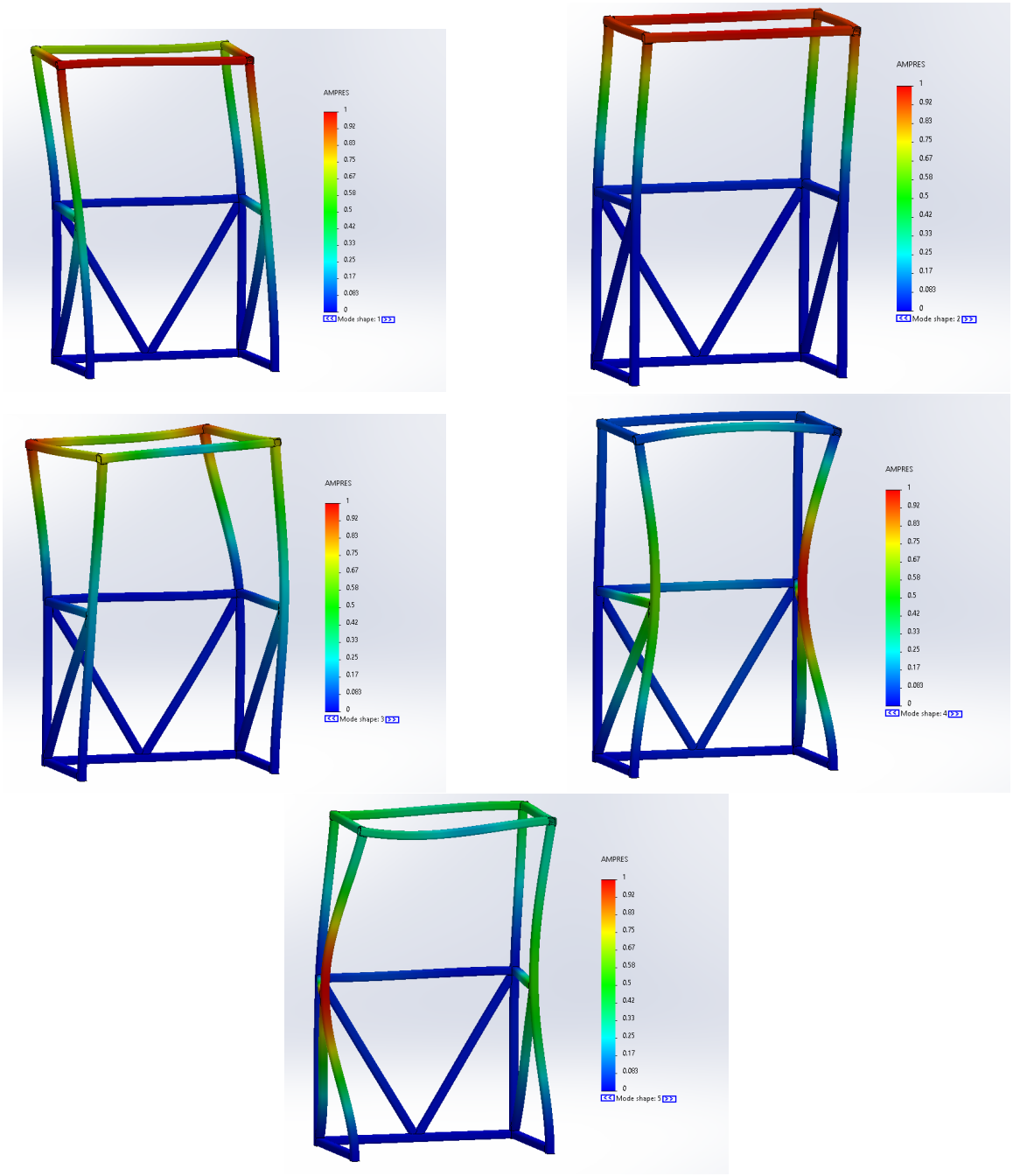

Figure 85. Resonance Analysis for the Final Baby Beluga Mount Design. Shows the Shape of the First 5 Resonance Modes.